ALMA MATER STUDIORUM
UNIVERSITÀ DI BOLOGNA

Department of Electrical, Electronic, and Information Engineering
“Guglielmo Marconi”

Ph.D. in Electrical Engineering
XXVI Cycle
Power Electronics, Electrical Machines and Drives (ING-IND/32)

Diagnosis and Fault Detection in Electrical Machines and Drives based on Advanced Signal Processing Techniques

Ph.D thesis of:
Yasser Gritli

Tutor :
Prof. Fiorenzo Filippetti

Ph.D. Coordinator:
Prof. Domenico Casadei

Final dissertation on March 2014

AKNOWLEDGEMENTS

This research project has been carried out at the Department of Electrical, Electronics and Information Engineering “Guglielmo Marconi” (DEI), at University of Bologna, Bologna, ITALY.

First of all, I would like to express my deep and sincere gratitude to my supervisor Prof. Fiorenzo Filippetti for his excellent supervision and helps during this work. I would like to thank all my Professors at the Department of Electrical Engineering for all their technical, professional and administrative support.

I want in special thanks to, Prof. Domenico Casadei, Prof. Giovanni Serra, Prof. Claudio Rossi, Prof. Luca Zarri, Prof. Gabriele Grandi, and Prof. Angelo Tani.

My greatest thanks go to Prof. Rosario Miceli from University of Palermo-Italy, Prof. Sang Bin Lee from University of Seoul-Korea, Prof. Gérard-André Capolino from University of Picardie “J. Verne”- France, and Prof. Mohamed Ben Rejeb from University of Tunis El Manar-Tunisia.

Many thanks go also to all my colleagues, who have assisted me during the work of this Ph.D. thesis especially Andrea Stefani, Michele Mengoni, Matteo Marano, and Alessio Pilati.

Finally, I owe my gratitude to my Mother, my Father, my Sisters, my Boutheina, my Sarra and my family members for all their love and support.

CONTENT

LISTE OF FIGURES

LIST OF TABLES

NOMENCLATURE

f	Stator frequency
s	Slip
ω_r	Rotor speed
θ_r	Rotor position angle
θ	Stator-flux phase angle
R_s	Stator resistance
R_r	Rotor resistance
R_{add}	Additional resistance used during the tests
v_{ds}, v_{qs}	d–q components of the stator voltage vector in the synchronous reference frame
i_{ds}, i_{qs}	d–q components of the stator current vector in the synchronous reference frame
f_{sam}	Sampling frequency
f_{low}, f_{up}	Lower and upper limits of the instantaneous fault frequency evolution
f_{kss}, f_{krs}	Frequencies of the *k*th stator and rotor harmonic components due to a stator fault
f_{ksr}, f_{krr}	Frequencies of the *k*th stator and rotor harmonic components due to a rotor fault
L_m	Mutual inductance between stator and rotor windings
L_s, L_r	Stator and rotor self-inductances
i_{dms}, i_{qms}	d–q components of the magnetizing current in the synchronous reference frame
i_{as}, i_{bs}, i_{cs}	Stator phase currents
i_{ar}, i_{br}, i_{cr}	Rotor phase currents
v_{as}, v_{bs}, v_{cs}	Stator phase voltage
v_{dr}, v_{qr}	d–q components of the rotor modulating signals in the synchronous reference frame
f_{sl}	Sliding frequency
m_{Paj}	Mean power value of approximation signal.

PREFACE

Condition monitoring leading to fault diagnosis and prediction of electrical machines and drives has attracted researchers in the past few years because of its considerable influence on the operational continuation of many industrial processes. Reducing maintenance costs and preventing unscheduled downtimes, which result in lost production and financial income, are the priorities of electrical drive manufacturers and operators. In fact, correct diagnosis and early detection of incipient faults result in fast unscheduled maintenance and short downtime for the process under consideration. They also avoid harmful, sometimes devastating, consequences and reduce financial loss. An ideal diagnostic procedure should take the minimum measurements necessary from a machine and by analysis extract a diagnosis, so that its condition can be inferred to give a clear indication of incipient failure modes in a minimum time. During the last years there has been a considerable amount of research into the creation of new condition monitoring techniques for induction motors and drives, overcoming the drawbacks of traditional methods. More specifically, there has been a transition from techniques suitable for machines in steady state conditions to machines operating in time-varying conditions.

In the current thesis, a new diagnosis technique for electrical machines operating in time-varying conditions is presented, where the validity under speed-varying condition or fault-varying condition is validated.

The presented work was elaborated in five chapters organized as follows:

In the first chapter, the considered faults (stator, rotor electrical/mechanical faults) are introduced, and a literature review of the corresponding diagnosis techniques are presented and discussed.

The problematic of signal processing techniques used for electrical machine diagnosis operating in time-varying conditions is firstly presented in the second chapter. Then, the proposed approch is completely described and systematized in order to overcome limits of existing techniques.

The proposed diagnosis technique is validated for the detection of electrical faults in three-phase wound-rotor induction machines in the third chapter, where stator and rotor electrical faults were investigated under time-varying conditions.

In the fourth chapter, the proposed diagnosis technique is validated for the detection of rotor broken bars in single and double squirrel cage induction motors under time-varying conditions.

Finally, the detection of rotor demagnetization, in five-phase surface-mounted permanent magnet synchronous generators under time-varying conditions is investigated in the fifth chapter, where stator fault detection and localization in seven-phase induction machine is also investigated in time and frequency domains.

CHAPTER 1 : STATE OF ART IN DIAGNOSTIC FOR ELECTRICAL MACHINES

1.1 Introduction

Condition monitoring of electrical machines has become a very important technology in the field of electrical systems maintenance, mainly for its potential functions of failure prediction, fault identification, and dynamic reliability estimation. In this thesis, we make reference to induction machine, even if the discussed and proposed diagnostic technique can be extended and applied also to other kind of machines. For example to the permanent magnet machine as we can see in the following chapters.

Electrical machines are subject to different sorts of faults. Stator winding faults including: turn to turn, coil to coil, open circuit, phase to phase, or coil to ground, generally initiated by high-resistance connections. Rotor electrical faults which include rotor open phase, rotor unbalance due to short circuits or high-resistance connections for wound rotor machines, or rotor magnet demagnetization that can be caused by an over current on the stator windings. Rotor mechanical faults such as broken bar(s) or cracked end-ring for squirrel-cage machines, cracked rotor magnet, bearing damage, static/dynamic eccentricity, and misalignment. The aforementioned failure modes can potentially affect the good operating condition of any industrial system [1]-[4]. A recent reliability study [4] has revealed the distribution of failures in induction motors as illustrated in Fig. 1.1.

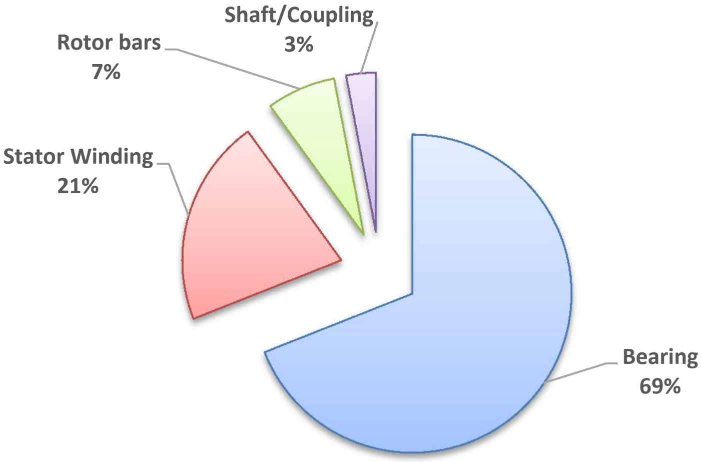

Fig. 1.1 Distribution of failures by motor component

During the last years there has been a considerable amount of research into the creation of new condition monitoring techniques for induction motors and drives, overcoming the drawbacks of traditional methods. In this context, different efficient and non-invasive diagnosis techniques have been developed which investigate easily measured electrical or mechanical quantities like for example current, external magnetic field, speed and vibrations, in order to detect the above listed failure modes at incipient stage of degradation. [5]-[8]. The topic is becoming far more attractive and critical as the population of electric machines has largely increased in recent years: the number of operating machines is about 16.1 billion in 2011, with a growth of about 50% in the last five years [9].

In this chapter, the considered faults (stator, rotor electrical/mechanical faults) are introduced, and a literature review of the corresponding diagnosis techniques are presented and discussed.

1.2 Stator related-faults

1.2.1 Stator faults physics

According to a recent reliability study, stator winding faults are of 21% ovrall distribution of failures by motor component [4]. This category of faults can be observed in different forms in electrical machines such as: turn to turn, coil to coil, open circuit, phase to phase, or coil to ground. Obviously consequences on the performances operating of the motor are different. In case of asymmetry in the stator windings such as an open-phase failure or high-resistance connection, the machine can operate, but with reduced torque. But in case of short-circuit of a few turns in a phase winding, the fault evolve rapidly in time, and leads to catastrophic damages.

It is universally known, that an electrical or magnetic non rotational asymmetry of induction machine or an asymmetry in the supply voltages can be detected through the stator current negative sequence. The machine behavior is not the ideal one but no drastic action must be taken in case of small asymmetries. A strong electric asymmetry, as an open phase, causes a negative sequence of similar magnitude compared with the positive one. This failure mode can be is therefore easily detected, and the protection system is triggered.

Winding short circuit is well known as one of the most difficult faults to detect at incipient stage. The standard protection might not work or the motor might keep on running while the heating in the shorted turns would soon cause critical insulation breakdown. If left undetected, turn faults will propagate, leading to phase to ground or phase to phase faults.

Then it is important to note that this failure mode is generally initiated by high-resistance connections caused by a combination of poor workmanship, thermal cycling and vibration, or damage of the contact surfaces due to pitting, corrosion or contamination.

The increase in the resistance due to poor contacts can cause overheating to reach an unacceptable level, which can eventually leads to open-circuit failures due to the melting of copper conductors. Eventually, excessive overheating in the contact points can also deteriorate insulation and expose the copper conductor to serious damages such as short-circuit failures between conductors or to the ground.

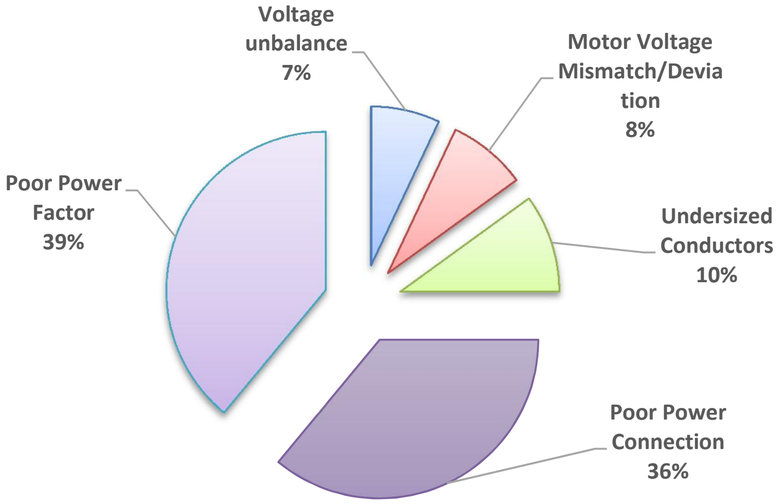

Fig. 1.2 Pareto of problems resulting in reduced motor efficiency (increased electrical losses) in electrical distribution systems

In a study performed by the Department of Energy at three industrial facilities [10], the losses in the electrical distribution system accounted for 2% of the annual plant energy usage. According to the Pareto (Fig. 1.2) of problems resulting in a decreased efficiency (or increased losses) in electrical distribution systems, 36% of the problems are due to the poor connections [11]. Recently, researchers focused their efforts in detecting the existence, the location and severity of high-resistance connections in circuits for electrical machines [12]-[14].

1.2.2 Stator fault components propagation

Electrical machines are subject to both electromagnetic and mechanical stresses, which are symmetrically distributed. In healthy conditions, the three stator and rotor impedances are identical and the currents are balanced. Under these normal conditions, only the normal frequency components at f and sf exist respectively on stator and rotor currents, where f is the power grid frequency and s the slip.

If the stator is damaged, the stator symmetry of the machine is lost and a reverse rotating magnetic field is produced. Let us assume that the stator and rotor voltages are not altered by the fault and that the machine speed is free to vary. Then, a frequency component appears in the stator current at frequency $-f$. This inverse sequence is reflected on the rotor side and produces the frequency component $(s-2)f$, which induces a pulsating torque and a speed oscillation at frequency $2f$. This frequency generates both a reaction current at frequency $(s-2)f$ and a new component at frequency $(s+2)f$. The latter produces new components in the stator currents at frequencies $\pm 3f$, and the process starts again. In conclusion, it leads to a set of new components at frequencies expressed by (1.1) and (1.2), in the stator and rotor currents respectively.

$$(f_{kss} = \pm\left(1-2k\right)f)_{k=0,1,2,...} \tag{1. 1}$$

$$(f_{krs} = \left(s \pm 2k\right)f)_{k=0,1,2,...} \tag{1. 2}$$

Fig. 1.3 gives a graphical interpretation of the aforementioned propagation mechanism of the fault harmonics. It is worth noting that this interpretation is just qualitative and may help the reader to understand the effect of a fault, but does not provide either a quantitative or an accurate description of all the phenomena involved [15].

Generally, the main focus are on the detection of fault dominant frequency components in stator signals at the frequency $-sf$ and at the frequency $(s-2)f$ in rotor signals. Fig. 1.3 shows the stator fault propagation in frequency domain. This fault can be monitored and detected in a variety of methods. In fact, the equivalent parameters of the machine are changed, the currents are not balanced, and all the quantities linked to the currents are affected by the faults. But in closed-loop operation the control system ensures a safe operation even under an unbalance in stator windings. Therefore, the typical rotor current fault frequency components is reduced by the compensating action of the control system. However, under these conditions the fault-related frequencies are reflected in the voltages that can be used for fault detection [15-16].

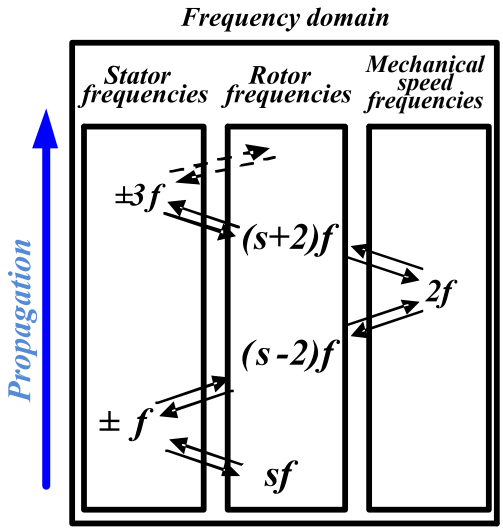

Fig. 1.3 Frequency domain propagation of a stator fault.
The minus sign (–) identifies current inverse sequence components

1.3 Rotor related-faults

1.3.1 Rotor faults physics

Different faults can affect the rotor part of induction motors, which were repartitioned in [17] and illustrated by Fig. 1.4. Squirrel cage machines can be classified in two different types of cage rotors for induction motors: cast (up to 3000-kW rating) and fabricated. Fabricated cages are used for higher ratings and special application machines, where possible failure events occur on bars and end-ring segment. Cast rotors are almost impossible to repair after bar breakage or cracks, although they are more durable and rugged than fabricated cages. Typically, they are used in laboratory tests to validate diagnostic procedures for practical reasons. Broken bar and cracked end ring faults share only 7 % of induction machine faults, but the detection of these events is a key item. In case of stator faults machine operation after the fault is limited to a short time, but in case of rotor faults the machine operation after the fault is not restricted apart from suitable caution during maintenance. On the other side the current in the rotor bar adjacent to the faulty one increases remarkably, up to 50 % of nominal current, while in the stator faulty winding the current variation is a few percent of the nominal current. Another special and interesting case is for double-cage induction motors. Doubly squirrel cage induction motors (DCIMs) are commonly used for applications in which high starting torque and efficient steady state operation are required, such as conveyors, pulverizers, or mills [18]. In these applications, DCIMs are subject to fatigue failure of the outer (“starting”) cage, due to the cyclic thermal/mechanical stress caused by frequent starts and long startup time [19]-[22].

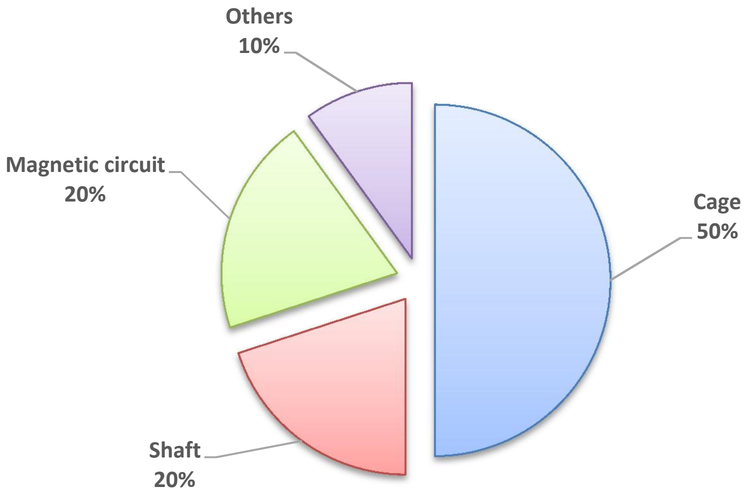

Fig. 1. 4 Rotor fault repartition in squirrel cage induction motors.

Failure of outer cage bars tends to spread to neighboring bars as the currents of the damaged bars are distributed into them. This could eventually result in startup failure due to insufficient startup torque [23]. An example of a DCIM failure with outer cage bar damage is shown in Fig. 1.5. This 800 kW, 3.3kV pulp stirrer motor recently failed in a paper mill in Korea. The inner cage was in good condition. On the contrary, the excessive thermal and thermo-mechanical stress due to outer cage damage resulted in “melting” and “fracture” of the outer bars (the temperature exceeded 200°C) [22]. This produced copper bar fragments that caused stator end winding insulation and core damage, and led to irreversible motor failure.

For wound-rotor machines, the physics of rotor fault is similar to stator fault and it results either in an increase of rotor resistance or in short and open circuits. In case of increased resistance, the machine can operate also after the fault occurrence, while in case of short and open circuits, after fault operation is limited to a short time. For wound rotor machines it is reasonable to assume that the percentage of stator windings and rotor windings faults can be divided in equal parts. In fact the rotor circuits of wound motors are usually poorly protected even in presence of adjunctive components (slip-ring connections, resistors connected to the slip rings).

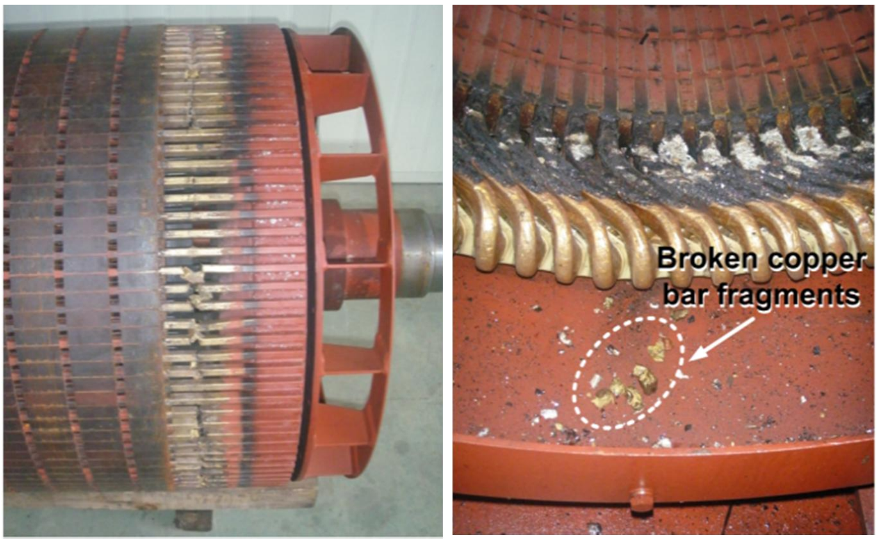

(a) **(b)**

Fig. 1. 5 Example of 3.3 kV, 800kW double cage induction motor failure due to outer cage damage: (a) outer bar damage, (b) stator end-winding insulation failure due to broken copper fragments from outer bar

1.3.2 Rotor fault components propagation

An electrical machine is subject to both electromagnetic and mechanical forces which are symmetrically distributed. In healthy conditions, the equivalent windings impedances are identical and consequently the stator and rotor currents are balanced. Under these normal conditions, only normal frequency components at f and sf exist respectively on stator and rotor currents, where f is the power grid frequency and s the slip.

If the rotor is damaged, the rotor symmetry of the machine is lost, the equivalent rotor windings impedances are no longer equal, and a reverse rotating magnetic field is produced. Consequently, an inverse frequency component appears in the rotor current at the frequency $-sf$. This component produces a fault frequency $(1-2s)f$ in the stator currents which causes a pulsating torque and a speed oscillation at the frequency $2sf$. This frequency induces both a reaction current at frequency $(1-2s)f$ and a new component at frequency $(1+2s)f$. The last frequency produces new components in the stator currents at frequencies $\pm 3sf$. As a consequence, a set of new frequency components defined as (1.3) appear in the spectrum of stator currents and a set of new frequency components expressed as (1.4) appear in spectra of rotor currents [15], [16].

$$\left(f_{ksr} = \left(1 \pm 2ks\right) f\right)_{k=\ 0,1,2,\ldots} \tag{1. 3}$$

$$\left(f_{krr} = \pm (1+2k) sf \right)_{k=0,1,2,\ldots} \tag{1. 4}$$

Usually, the diagnostic techniques are focused on the detection of fault dominant frequency components in stator signals at the frequency $(1\pm2s)f$ and at the frequency $-sf$ in rotor signals. Fig. 1.6 shows the rotor fault propagation in frequency and in time. This fault can be monitored and detected in a variety of methods. In fact, the equivalent parameters of the machine are changed, the currents are not balanced, and all the quantities linked to the currents are affected by the faults. The choice of the best method for a specific application can be made according to the following priorities: simplicity, sensitivity, ruggedness and reliability. Moreover, in closed-loop operation the control system ensures a safe operation even under an unbalance in both stator and rotor windings. Consequently, the typical rotor current fault frequency components is reduced by the compensating action of the control system. However, under these conditions the fault-related frequencies are reflected in the voltages that can be used for fault detection [24].

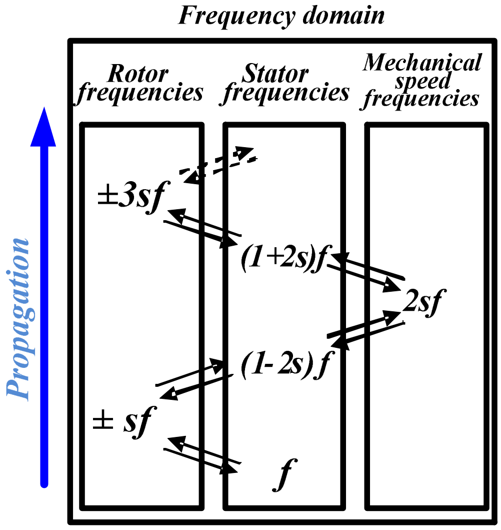

Fig. 1.6 Frequency domain propagation of a rotor fault.
The minus sign (–) identifies current inverse sequence components

1.4 Signal processing techniques for electrical machines diagnosis

Fault detection is efficient only when fault evolution is characterized by a time constant of the order of days or greater, so that suitable action can take place. In any case, a key item for the detection of any fault is proper signal conditioning and processing. With advances in digital technology over the last few years, adequate data processing capability is now available on cost-effective hardware platforms. They can be used to enhance the features of diagnostic systems on a real-time basis in addition to the normal machine protection functions.

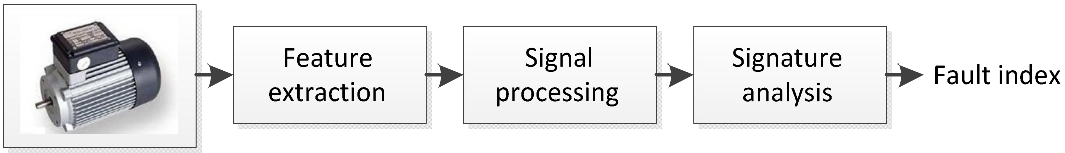

Fig. 1.7 Block topology of signal-based diagnostic procedure

Signal-based diagnosis looks for the known fault signatures in quantities sampled from the actual machine. Then, the signatures are monitored by suitable signal processing (Fig. 1.7). Typically, frequency analysis is used, although advanced methods and/or decision-making techniques can be of interest. Here, signal processing plays a crucial role as it can be used to enhance signal-to-noise ratio and to normalize data in order to isolate the fault from other phenomena and to decrease the sensitivity to operating conditions.

Different diagnosis techniques for electrical machines can be found in literature. In the category of time-domain analysis technique there are: the time-series averaging method, which consist in extracting a periodic component of interest from a noisy compound signal, the signal enveloping method, and the Kurtosis method, and the spike energy method [6], [25]-[28].

In [26], the oscillation of the electric power in the time domain becomes mapped in a discrete waveform in an angular domain. Data-clustering techniques are used to extract an averaged pattern that serves as the mechanical imbalance indicator. The maximum covariance method is another technique that is based on the computation of the covariance between the signal and the reference tones in the time domain [27].

Spectral frequency estimation techniques were widely adopted in machine diagnosis, as frequency domain tool analysis. These approaches are based on the Fourier analysis (FA) for investigating the signals being analyzed. Unluckily, electrical machines operate mostly in time-varying conditions. In this context, slip and speed vary unpredictably, and the classical application of FA for processing the voltage set points or the measured currents fails, as shown in [29]–[31]. In fact, the bandwidth of the fault frequency components is related to the speed variation. Among different solutions, the signal demodulation [29], the high-resolution frequency estimation [32], and the discrete polynomial-phase transform [33] have been developed to reduce the effect of the non-periodicity of the analyzed signals or to detect multiple faults [34]. These FA-based techniques give high-quality discrimination between healthy and faulty conditions, but they cannot provide any time-domain information.

This shortcoming in the FA-based techniques can be reduced by analyzing a small interval of the signal by means of the short-time Fourier transform. This method has been widely used to detect both stator and rotor failures in electrical motors. However, the fixed width of the window and the high computational cost required to obtain a good resolution still remain major drawbacks of this technique [35]–[37]. Based on the instantaneous frequencies issued from the intrinsic mode functions, the Hilbert–Huang transform was proposed for motor diagnosis and has shown quite interesting performances in terms of fault severity evaluation [38]–[41]. Other quadratic transforms, such as the Wigner–Ville distribution (WVD), suffer from the same constraint [42]. This limitation can be overcome by new advanced time–frequency distributions such as smoothed pseudo-WVDs [42], Choi–Williams distribution [42], [43], and Zhao–Atlas–Marks distribution [44]. However, the removal of cross-terms leads generally to reducing the joint time–frequency resolution and the signal energy.

Being a linear decomposition, wavelet transform (WT) provides a good resolution in time for high-frequency components of a signal and a good resolution in frequency for low-frequency components. In this sense, wavelets have a window that is automatically adjusted to give the appropriate resolution developed by its approximation and detail signals. Motivated by the aforementioned proprieties, in recent years, some authors have pointed out the effectiveness of WT for tracking fault frequency components under non-stationary conditions. WT was used with different approaches for monitoring motors. The related techniques are the undecimated discrete WT [45], the wavelet ridge method [46], the wavelet coefficients analysis [47], [48], or the direct use of wavelet signals [48]–[50] for stator- and rotor-fault detection. Recently, fractional Fourier transform has been proposed in [51], providing an innovative graphical representation of rotor-fault components issued from discrete WT in the time–frequency domain. More intensive research efforts have been focused on the usage of both approximation and detail signals for tracking different failure modes in motors, such as broken bars [35], [49]- [50], [52]-[53] interturn short circuits [35], [51], [54], mixed eccentricity, [49], [52], [55], and increasing resistance in a stator phase [15], [45], [56] or in a rotor phase [15], [37], [57].

Most of the reported contributions are based on wavelet analysis of currents during the start-up phase or during any load variation. In this context, the frequency components are spread in a wide bandwidth as the slip and the speed change considerably. The situation is more complex under rotor-fault conditions due to the proximity of the fault components to the fundamental frequency. These facts justify the usage of multidetail or/and approximation signals resulting from the wavelet decomposition [35], [48]–[50], [52]. Moreover, the different decomposition levels are imposed by the sampling frequency. However, the dependence on the choice of the sampling frequency and on the capability of tracking multiplefault frequency components makes difficult to interpret the fault pattern coming from wavelet signals and increases the diagnosis complexity. Moreover, the usage of large frequency bandwidths exposes the detection procedure to erroneous interpretations due to a possible confusion with other frequencies related to gearbox or bearing damages [58].

In order to quantify the fault severity, the energy of approximation and/or detail signals resulting from wavelet decomposition has been already used [35], [49]. However, this attempt reduces each time–frequency band to a single value. In this way, the time-domain information could be lost.

1.5 Conclusion

Potential failure modes in electrical machines, as stator and rotor electrical/mechanical faults, which are investigated in this thesis, were exhaustively analyzed. A literature review of the corresponding diagnosis techniques were also presented.

Finally, an important issue deduced particularly from section (1.4), which is the need to develop new diagnostic approaches for electrical machines operating in time-varying conditions, with possible improvements that can be formulated as follows:

1) Capability of monitoring the fault evolution continuously over time under any transient operating condition;
2) No requirement for speed/slip measurement or estimation;
3) Higher accuracy in filtering frequency components around the fundamental;
4) Reduction in the likelihood of false indications by avoiding confusion with other fault harmonics (the contribution of the most relevant fault frequency components under speed-varying conditions are clamped in a single frequency band);
5) Low memory requirement due to low sampling frequency;
6) Reduction in the latency of time processing (no requirement of repeated sampling operation).

Effectively, in the present thesis, an effective method to solve the aforementioned open points in time-varying conditions is presented. A complete description which systematizes the use of the developed approach is presented in Chapter 2, and experimental results showing the validity of the presented technique are presented and exhaustively commented in the next chapters.

REFERENCES

[1] A.H. Bonnet, and G.C. Soukup, ‘‘Cause and analysis of stator and rotor failures in three-phase squirrel cage induction motors,” *IEEE Transactions on Industry Applications*, Vol. 28, N°4, pp. 921–937, 1992.

[2] Nandi, S., Toliyat, H.A.; Xiaodong Li, "Condition monitoring and fault diagnosis of electrical motors-a review," *Energy Conversion, IEEE Transactions on*, vol.20, no.4, pp.719,729, Dec. 2005

[3] R. M. Tallam, S. B. Lee, G. C. Stone, G. B. Kliman, J. Yoo, T. G. Habetler, and R. G. Harley, “A survey of methods for detection of stator-related faults in induction machines,” *IEEE Transactions on Industry Applications*, vol. 43, no. 4, pp. 920–933, Jul./Aug. 2007.

[4] A.H. Bonnett, C. Yung, ‘‘Increased Efficiency Versus Increased Reliability,” *IEEE Industry Application Magazine*, Vol. 14, N°1, pp. 29–36, 2008.

[5] G.K. Singh, S.A.S. Al Kazzaz, ‘‘Induction machine drive condition monitoring and diagnostic research-a survey,” *Journal of Electric Power Systems Research*, Vol. 64, N°2, pp. 145–158, 2003.

[6] A. Bellini, F. Filippetti, C. Tassoni and G.-A. Capolino, ‘‘Advances in Diagnostic Techniques for Induction Machines,” *IEEE Transactions on Industrial Electronics*, Vol. 55, N°12, pp. 4109–4126, 2008.

[7] F. Filippetti, A. Bellini, G-A. Capolino, “Condition monitoring and diagnosis of rotor faults in induction machines: State of art and future perspectives”, *IEEE Workshop on Electrical Machines Design Control and Diagnosis (WEMDCD’2013)*, pp. 196-209, Paris, 2013.

[8] S.H. Kia, H. Henao, G. Capolino, “Efficient digital signal processing techniques for induction machines fault diagnosis”, *IEEE Workshop on Electrical Machines Design Control and Diagnosis (WEMDCD’2013)*, pp. 232-246, Paris, 2013.

[9] H. A. Toliyat, S. Nandi, S. Choi, and H. Meshgin-Kelk, Electric Machines, Modeling, condition monitoring and Fault diagnosis. *CRC Press*, 2012.

[10] “Energy tips—Motor systems,”Motor Systems Tip Sheet #8, Sep. 2005, Washington, DC: U.S. Dept. Energy. [Online]. Available: http://www1 eere.energy.gov/industry/saveenergynow/database/index.asp?filter=4

[11] Electrical Distribution System Tune-Up, Bonneville Power Administration, Portland, OR, Jan. 1995.

[12] J. Bockstette, E. Stolz, and E.J.Wiedenbrug, “Upstream impedance diagnostics for three phase induction machines,” *Proc. of IEEE SDEMPED*, Cracow, Poland, 2007, pp. 411-414.

[13] Y. Jangho, C. Jintae, B.L. Sang and Y. Jiyoon, ‘‘On-line Detection of High-Resistance Connections in the Incoming Electrical Circuit for Induction Motors,” *IEEE Transactions on Industry Applications*, Vol. 45, N°2, pp. 694–702, 2009.

[14] J. Yun, J. Cho, S.B. Lee, J. Yoo,“On-line detection of high-resistance connections in the incoming electrical circuit for induction motors,” *IEEE Transactions on Industry Applications*, Vol. 45, Issue 2, pp. 694-702, 2009.

[15] A. Stefani, A. Yazidi, C. Rossi, F. Filippetti, D. Casadei and G.A. Capolino, ‘‘Doubly Fed Induction Machines Diagnosis Based on Signature Analysis of Rotor Modulating Signals,” *IEEE Transactions on Industry Applications*, Vol. 44, N°6, pp.1711–1721, Nov./Dec. 2008.

[16] D. Casadei, F. Filippetti, C. Rossi, A. Stefani, A. Yazidi et G. A.Capolino, ‘‘Diagnostic technique based on rotor modulating signals signature analysis for doubly fed induction machines in wind generator systems,” *Conference Record of the 41st IAS-IEEE Annual Meeting in Industry Applications Conference*, Tampa, Oct.2006.

[17] Vaag Thorsen, M. Dalva, “Failure ldentificatinn and Analysis for High-Voltage Induction Motors in the Petrochemical Industry”, *IEEE Transactions on Indusbry Applications*, Vol. 35, No.4, July/August 1999, pp. 810- 819.

[18] Motors and generators, NEMA standards pub. MG 1-2006, 2006.

[19] P.L. Alger, and J.H. Wray, “Double and triple squirrel cages for polyphase induction motors,” *AIEE Transactions Part III – Power Apparatus and Systems*, vol. 78, no.2, pp. 637-645, Jan. 1953.

[20] G. Kovacs, “Starting disc rotor for high-output two-pole induction motors”, in *Proc. IEEE IAS*, pp. 8-12, vol. 1, 1990.

[21] H.A. Toliyat, G.B. Kliman, Handbook of electric motors, 2nd edition, Marcel Dekker, 2004.

[22] J. Mroz, “Temperature field distribution of a double squirrel-cage rotor during startup,” *IEE Proceedings – Electric Power Applications*, vol. 152, no. 6, pp. 1531-1538, Nov. 2005.

[23] W.Schuisky, “Starting losses in windings of double squirrel-cage motors,” *Electrical Engineers - Part II: Journal of Power Engineering*, vol. 95, N° 45, pp. 325 – 327, 1948.

[24] D. Casadei, F. Filippetti, C. Rossi and A. Stefani, "Closed Loop Bandwidth Impact on Doubly Fed Induction Machine Asymmetries Detection Based on Rotor Voltage Signature Analysis", *43rd UPEC’08*, Padova-Italy, Sept. 2008.

[25] A. Dimarogonas, Vibration for Engineers. Englewood Cliffs, NJ: Prentice-Hall, 1996.

[26] C. Kral, T. G. Habetler, and R. G. Harley, “Detection of mechanical imbalances of induction machines without spectral analysis of time-domain signals. *IEEE Transactions on Industrial Application*, Vol. 40, No. 4, pp. 1101-1106, 2004.

[27] A. Bellini, G. Franceschini, and C. Tassoni, “Monitoring of induction machines by maximum covariance method for frequency tracking,” *IEEE Trans. Ind. Appl.*, vol. 42, no. 1, pp. 69–78, Jan./Feb. 2006.

[28] J. Lin., “An integrated time domain averaging scheme for gearbox diagnosis. IEEE Proceeding: *8th International Conference on Reliability, Maintainability and Safety*, Pages: 808-812, 2009.

[29] A. Stefani, F. Filippetti, and A. Bellini, “Diagnosis of induction machines in time-varying conditions,” *IEEE Trans. Ind. Electron.*, vol. 56, no. 11 , pp. 4548–4556, Nov. 2009.

[30] Y. Gritli, C. Rossi, L. Zarri, F. Filippetti, A. Chatti, D. Casadei, and A. Stefani, “Double frequency sliding and wavelet analysis for rotor fault diagnosis in induction motors under time-varying operating condition,” *in Proc. IEEE Int. Symp. Diagn. Elect. Mach., Power Electron. Drives*, Bologna, Italy, Sep. 5–8, 2011, pp. 676–683.

[31] B. Akin, S. Choi, U. Orguner, and H. A. Toliyat, “A simple real-time fault signature monitoring tool for motor-drive-embedded fault diagnosis system,” *IEEE Trans. Ind. Electron.*, vol. 58, no. 5, pp. 1990–2001 , May 2011.

[32] S. H. Kia, H. Henao, and G. A. Capolino, “A high-resolution frequency estimation method for three-phase induction machine fault detection,” *IEEE Trans. Ind. Electron.*, vol. 54, no. 4, pp. 2305–2314, Aug. 2007.

[33] M. Pineda-Sanchez, M. Riera-Guasp, J. Roger-Folch, J. A. AntoninoDaviu, J. Perez-Cruz, and R. Puche-Panadero, “Diagnosis of induction motor faults in

time-varying conditions using the polynomial-phase transform of the current," *IEEE Trans. Ind. Electron.*, vol. 58, no. 4, pp. 1428 – 1439, Apr. 2011.

[34] A. Garcia-Perez, R. de Jesus Romero-Troncoso, E. Cabal-Yepez, and R. A. Osornio-Rios, "The application of high-resolution spectral analysis for identifying multiple combined faults in induction motors," *IEEE Trans. Ind. Electron.*, vol. 58, no. 5, pp. 2002–2010, May 2011.

[35] J. Cusido, L. Romeral, J.A. Ortega, J.A. Rosero et A. G. Espinosa, ''Fault Detection in Induction Machines Using Power Spectral Density in Wavelet Decomposition," *IEEE Transactions on Industrial Electronics*, Vol. 55, N°2, pp. 633–643, 2008.

[36] S. H. Kia, H. Henao, and G.-A. Capolino, "Torsional vibration assessment using induction machine electromagnetic torque estimation," *IEEE Trans. Ind. Electron.*, vol. 57, no. 1, pp. 209–219, Jan. 2010.

[37] I. P. Tsoumas, G. Georgoulas, E. D. Mitronikas, and A. N. Safacas, "Asynchronous machine rotor fault diagnosis technique using complex wavelets," *IEEE Trans. Energy Convers.*, vol. 23, no. 2, pp. 444–459 , Jun. 2008.

[38] R. Yan and R. X. Gao, "Hilbert–Huang transform-based vibration signal analysis for machine health monitoring," *IEEE Trans. Instrum. Meas.*, vol. 55, no. 6, pp. 2320–2329, Dec. 2006.

[39] J. Antonino-Daviu, P. J. Rodriguez, M. Riera-Guasp, A. Arkkio, J. Roger-Folch, and R. B. Perez, "Transient detection of eccentricity related components in induction motors through the Hilbert–Huang transform," *Energy Convers. Manage.*, vol. 50, no. 7, pp. 1810–1820 , Jul. 2009.

[40] A. Espinosa, J. Rosero, J. Cusido, L. Romeral, and J. Ortega, "Fault detection by means of Hilbert–Huang transform of the stator current in a PMSM with demagnetization," *IEEE Trans. Energy Convers.*, vol. 25 , no. 2, pp. 312–318, Jun. 2010.

[41] R. Puche-Panadero, M. Pineda-Sanchez, M. Riera-Guasp, J. Roger-Folch, E. Hurtado-Perez, and J. Peres-Cruz, "Improved resolution of the MCSA method via Hilbert transform, enabling the diagnosis of rotor asymmetries at very low slip," *IEEE Trans. Energy Convers.*, vol. 24, no. 1, pp. 52 –59, Mar. 2009.

[42] S. Rajagopalan, J. M. Aller, J. A. Restrepo, T. G. Habetler, and R. G. Harley, "Detection of rotor faults in brushless DC motors operating under non-stationary conditions," *IEEE Trans. Ind. Appl.*, vol. 42, no. 6 , pp. 1464–1477, Nov./Dec. 2006.

[43] S. Rajagopalan, J. A. Restrepo, J. M. Aller, T. G. Habetler, and R. G. Harley, “Non-stationary motor fault detection using recent quadratic time–frequency representations,” *IEEE Trans. Ind. Appl.*, vol. 44, no. 3 , pp. 735–744, May/Jun. 2008.

[44] Y. Zhao, L. E. Atlas, and R. J. Marks II, “The use of cone-shaped kernels for generalized time–frequency representations of nonstationary signals,” *IEEE Trans. Acoust., Speech, Signal Process.*, vol. 38, no. 7, pp. 1084 – 1091, Jul. 1990.

[45] W. G. Zanardelli, E. G. Strangas, and S. Aviyente, “Identification of intermittent electrical and mechanical faults in permanent-magnet AC drives based on time–frequency analysis,” *IEEE Trans. Ind. Appl.*, vol. 43, no. 4 , pp. 971–980, Jul./Aug. 2007.

[46] S. Rajagopalan, J. M. Aller, J. A. Restrepo, T. G. Habetler, and R. G. Harley, “Analytic wavelet ridge-based detection of dynamic eccentricity in brushless direct current (BLDC) motors functioning under dynamic operating conditions,” *IEEE Trans. Ind. Electron.*, vol. 54, no. 3 , pp. 1410–1419, Jun. 2007.

[47] O. A. Mohammed, N. Y. Abed, and S. Ganu, “Modeling and characterization of induction motor internal faults using finite-element and discrete wavelet transforms,” *IEEE Trans. Magn.*, vol. 42, no. 10, pp. 3434–3436, Oct. 2006.

[48] A. Ordaz-Moreno, R. J. Romero-Troncoso, J. A. Vite-Frias, J. R. Rivera-Gillen, and A. Garcia-Perez, “Automatic online diagnosis algorithm for broken-bar detection on induction motors based on discrete wavelet transform for FPGA implementation,” *IEEE Trans. Ind. Electron.*, vol. 55, no. 5, pp. 2193–2202, May 2008.

[49] M. Riera-Guasp, J. A. Antonino-Daviu, M. Pineda-Sanchez, R. Puche-Panadero, and J. Perez-Cruz, “A general approach for the transient detection of slip-dependent fault components based on the discrete wavelet transform,” *IEEE Trans. Ind. Electron.*, vol. 55, no. 12, pp. 4167–4180, Dec. 2008.

[50] A. Bouzida, O. Touhami, R. Ibtiouen, A. Belouchrani, M. Fadel, and A. Rezzoug, “Fault diagnosis in industrial induction machines through discrete wavelet transform,” *IEEE Trans. Ind. Electron.*, vol. 58, no. 9, pp. 4385–4395, Sep. 2011.

[51] M. Pineda-Sanchez, M. Riera-Guasp, J. A. Antonino-Daviu, J. Roger-Folch, J. Perez-Cruz, and R. Puche-Panadero, “Diagnosis of induction motor faults in the fractional Fourier domain,” *IEEE Trans. Instrum. Meas.*, vol. 59, no. 8, pp. 2065–2075, Aug. 2010.

[52] J. Antonino-Daviu, P. Jover Rodriguez, M. Riera-Guasp, M. Pineda Sanchez, and A. Arkkio, “Detection of combined faults in induction machines with stator parallel branches through the DWT of the startup current,” *Mech. Syst. Signal Process.*, vol. 23, no. 7, pp. 2336–2351, Oct. 2009.

[53] J. Pons-Llinares, J. A. Antonino-Daviu, M. Riera-Guasp, M. Pineda-Sanchez, and V. Climente-Alarcon, “Induction motor diagnosis based on a transient current analytic wavelet transform via frequency B-splines,” *IEEE Trans. Ind. Electron.*, vol. 58, no. 5, pp. 1530–1544, May 2011.

[54] A. Gandhi, T. Corrigan, and L. Parsa, “Recent advances in modeling and online detection of stator interturn faults in electrical motors,” *IEEE Trans. Ind. Electron.*, vol. 58, no. 5, pp. 1564–1575, May 2011.

[55] W. Yang, P. J. Tavner, C. J. Crabtree, and M. Wlikinson, “Cost-effective condition monitoring for wind turbines,” *IEEE Trans. Ind. Electron.*, vol. 57, no. 1, pp. 263–271, Jan. 2010.

[56] Y. Gritli, A. Stefani, C. Rossi, F. Filippetti, and A. Chatti, “Experimental validation of doubly fed induction machine electrical faults diagnosis under time-varying conditions,” *Elect. Power Syst. Res.*, vol. 81, no. 3, pp. 751–766, Mar. 2011.

[57] Y. Gritli, A. Stefani, C. Rossi, F. Filippetti, and A. Chatti, “Advanced rotor fault diagnosis for DFIM based on frequency sliding and wavelet analysis under time-varying condition,” *in Proc. IEEE ISIE*, Bari, Italy, Jul. 2010, pp. 2607–2614.

[58] W. T. Thomson and M. Fenger, “Current signature analysis to detect induction motor faults,” *IEEE Ind. Appl. Mag.*, vol. 7, no. 4, pp. 26–34, Jul./Aug. 2001.

CHAPTER 2 : DEVELOPED APPROACH FOR DIAGNOSING ELECTRICAL MACHINES

2.1 Introduction

In the present chapter, the problematic of signal processing techniques used for electrical machine diagnosis operating in time-varying conditions is firstly analyzed: limits of Fourier analysis, the use of multi-frequency bands for tracking single fault component, and latency of calculation with direct use of Discrete Wavelet Transform (DWT). Then, a new effective method is completely described and systematized in order to achieve the different open points established in the previous chapter.

2.2 Signals and processing tools for faults characterization

2.2.1 Signals selection for processing

Under normal operating conditions, electrical machines are subject to electromagnetic and mechanical stresses symmetrically distributed. Once the motor is affected by stator/rotor faults, the symmetry is lost, and the impact of this dissymmetry is reflected on the electrical and mechanical quantities: currents, voltages, torque, magnetic fluxes, or vibrations.

In fact, many contributions can be found in literature dealing with stator or rotor faults diagnosis of electrical machines, based on monitoring of available electrical or mechanical signals. Fault harmonics classification in term of adopted input signals for processing is illustrated by Table. 2.1. Since most bearing vibrations are periodical movements, vibration signature analysis was widely investigated for these purposes [1]-[3].

Table. 2. 1 Fault harmonics Classification in term of Adopted input signals for processing

Fault	Signal	Characteristic Frequency
Stator asymmetry	Stator current	$(f_{kss}=\pm(1-k)f)_{k=0,1,2,\dots}$
	Rotor current/voltages	$(f_{krs}=(s\pm 2k)f)_{k=0,1,2,\dots}$
Rotor asymmetry	Stator current	$(f_{ksr}=(1\pm 2ks)f)_{k=0,1,2,\dots}$
	Rotor currents/voltages	$(f_{krr}=\pm(1+2k)sf)_{k=0,1,2,\dots}$
	Vibration	$f_{kvr}=(6-2ks)f)_{k=1,2,3,\dots}$
Mixed eccentricity	Stator current	$f_{ks}=\lvert f\pm kfr\rvert_{k=1,2,3,\dots}$
Bearing outer race	Stator current	$f_{mob}=\lvert f\pm mfv\rvert_{m=1,2,3,\dots}$
	Vibration	$f_{vob}=(N/2).fr.(1-b_b cos(\beta)/dp)$
Bearing cage	Vibration	$f_{vcb}=(1/2).fr.(1-d_b cos(\beta)/dc$
Bearing inner raceway	Vibration	$f_{vib}=(Nb/2).fr.(1+d_b cos(\beta)/dc$
Bearing ball	Vibration	$f_{vbb}=(dc/db).fr.(1-(d_b cos(\beta)/dc)^2)$
Magnet demagnetization	Back-emf	$(f_{kdem}=f(1\pm k/p))_{k=0,1,2,\dots}$
…	…	…

Leakage flux was successfully applied to monitor machine conditions [4]-[5] provided that a suitable shield was available to prevent the influence of external sources. Measured or observed electromagnetic torque was widely investigated for diagnosing mechanical faults [6]-[7].

For conventional machines, the available quantities are three line currents (i_a, i_b, i_c) and three line-to-line voltages (v_{ab}, v_{bc}, v_{ca}). Actual quantities are usually transformed in order to obtain equations with time-invariant coefficients. Moreover, the transformation reduces the number of dimensions of the state variables, and a suitable reference frame may be retrieved in order to simplify the machine model according to the desired operations. For example, in field-oriented control, the right choice of the reference frame results in decoupling of flux and torque.

Another issue in closed-loop operation, is that the control itself affects the behavior of electrical variables, and so new diagnostic procedures are necessary for machine monitoring. In [8], the impact of currents regulators was evidenced and a new approach based on the analysis of rotor modulating signals was proposed for stator and rotor fault diagnosis in steady state conditions [9]. One of the main objectives of this thesis is to extend this approach to time varying operating conditions, using new signal processing technique for investigating the control variables in this context. Also vibration signals will be considered for diagnosing rotor mechanical faults, in order to evaluate the performances of the proposed approach.

2.2.2 Signal Processing tools

Different signal processing techniques for diagnosing electrical machines can be found in literature which can be classified in three categories: time-domain analysis, frequency domain analysis, and time-frequency domain analysis. As already introduced in chapter. 1, the main focus in this thesis is the extension of frequency-domain signature faults to optimal time-frequency domain analysis. In the following, a detailed discussion showing the necessity and advantages of migration from frequency domain analysis (represented by Fourier transform), to time-frequency domain analysis (represented by Wavelet Transform), [10]-[13].

2.2.2.1 Fourier Transform

Fourier analysis breaks down a signal in its constituting sinusoids of different frequencies. In other words, the view of the signal changes from time-base to frequency-base. This technique decomposes a signal into orthogonal trigonometric basis functions. The Fourier transform of a continuous signal x(t) is defined as:

$$X^{FT}(f)=\int_{-\infty}^{+\infty} x(t).e^{-j2\pi ft}dt \qquad (2.1)$$

This transformation gives the global frequency distribution of the original time-domain signal x(t) . Most experimentally obtained signals are not continuous in time, but sampled as discrete time intervals ΔT. Furthermore they are of finite length with a total measurement time T, divided into N = T/ΔT intervals. These kind of signals can be analyzed in the frequency domain using the discrete Fourier transform (DFT), defined in (2.2). Due to the sampling of the signal, the frequency spectrum becomes periodic, so the frequencies that can be analyzed are finite. The DFT is evaluated at discrete frequencies f_n = n/T, n = 0, 1, 2, . . . , N − 1.

$$X^{DFT}\left(f_n\right)=\frac{1}{N}\sum_{k=0}^{N-1}x\left(k\right).e^{-j2\pi k\Delta T} \tag{2.2}$$

The calculation of the DFT can become very time-consuming for large signals (large N). The fast Fourier transform (FFT) algorithm does not take an arbitrary number of intervals N , but only the intervals N = 2^m, m ∊ N. The reduction in the number of intervals makes the FFT very fast. A drawback compared to the ordinary DFT is that the signal must have 2m samples, this is however in general no problem.

FFT was widely used for electrical machines diagnosis, and has shown efficient ability to discriminate healthy from faulty operating conditions. Intersting results in diagnosisng electrical and mechanical faults, based on FFT can be found in [4]-[5], [8]-[9].

However, the calculation of the FFT suffer from two limits and has a big drawback for any fault detection procedure. First since only a small part of the signal x(t) on the interval 0 ≤ t ≤ T is used, leakage can occur. Leakage is caused by the discontinuities introduced by periodically extending the signal. Leakage causes energy of fundamental frequencies to leak out to neighboring frequencies. A solution to prevent signal leakage is by applying a window to the signal which makes the signal more periodic in the time interval. A disadvantage is that the window itself has a contribution in the frequency spectrum. The second problem is the limited number of discrete signal values, this can lead to aliasing. Aliasing causes fundamental frequencies to appear as different frequencies in the frequency spectrum and is closely related to the sampling rate of the original signal. Aliasing can be prevented if the sampling theorem of Shannon is fulfilled. The theorem of Shannon states that no information is lost by the discretization if the sample time ΔT equals or is smaller than ΔT = $2/f_{max}$. Finally, the major drawback of this technique is the lost of the time information, as it is not possible to determine when a particular event, such a discontinuity or a transient, takes place.

2.2.2.2 Short Time Fourier Transform

In order to analyze small sections of a signal, Denis Gabor developed a technique, the STFT that consists in the calculation of the Fourier transform of the original signal multiplied by a window function that is nonzero for only a short period of time as in

(2.3). More specifically, a signal x(t) is windowed by a window g(t) of limited extend, centered at time τ . The * denotes the complex conjugated. From the windowed signal a FT is taken, giving the frequency content of the signal in the windowed time interval.

$$X^{TFCT}\left(\tau,f\right)=\int_{-\infty}^{+\infty}x\left(t\right).g^{*}(t-\tau).e^{-j2\pi ft}dt \qquad (2.3)$$

As illustrated by Fig. 2.1, the STFT maps a signal into a two-dimensional function of time (i.e., the position of the window) and frequency. Since the size of the time window is the same for all frequencies, the STFT has a fixed resolution. A short window gives a good time resolution, but different frequencies are not identified very well.

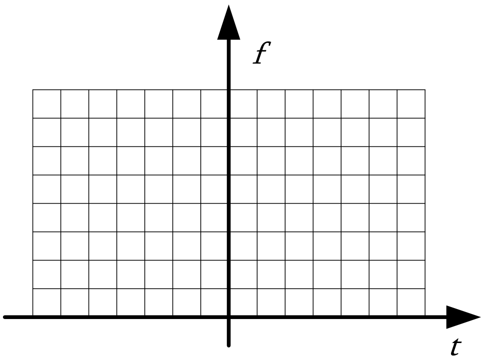

Fig. 2. 1 Constant resolution in time-frequency plane using Short-time Fourier Transform

This method was widely used to detect stator and rotor failures in induction motors. However the fixed size of the chosen window, the difficulties in quantifying the faults extent and the high computational cost required to obtain a good resolution still remain the major drawbacks of this technique[14]-[15].

However, practically all electrical or mechanical signals candidates to analysis for faults diagnosis require a more flexible approach, since it would be preferable to use wide time windows for the analysis of low-frequency signals, and narrow time windows for high-frequency signals. This behavior has been obtained by the development of Wavelet Transform.

2.2.2.3 Wavelet Transform

Wavelet analysis consists of breaking up a signal into shifted and scaled versions of an original wavelet, usually called mother wavelet. A wavelet is a special function of limited duration, with asymmetric waveform, that has an average value of zero. As can be seen, a wavelet is quite different from a sinusoidal wave, which is infinite, smooth and symmetric.

The Continuous Wavelet Transform (CWT) of *f*(t) is defined as the integral over time of the signal, multiplied by scaled and shifted versions of the wavelet function Ψ, and calculates how much similar they are.

$$C(scale, position) = \int_{-\infty}^{\infty} f(t)\psi(scale, position)dt\,. \tag{2.4}$$

The wavelet coefficients are the result of the CWT. Multiplying each coefficient by the appropriately scaled and shifted wavelet yields the constituent wavelet of the original signal (in the same way, multiplying a Fourier coefficient by a sinusoid of appropriate frequency, yields the constituent sinusoidal component of the original signal). Scaling, as a mathematical operation, either dilates or compresses a signal. According to the traditional definition of wavelet transform, the relation between scale and frequency is that low scales correspond to high frequencies and high scales to low frequencies. Consequently, it is possible to analyze a signal at different frequencies with different resolutions. Fig. 2.2 illustrates the aforementioned multiresolution in time-frequency plane.

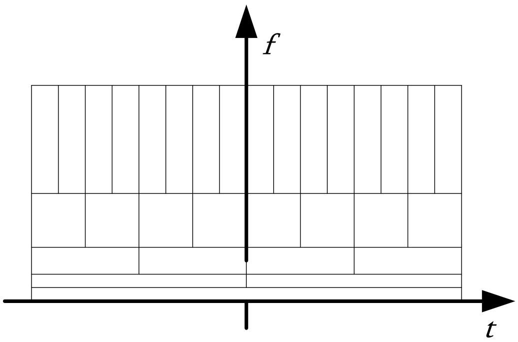

Fig. 2. 2 Multiresolution in time-frequency plane using Wavelet Transform

Calculating the wavelets coefficients at every possible scale and position is a demanding work. As a consequence, a subset of scales and positions, based on power of two is usually chosen (dyadic choice) [11]. In this case, the constituent wavelets of a signal can be found by recursively applying low-pass and high-pass filtering procedures as illustrated by Fig. 2.3.

The choice of the filter determines the shape of the used wavelet and therefore it is very important for the quality and accuracy of the analysis. The low-frequency component of the signal is usually called "approximation signal", whereas the high-frequency component is referred to as "detail signal". However, these two filters produce twice the initial amount of data (if the input signal is composed of *N* input samples, the output signals of the low-pass and hi-pass filters will have *N* samples each), although the total information has not changed. To correct this behavior, the filtering outputs are down-sampled, so that the approximation and detail signals have *N*/2 samples each.

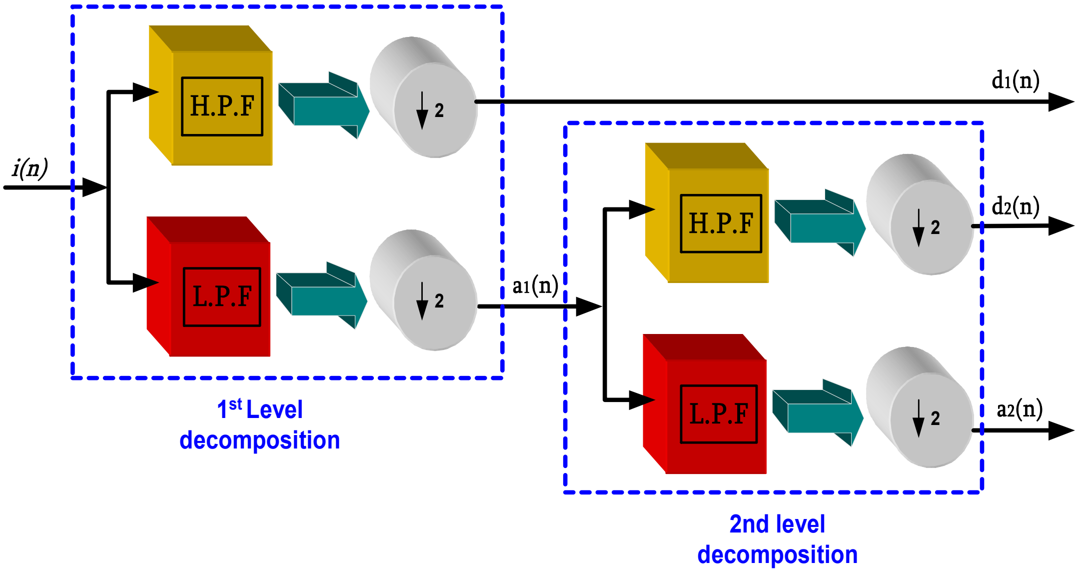

Fig. 2. 3 Wavelet Transform using a filter banks

The approximation signal of level 1, a_1, can be split into a lower-frequency part, i.e., the approximation signal of level 2, a_2, and in a higher-frequency part, i.e., the detail signal of level 2, d_2. Iterating the decomposition process into low-frequency and high-frequency components breaks the input signal into many lower-resolution components, and builds a wavelet decomposition tree.

The original signal $f(t)$ can be reconstructed by combining the approximation a_n and details d_j signals as :

$$f(t) = a_n(t) + \sum_{j=1}^{n} d_j(t) \tag{2.5}$$

where n is the decomposition level, and a_n and d_j are linear combinations of scaling functions $\phi_{i,n}$ and mother wavelet functions $\psi_{i,j}$ at level j :

$$\begin{aligned} a_n(t) &= \sum_{i=1}^{n} c_{i,n}\varphi_{i,n}(t) \\ d_j(t) &= \sum_{i=1}^{n} \beta_{i,j}\psi_{i,j}(t) \end{aligned} \tag{2.6}$$

The coefficient $c_{i,n}$ and $\beta_{i,j}$ are referred to as scaling and wavelet coefficients respectively. With the dyadic down-sampling procedure, the frequency bands of the n-level decomposition are strictly related to the sampling frequency f_s. These bands, given by $[0, 2^{-(n+1)}f_s]$ or $[2^{-(n+1)}f_s, 2^{-n}f_s]$, cannot be changed unless a new acquisition with a different sampling frequency is made, which penalize the memory and latency of processing.

Discrete Wavelet Transform (DWT) provides greater resolution in time for high frequency components, and greater resolution in frequency for low frequency components. So it is particularly suitable for the analysis of transient signals.

Motivated by the above proprieties, DWT have spread in different areas, especially in the last ten years for power systems quality and protections. Fig. 2.4 show the repartition of wavelet applications for different power system areas [16].

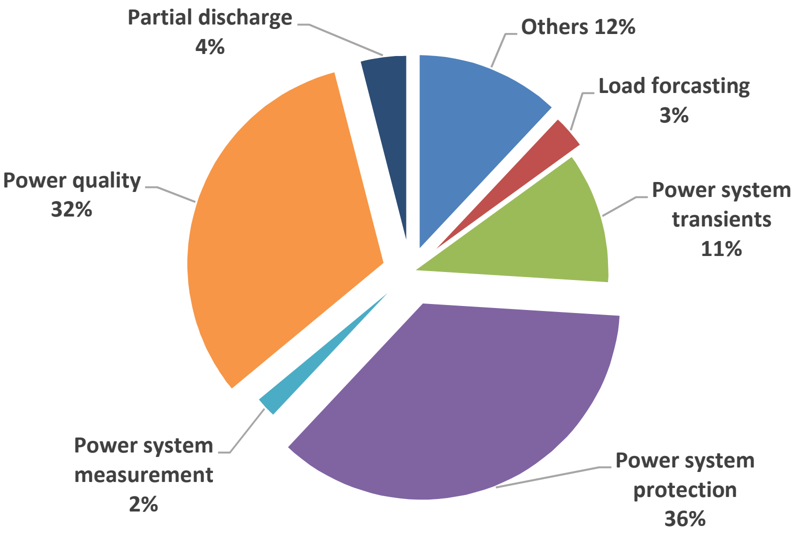

Fig. 2. 4 Percentage of wavelet applications for different power system areas

2.3 Problematic and developed Diagnosis approach

As already established in chapter 1, the need to develop a new diagnostic approach for electrical machines operating in time-varying conditions can be formulated with the following possible improvements over existing techniques: 1) Capability of monitoring the fault evolution continuously over time under any transient operating condition; 2) No requirement for speed/slip measurement or estimation; 3) Higher accuracy in filtering frequency components around the fundamental; 4) Reduction in the likelihood of false indications by avoiding confusion with other fault harmonics (the contribution of the most relevant fault frequency components under speed-varying conditions are clamped in a single frequency band); 5) Low memory requirement due to low sampling frequency; 6) Reduction in the latency of time processing (no requirement of repeated sampling operation).

Electrical machines operate mostly in time-varying conditions. In this context, slip and speed vary unpredictably, and then chains of fault components related to stator or rotor faults, such as $(f_{krs}=(s\pm 2k)f)_{k=0,1,2,\ldots}$, or $(f_{ksr}=(1\pm 2ks)f)_{k=0,1,2,\ldots}$, …, are spread in frequency bands proportional to the speed variation.

In order to carry out a preliminary frequency domain characterization of a stator fault in time-varying conditions, the fault configuration was emulated in a non-destructive way using a wound rotor induction machine (WRIM), experimentally mounted in the laboratory for wind energy application. Since the common effect of both faults is the unbalance of the corresponding winding impedances, the fault configuration was emulated by inserting additional resistances in series to the stator phase winding (R_{add}). FFT was used to carry out a preliminary characterisation of the stator fault in speed-varying conditions, to detect experimentally the contribution of the fault components $(2-s)f$ and $(2+s)f$ under healthy and faulty $(Radd=Rs)$ cases.

Fig. 2.4 shows the experimental rotor modulating signal spectra for large speed transient under healthy (red line) and stationary stator High-resistance connection (blue line). Comparing the spectra of the modulating signals, it is evident that a stator asymmetry produces increments in magnitudes of the components $(2-s)f$ and $(2+s)f$. Moreover, being dependent on slip values, under speed varying conditions, the magnitudes of the above fault components are spread in a bandwidth proportional to the speed variation. Consequently, the use of Fourier transform in these conditions can lead to an erroneous diagnosis.

On the other hand, under intermittent stator fault conditions, where the variation of speed is induced by the degree of the stator unbalance, which justifies the spreading effect (distortions) observed in Fig. 2.5.

Consequently, the use of Fourier transform in these conditions can lead also to an erroneous diagnosis. Moreover, time domain information is lost, and then the first point of the planned improvements “1)” cannot be achieved with this technique.

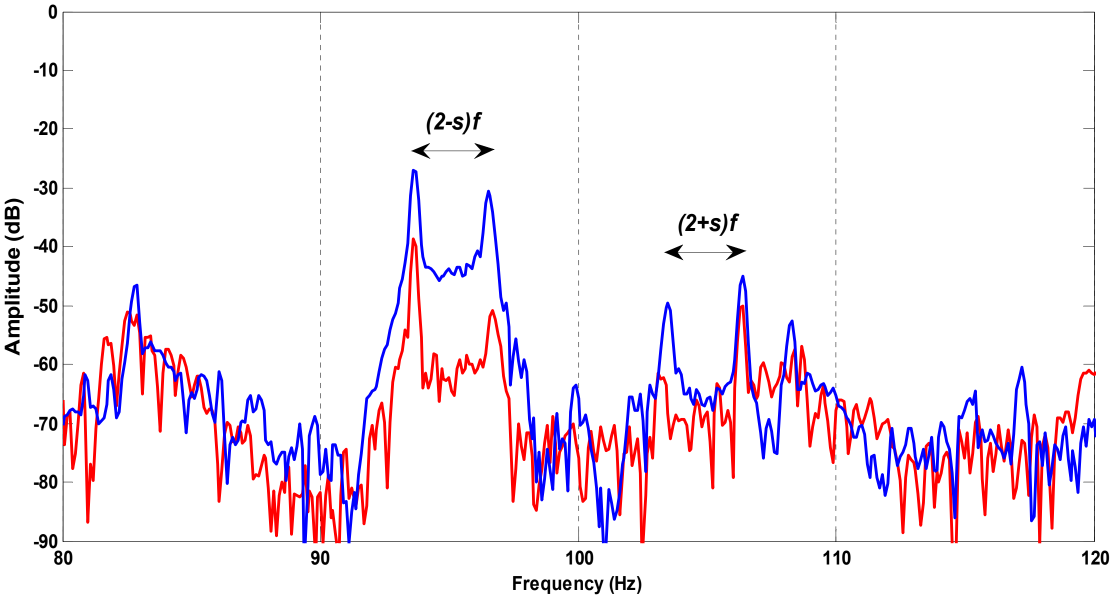

Fig. 2. 5 Experimental results: Rotor modulating signal spectrum for large speed transient under healthy (red line) and stationary stator High-resistance connection (blue line)

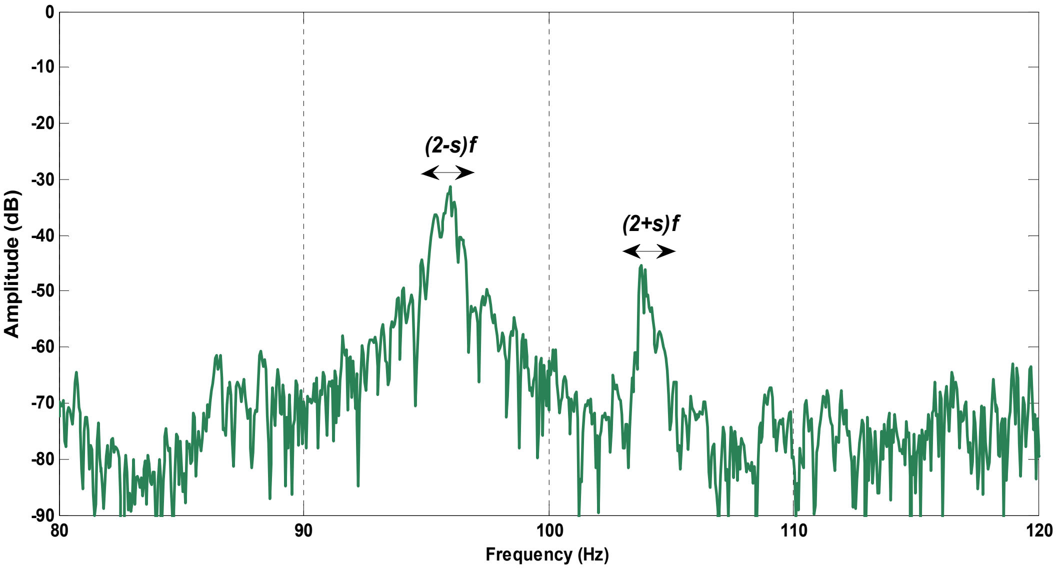

Fig. 2. 6 Experimental results: Rotor modulating signal spectrum for intermittent stator High-resistance connection

In order to overcome the limits of Fourier Transform, and the fixed size of the chosen window for STFT, the main focus of researchers in the field was oriented to the tracking of fault components issued from non-stationary electrical or mechanical signals by mean of Wavelet Transform Analysis [17]-[22].

In Fig. 2.7 a high-level wavelet signals resulting from the DWT of the startup current for: (a) healthy machine and (b) machine with two broken bars are shown. As seen, the diagnosis process is based on the comparative study of the different wavelet analysis under healthy and faulty conditions induced by the spreading effect of the left side band (1-2s)f characteristic of this fault.

Most of the reported contributions are based on wavelet analysis of currents during the start-up phase or during any load variation. In this context, the frequency components are spread in a wide bandwidth as the slip and the speed change considerably. This fact justify the usage of multi-detail or/and approximation signals resulting from the wavelet decomposition [20]–[22].

In fact, the different decomposition levels are imposed by the sampling frequency. However, the dependence on the choice of the sampling frequency and on the capability of tracking multiple fault frequency components makes difficult to interpret the fault pattern coming from wavelet signals and increases the diagnosis complexity.

Another issue is that the use of multi-frequency bands for tracking single fault component subject the process of diagnosis to confusions with other fault components and then the last four points of the planned improvements "3)-6)", in the previous chapter cannot be achieved with a direct use of Discrete Wavelet Transform.

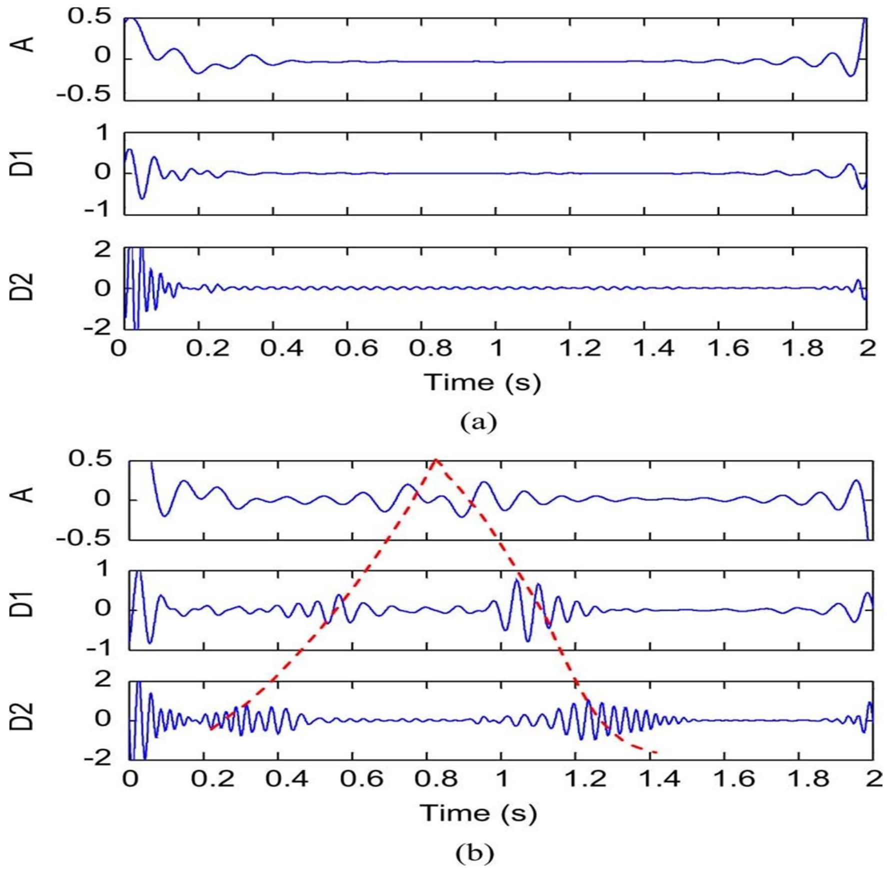

(a)

(b)

Fig. 2. 7 High-level wavelet signals resulting from the DWT of the startup current for: (a) healthy machine and (b) machine with two broken bars.

Then, a more appropriate technique is needed for providing a reliable diagnosis procedure to discriminate healthy from faulty conditions under speed or fault varying conditions.

In the next section, a simple and effective new technique is proposed, providing reliable information in time-frequency domain for diagnosing electrical machines under time-varying operating conditions.

2.4 Proposed diagnostic approach

The principal feature of wavelet analysis is its High Multiresolution Analysis HMRA capability. Wavelet analysis is signal decomposition, using successive combination of approximation and detail signals. The procedure is repeated until the original signal is decomposed to a pre-defined J level decomposition. With the well known dyadic down sampling procedure, frequency bands of each level of decomposition are related to the sampling frequency. Hence, these bands can’t be changed unless a new acquisition with different sampling frequency is made. This fact complicates any fault detection based on DWT, particularly in time-varying condition.

As already analysed in Section 1.2.2, stator fault in induction machines leads to a set of new components at frequencies $(f_{kss}=\pm(1-2k)f)_{k=0,1,2,\dots}$ in the stator currents and $(f_{krs}=(s\pm 2k)f)_{k=0,1,2,\dots}$ in the rotor currents (in case of WRIM where rotor quantities are accessible). Then typically, in case of stator faults, the amplitudes of the sideband components of a phase current are monitored in order to sense their variation in steady state conditions. Fig. 2.8 illustrates an extension of the propagation mechanism corresponding to the evolution of the aforementioned fault components in frequency domain (Section 1.2.2), to time-frequency domain. The periods of the fault harmonics are shown on the x-axis, ordered according to the propagation mechanism, whereas the corresponding frequencies are shown on the y-axis.

Similar considerations can be done for a rotor dissymmetry. In this case, a set of fault components at frequencies $(f_{ksr}=(1\pm 2ks)f)_{k=0,1,2,\dots}$ appears in the spectrum of the stator currents and new fault components at frequencies $(f_{krr}=\pm(1+2k)sf)_{k=0,1,2,\dots}$ appear in the spectrum of rotor currents. The corresponding extension of the propagation mechanism from frequency (section 2.2.2) to time frequency domain is illustrated by Fig. 2.9.

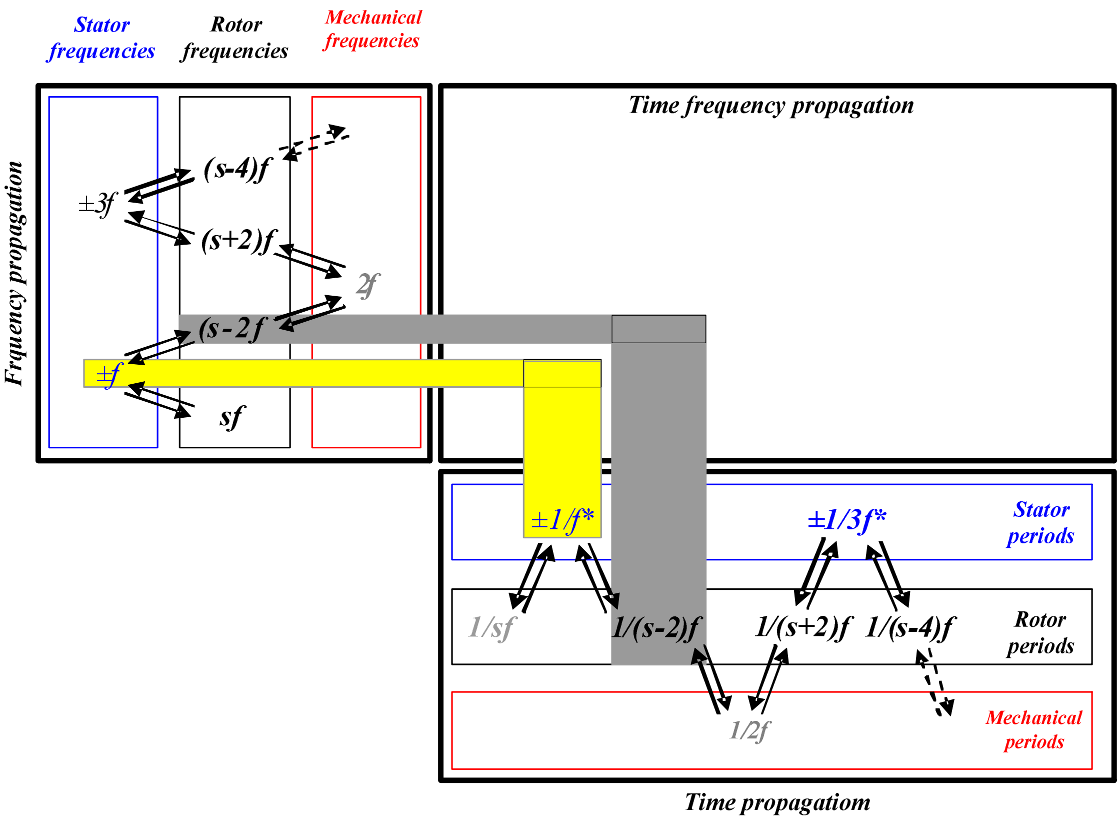

Fig. 2. 8 Time-frequency propagation of a stator fault. The minus sign (–) identifies current inverse sequence components

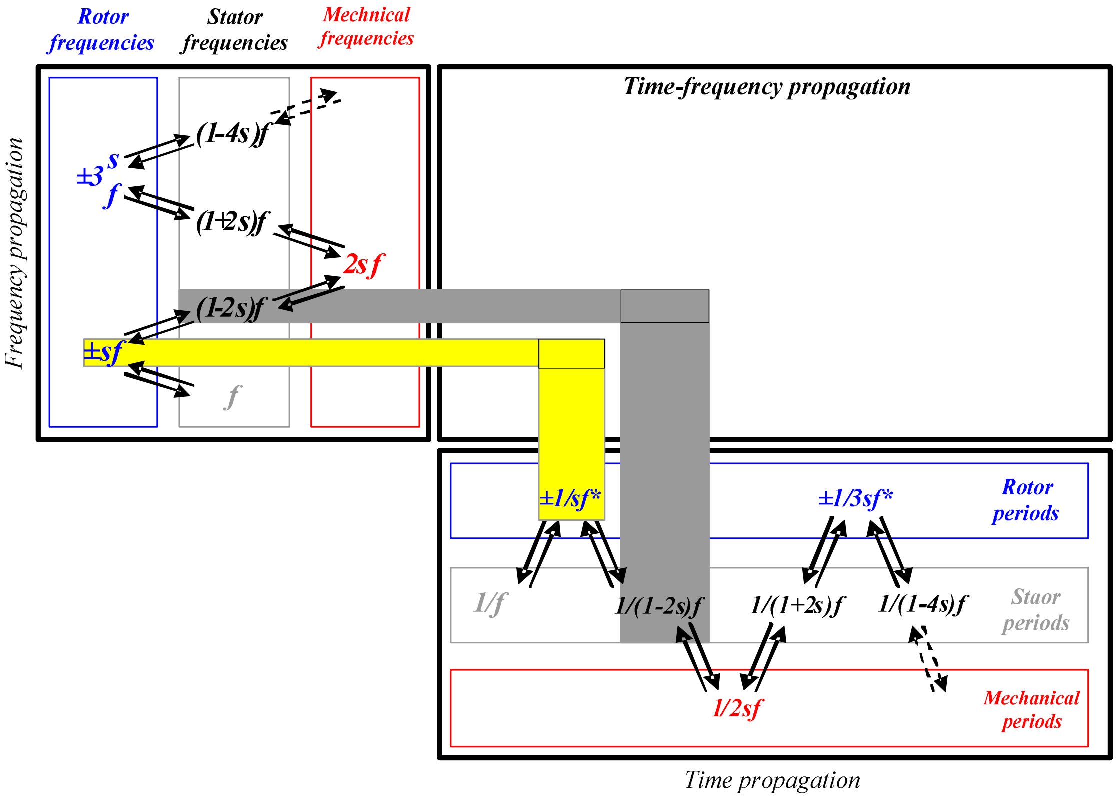

Fig. 2. 9 Time-frequency propagation of a rotor fault. The minus sign (–) identifies current inverse sequence components

Nowadays, most of installed electrical machines operate in time-varying conditions. Under the above conditions the fault components, whose amplitudes must be monitored for diagnostic purposes, are spread in a frequency band proportional to the speed variation. It turns out that the direct application of MCSA, based on Fourier analysis, to the machine currents or to control variables is not adapted.

In the following, an efficient solution is systemized for stator or rotor faults diagnosis in electrical machines.

The main feature of the WT is its capability of multi-resolution analysis. The wavelet analysis is a signal analysis based on a combination of approximation and detail coefficients, via a mother wavelet and scaling functions for J decomposition levels. The level of decomposition J is related to the sampling frequency f_{sam} of the analyzed signal (Table. 2.2) [23], [24].

Once f_{sam} is chosen, the repartition of the frequency bandwidths cannot be changed unless a new acquisition with a different sampling frequency is performed. This dependency complicates the choice of the frequency bands in which the fault frequency components are supposed to be. This is true especially when the influence of the fundamental component has to be avoided because of its proximity to the fault frequency components [25].

Table. 2. 2 Fault harmonics Frequency Bandwidth Repartition

Approximations «a_j »	Frequency Bandwidths (Hz)	Details « d_j »	Frequency bandwidths (Hz)
a_J	$[0, 2^{-(J+1)} f_{sam}]$	d_J	$[2^{-(J+1)} f_{sam}, 2^{-J} f_{sam}]$
⋮	⋮	⋮	⋮
a_2	$[0, 2^{-3} f_{sam}]$	d_2	$[2^{-3} f_{sam}, 2^{-2} f_{sam}]$
a_1	$[0, 2^{-2} f_{sam}]$	d_1	$[2^{-2} f_{sam}, 2^{-1} f_{sam}]$

As previously introduced, stator or rotor faults in wound rotor induction machines can be detected by tracking the evolution of the fault components f_{krs} or f_{krr}, respectively from rotor variables (currents, voltages). Under speed-varying conditions, fault frequency components are spread in a frequency band $[f_{low}, f_{up}]$ related to the speed, where f_{low} and f_{up} denote the lower and upper limits of the fault frequency evolution respectively. A simple processing of the currents or to control variables allows shifting the fault component at frequency f_{krs} or f_{krr} in a dedicated frequency band among those shown in Table 2.2. More in detail, a frequency sliding equal to $f_{sli}^{krs,krr}$ is applied to the rotor variables (currents, voltages) by using (2.7), so that each single fault frequency component is shifted into a prefixed single frequency band.

$$\overline{x}_{sl}^{krs,krr}(t) = \mathrm{Re}\left\{ \overline{x}^{krs,krr}(t)e^{-2\pi i f_{sl}^{krs,krr} t} \right\} \tag{2.7}$$

where $\overline{x}^{krs,krr}$ is the rotor current or voltage space vector, to be analyzed. Then, the discrete WT is applied to the resulting signal $\overline{x}_{sl}^{krs,krr}$ to extract the fault signature in the frequency band that has been chosen.

As illustrated by Fig. 2.10, the DWT divides the frequency content of the original signal into logarithmically spaced frequency bands. The approximation a_J and detail d_J have the same frequency bandwidth, equal to $f_{sam}/2^{J+1}$. Thanks to its proximity to 0 Hz, the approximation a_J is less subject to overlapping effect than detail signals and hence is more suitable for fault analysis [23], [26]. Consequently, the frequency bands $[0,2^{-(J+1)} f_{sam}]$ are chosen to track the main fault components.

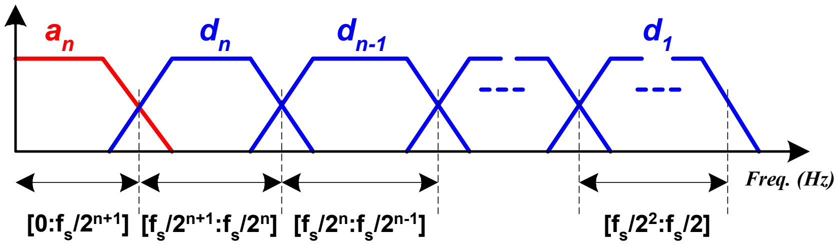

Fig. 2. 10 The DWT filtering process for decomposition of signal into predetermined frequency bands

Being related to the sampling frequency f_{sam}, the level J of decomposition has to be chosen in such a way to satisfy the following criterion:

$$\left|f_{up} - f_{low}\right| < 2^{-(J+1)} f_{sam} \tag{2.8}$$

Condition (2.8) means that the size of the frequency bandwidth in which the fault frequency component evolves should be smaller than the bandwidth related to the approximation signal a_J. Since f_{low} and f_{up} may be affected by uncertainties due to speed ripples or noise, it is convenient to introduce a tolerance factor ξ, slightly greater than one, to avoid false alarms after the fault quantification process.

Thus, the level of decomposition is chosen in order to satisfy the following constraint:

$$J < \frac{\log\left(f_{sam} / \xi\left(f_{up} - f_{low}\right)\right)}{\log(2)} - 1 \tag{2.9}$$

Once the decomposition level has been chosen, the value of the sliding frequency f_{sli} can be computed as follows:

$$f_{sli} = \left(f_{low} + f_{up} - 2^{-(J+1)} f_{sam}\right) / 2 \tag{2.10}$$

With regard to the type of mother wavelet, the use of a low-order Daubechies mother wavelet (db10) has already provided satisfactory results.

Recently, a high order mother wavelet has been recommended to minimize the overlapping effect between adjacent frequency bandwidths, and it has already been tested for rotor broken bars detection [24], [26]. Several types of mother wavelets such as Daubechies, Coiflet, and Symlet have been tested. Regardless of different properties, the qualitative analysis of the results has shown that no significant advantages appeared [27]. The 40th order Daubechies mother wavelet (db40) was adopted in order to minimize the overlapping effect between adjacent frequency bands related to detail d_8 and approximation a_8.

Once the state of the machine has been diagnosed, a quantitative evaluation of the fault degree is necessary. For this purpose, the fault indicator mPa_j at different resolution levels j has been introduced:

$$mPa_j(I,V) = \frac{1}{\Delta n}\sum_{n=1}^{\Delta n}\left|a_j(n)\right|^2 \tag{2.11}$$

where $a_j(n)$ is the approximation signal of interest, Δn denotes the number of samples and j the decomposition level.

The fault indicator is periodically calculated over time, every δn sampling period and over a time interval including the latter Δn samples. This process is shown in Fig. 2.11.

The values of δn and Δn were chosen according to the desired time sensitivity needed to observe the fault evolution. When the fault occurs, the signal energy distribution changes due to the presence of the fault frequency component. Hence, the energy excess confined in the approximation signal may be considered as a fault indicator in case of stator or rotor unbalances.

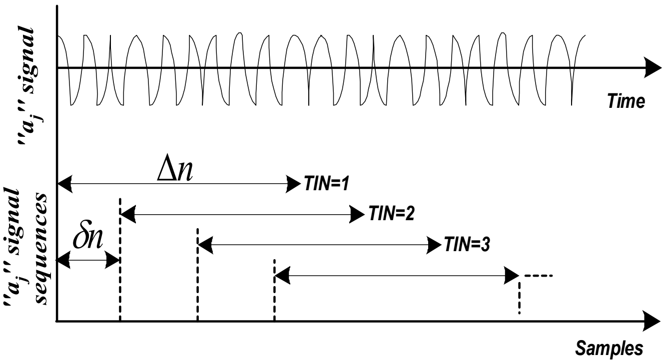

Fig. 2. 11 Principle of time interval calculation as a function of the *Time Interval Number (TIN)*

2.5 Conclusion

The problematic of signal processing techniques used for electrical machine diagnosis operating in time-varying conditions was firstly analyzed in this chapter. Then, a new effective method is completely described and systematized in order to achieve the different open points established in the previous chapter providing:

- Capability of monitoring the fault evolution continuously over time under any transient operating condition;
- Speed/slip measurement or estimation is not required;
- Higher accuracy in filtering frequency components around the fundamental;
- Reduction in the likelihood of false indications by avoiding confusion with other fault harmonics (the contribution of the most relevant fault frequency components under speed-varying conditions are clamped in a single frequency band);
- Low memory requirement due to low sampling frequency;
- Reduction in the latency of time processing (no requirement of repeated sampling operation).

REFERENCES

[1] T. Chow and S. Hai, "Induction machine fault diagnostic analysis using wavelet technique", *IEEE Transactions Industrial Electronics*, Vol. 51, N°. 3, pp. 558–565, Jun. 2004.

[2] Hua Su, Kil To Chong, "Induction Machine Condition Monitoring Using Neural Network Modeling", *IEEE Transactions Industrial Electronics*, Vol. 54, Issue 1, pp. 241 – 249, Feb. 2007.

[3] R.J. Romero-Troncoso, R.A. Osornio-Rios, E. Cabal-Yepez, J.J. Rangel-Magdaleno and L.M. Contreras-Medina, "Novel Methodology for Online Half-Broken-Bar Detection on Induction Motors", *IEEE Transactions on Instrumentation and Measurement*, Vol. 58, N°. 5, May. 2009.

[4] H. Henao, C. Martis, G.A. Capolino, "An Equivalent Internal Circuit of the Induction Machine for Advanced Spectral Analysis", *IEEE Transactions on Industry Applications,* Vol. 40, N°. 3, May/June 2004.

[5] K. Bacha, H. Henao, M. Gossa, G.A. Capolino, "Induction machine fault detection using stray flux EMF measurement and neural network-based decision", *Electric Power Systems Research*, Vol. 78, pp. 1247–1255, 2008.

[6] J. S. Hsu, "Monitoring of defects in induction motors through airgap torque observation", *IEEE Trans. Ind. Appl.*, vol. 31, no. 5, pp. 1016–1021, Sep./Oct. 1995.

[7] C. Kral, R. S. Wieser, F. Pirker, and M. Schagginger, "Sequences of field-oriented control for the detection of faulty rotor bars in induction machines-the Vienna Monitoring Method", *IEEE Transactions Industrial Electronics*, Vol. 47, N°. 5, pp. 1042–1050, Oct. 2000.

[8] D. Casadei, F. Filippetti, C. Rossi, A. Stefani "Closed Loop Bandwidth Impact on Doubly Fed Induction Machine Asymmetries Detection Based on Rotor Voltage Signature Analysis", *43rd International Universities Power Engineering Conference, UPEC 2008.*

[9] A. Stefani, A. Yazidi, C. Rossi, F. Filippetti, D. Casadei and G.A. Capolino, "Doubly Fed Induction Machines Diagnosis Based on Signature Analysis of Rotor Modulating Signals", *IEEE Transactions on Industry Application*, Vol. 44, N° 6, Nov/Dec 2008.

[10] Frédéric Truchetet, « Ondelettes pour le signal numérique », Hermes, Paris 1998, ISBN 2-86601-672-6.

[11] S.G. Mallat, "A Theory for Multiresolution Signal Decomposition: The Wavelet Representation", *IEEE Transactions on pattern analysis and machine intelligence*. Vol. II, N°. 7. July 1989.

[12] R.J.E. Merry, “Wavelet Theory and Applications A literature study”, DCT 2005.53, Eindhoven, June 7, 2005.

[13] I. Daubechies, "Where do Wavelets Come From? A personal Point of view", *Proceedings of the IEEE*, Vol. 84, N°. 4, April 1996.

[14] G.T. Heydet, P.S. Fjeld, C.C. Liu, D. Piercel, L. TU, G. Hensley, "Applications of the windowed FFT to Electric power quality assessment", *IEEE Transactions on Power Delivery*, Vol. 14, N° 4, pp.1411-1416, Oct. 1999.

[15] R. Pineda-Sanchez, M. Riera-Guasp, M. Roger-Folch, J. Hurtado-Perez, E. Perez-Cruz, J. "Improved Resolution of the MCSA Method Via Hilbert Transform, Enabling the Diagnosis of Rotor Asymmetries at Very Low Slip", *IEEE Transactions on Energy Conversion* Vol. 24, Issue 1, pp. 52 – 59, March 2009.

[16] R. de C. Fernandez, H. N. Diaz Rojas, "An overview of wavelet transforms application in power systems", *14th Power Systems Computation Conference*, Session 1, paper 6, Seville, 2002.

[17] J. Antonino-Daviu, P. Jover Rodriguez, M. Riera-Guasp, M. Pineda Sanchez, and A. Arkkio, “Detection of combined faults in induction machines with stator parallel branches through the DWT of the startup current,” *Mech. Syst. Signal Process.*, vol. 23, no. 7, pp. 2336–2351, Oct. 2009.

[18] J. Pons-Llinares, J. A. Antonino-Daviu, M. Riera-Guasp, M. Pineda-Sanchez, and V. Climente-Alarcon, “Induction motor diagnosis based on a transient current analytic wavelet transform via frequency B-splines,” *IEEE Trans. Ind. Electron.*, vol. 58, no. 5, pp. 1530–1544, May 2011.

[19] A. Gandhi, T. Corrigan, and L. Parsa, “Recent advances in modeling and online detection of stator interturn faults in electrical motors,” *IEEE Trans. Ind. Electron.*, vol. 58, no. 5, pp. 1564–1575, May 2011.

[20] A. Ordaz-Moreno, R. J. Romero-Troncoso, J. A. Vite-Frias, J. R. Rivera-Gillen, and A. Garcia-Perez, “Automatic online diagnosis algorithm for broken-bar detection on induction motors based on discrete wavelet transform for FPGA implementation,” *IEEE Trans. Ind. Electron.*, vol. 55, no. 5, pp. 2193–2202, May 2008.

[21] A. Bouzida, O. Touhami, R. Ibtiouen, A. Belouchrani, M. Fadel, and A. Rezzoug, “Fault diagnosis in industrial induction machines through discrete wavelet transform,” *IEEE Trans. Ind. Electron.*, vol. 58, no. 9, pp. 4385–4395, Sep. 2011.

[22] J. Antonino-Daviu, S. Aviyente, E. G. Strangas, and M. Riera-Guasp, “Scale Invariant Feature Extraction Algorithm for the Automatic Diagnosis of Rotor Asymmetries in Induction Motors”, *IEEE Trans. Ind. Inf.*, vol. 9, no. 1, pp. 100–108, Feb. 2013.

[23] T. K. Sarkar, C. Su, R. Adve, M. S. Palma, L. G. Castillo, and R. Boix, “A tutorial on wavelets from an electrical engineering perspective, Part 1: Discrete wavelet techniques,” *IEEE Antennas Propag. Mag.*, vol. 40, no. 5, pp. 49–68, Oct. 1998.

[24] M. Riera-Guasp, J.A. Antonino, J. Roger-Folch, M.P. Molina, “The use of the wavelet approximation signal as a tool for the Diagnosis and quantification of Rotor Bar Failures, ” *IEEE Trans. Ind. App.*, vol. 44, no. 3, pp. 716–726, May./Jun. 2008.

[25] M.R. Guasp, J.A. Daviu, M.P. Sanchez, R.P. Panadero, J.P. Cruz, “A general approach for the transient detection of slip-dependent fault components based on the discrete wavelet transform,” *IEEE Trans. Ind. Elec.*, vol. 55, no. 12, pp. 4167–4180 Dec. 2008.

[26] S. H. Kia, H. Henao, and G. A. Capolino, “Diagnosis of broken-bar fault in induction machines using discrete wavelet transform without slip estimation,” *IEEE Trans. Ind. Appl.*, vol. 45, no. 4, pp. 1395–1404, Jul./Aug. 2009.

[27] J. Antonino-Daviu, M. Riera-Guasp, J. Roger-Folch, F. Martínez-Giménez, A. Peris, “Application and optimization of the discrete wavelet transform for the detection of broken rotor bars in induction machines,” *Appl. Comp. Harmon. Anal.*, vol. 21, no. 2, pp. 268–279, Sep. 2006.

CHAPTER 3 : ANALYSIS OF STATOR AND ROTOR FAULTS IN WOUND ROTOR INDUCTION MACHINES

3.1 Introduction

In this chapter, the proposed diagnosis technique presented in Chapter 2 is validated for the detection of electrical faults in three-phase wound-rotor induction machines (WRIMs). In the considered application, the rotor windings are supplied by a static converter for the control of active and reactive power flows exchanged between the machine and the electrical grid. In this application, the proposed diagnosis approach was applied for processing the rotor-voltage commands under time-varying conditions. Thus, the time evolution of fault components can be effectively analyzed. Moreover, the relevance of the fault components computed from rotor voltages in comparison to those coming from rotor currents under closed-loop operation is evaluated. Results issued from the quantitative evaluation process of the fault extend issued from the wavelet analysis are presented showing accurate stator- or rotor-fault detection. Simulation and experimental results show the validity of the proposed method, leading to an effective diagnosis procedure for both stator and rotor electrical faults in WRIMs.

3.2 System description

3.2.1 WRIM Control system

In this application, the wound-rotor induction machine is fed by a back-to-back converter on the rotor side and with the stator directly connected to the grid. A Stator Flux Oriented Control (SFOC) system is implemented to regulate rotor currents, in order to control separately the active and reactive power on the stator side [1]-[3]. In the *dq* reference frame rotating synchronously with the stator flux, the stator voltages and fluxes can be written as follows:

$$v_{ds} = R_s i_{ds} + \frac{d\psi_{ds}}{dt} - \omega\, \psi_{qs} \tag{3.1}$$

$$v_{qs} = R_s i_{qs} + \frac{d\psi_{qs}}{dt} + \omega\, \psi_{ds} \tag{3.2}$$

$$\psi_{ds} = L_s i_{ds} + L_m i_{dr} \tag{3.3}$$

$$\psi_{qs} = L_s i_{qs} + L_m i_{qr} = 0 \tag{3.4}$$

The above equations mean that the *d*-axis is in phase with stator-flux vector. In steady-state conditions, by neglecting the stator-phase resistance and by introducing the magnetizing current $\overline{i}_{ms} = \overline{\psi}_s / L_m$ the stator voltage and current components become:

$$v_{ds} \cong 0 \tag{3.5}$$

$$v_{qs} \cong |\bar{v}_s| \cong \omega \, \psi_{ds} \tag{3.6}$$

$$i_{ds} = \frac{L_m}{L_s}\left(i_{dms} - i_{dr}\right) \tag{3.7}$$

$$i_{qs} = -\frac{L_m}{L_s} i_{qr} \tag{3.8}$$

The active and reactive power are expressed as:

$$P_s = \frac{3}{2}\left(v_{ds} i_{ds} + v_{qs} i_{qs}\right). \tag{3.9}$$

$$Q_s = \frac{3}{2}\left(v_{qs} i_{ds} - v_{ds} i_{qs}\right). \tag{3.10}$$

By introducing (3.5)–(3.8) in (3.9) and (3.10), it is possible to rewrite the active and reactive power as function of stator-voltage and rotor-current components as:

$$P_s \cong -\frac{3}{2} \cdot |\bar{v}_s| \cdot \frac{L_m}{L_s} i_{qr} \tag{3.11}$$

$$Q_s \cong \frac{3}{2} \cdot |\bar{v}_s| \cdot \frac{L_m}{L_s}\left(\frac{|\bar{v}_s|}{2\pi f L_m} - i_{dr}\right) \tag{3.12}$$

Using (3.11) and (3.12) and assuming constant stator-voltage magnitude $|V_S|$ and frequency f, it is possible to consider the stator active power proportional to the q-axis rotor-current component i_{qr} and the stator reactive power related to the d-axis rotor-current component i_{dr}.

The DFIM control system (Fig. 3.1) is based on two cascaded loops. The outer loop is dedicated to the stator active and reactive power control, whereas the inner loop is related to the control of the *dq* components of the rotor current. Since the control system is symmetrical, the PI regulators have the same parameters for the *d*- and the *q*-axes loops.

The two PI regulators of the outer loop are used to determine the *dq* components of the rotor-current references on the basis of the active and reactive power errors.

The two PI regulators of the inner loop are used to determine the *dq* components of the rotor modulating signals using the *dq* rotor-current errors as input variables.

The transformations from three-phase quantities in a *dq* stationary reference frame and the inverse transformations are performed by the blocks D and D^{-1}, respectively. Being θ and θ_r, the stator-flux-phase and the rotor-position angles, respectively, the block T(θ) represents the transformation from a stationary reference frame to a synchronous rotating reference frame, as well as the block T($\theta - \theta_r$) represents the transformation from a rotor reference frame to a synchronous reference frame. The blocks $T^{-1}(\theta)$ and $T^{-1}(\theta - \theta_r)$ represent the corresponding inverse transformations.

The control algorithm computes the phase angle θ of the stator-flux vector using the components of the magnetizing current space vector $i^s{}_{dms}$, $i^s{}_{qms}$ in the stator reference frame as:

$$\theta = \arctan\left(\frac{i^s_{qms}}{i^s_{dms}}\right) \tag{3.13}$$

In order to increase the accuracy in the computation of the angle θ, a complex digital filter is applied to detect the fundamental frequency component of the magnetizing-current space vector $\overline{i}^s_{ms}$.

The transfer function of the digital filter in terms of Laplace transform is derived as follows.
In the synchronous reference frame which rotates at a constant angular speed $2\pi f$, the filtered magnetizing-current vector $\overline{i}_{ms(fil)}$ is obtained by applying a first-order low-pass filter to the magnetizing-current vector $\overline{i}_{ms}$, yielding

$$\overline{i}_{ms(fil)} = \frac{1}{1+\tau s}\overline{i}_{ms} \tag{3.14}$$

where τ is the low-pass-filter time constant. The magnetizing-current vector in the synchronous reference frame is related to the magnetizing-current vector in the stationary reference frame by the following relationship:

$$\overline{i}_{ms} = \overline{i}^s_{ms} e^{-j\theta_s} \tag{3.15}$$

By introducing (3.15) in (3.14), the equation of the filtered magnetizing-current vector in the stationary reference frame becomes:

$$\overline{i}^s_{ms(fil)} = \frac{1}{1+\tau \mathrm{s} - j\omega\tau}\overline{i}^s_{ms} \tag{3.16}$$

where ω is the stator-flux angular frequency, assumed constant and equal to $2\pi f$[rad/s]. Then, the dq components of the magnetizing-current vector can be derived from (3.16), yielding:

$$i^s_{msd(fil)} = \frac{(1+\tau \mathrm{s})i^s_{msd} - \omega\tau i^s_{qms}}{(1+\tau \mathrm{s})^2 + \omega^2\tau^2} \tag{3.17}$$

$$i^s_{qms(fil)} = \frac{\omega\,\tau i^s_{dms} + (1+\tau \mathrm{s})i^s_{qms}}{(1+\tau \mathrm{s})^2 + \omega^2\tau^2} \tag{3.18}$$

Equations (3.13), (3.17) and (3.18) are implemented in the block $\left|\bar{i}_{ms}\right|-\theta$ of Fig. 3.1.

The block *Act–React* of Fig. 3.1 calculates the active and reactive power by using (3.9) and (3.10).

For computer simulations, an analytical three-phase model of the WRIM and its control system has been implemented in Matlab-Simulink. As detailed in Appendix.1 a transient general model was adopted for wind power generation systems. In this model, coordinate transformations are not utilized and equations are written for every stator and rotor phase. Moreover stator variables and parameters are referred to the stator reference frame, whereas rotor variables and parameters are referred to the rotor reference frame. This means that every parameter present in the model is the true physical parameter of every single phase winding. This choice was done since in a wound rotor induction machines both rotor and stator terminals are accessible allowing the measurement of all the necessary phase parameters [3]-[4]. The model was modified in order to manage all the machine parameters for emulating different configurations of stator or rotor fault varying conditions.

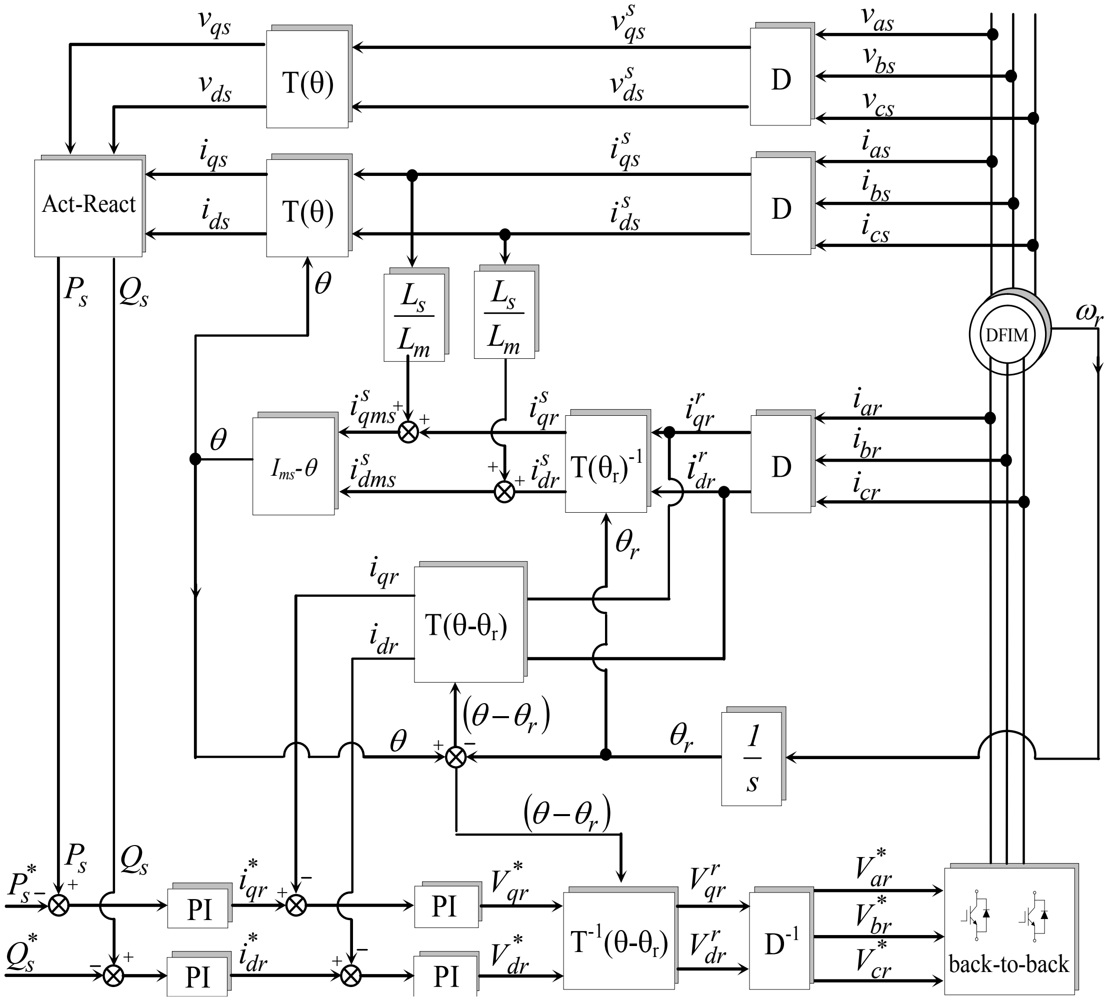

Fig. 3. 1 Block-scheme representation of the complete WRIM control system

3.2.2 Experimental system

The experimental setup (Fig. 3.2) consists of a 5.5-kW 220- V/ 380-V 50-Hz four-pole WRIM connected to a pulse width modulated back-to-back power converter on the rotor side. The generator is driven by a 9-kW dc motor fed by a commercial speed-controlled dc/dc converter. The field-oriented control for the WRIM has been implemented on a dSPACE DS1103 board. Since the speed of the WRIM is not fixed by the control system (because the WRIM set points are the active and reactive powers), the rotor speed is determined by the dc motor and can be varied by acting on the corresponding set point.

For the assessment of the fault diagnosis algorithm, the grid voltages, the rotor-side line currents, the reference rotor voltages, the rotor and stator currents, and the rotor speed are sampled at 3.2 kHz with a data acquisition window of 10 s. Finally, the frequency bandwidth of the current loops has been set to 100 Hz. Other parameters of the experimental setup, used also for the simulations, have been reported in Tables. 3.1-3.3.

Since the common effect of both stator and rotor faults is the imbalance of the corresponding winding impedances, the fault configurations have been emulated in a nondestructive way by increasing the stator or the rotor phase resistances with additive components (R_{add}). During the tests, active and reactive power set points at the stator side are kept equal to 5.5 kW and 4.1 kVA, respectively.

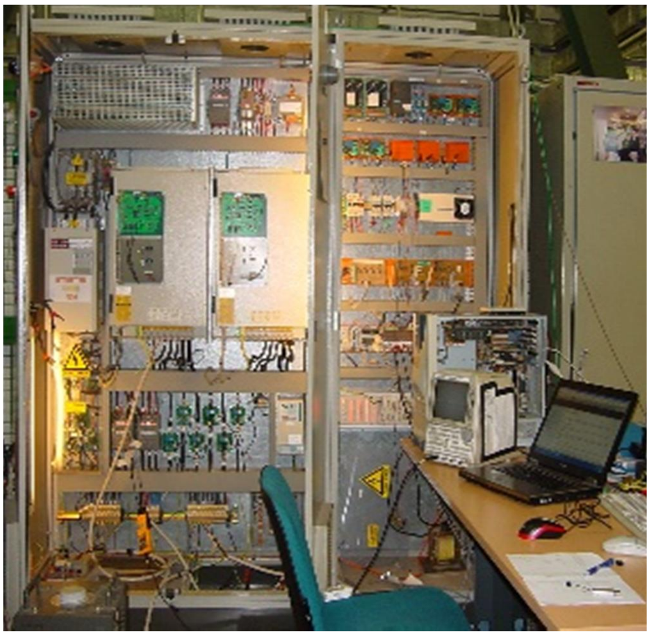

(a)

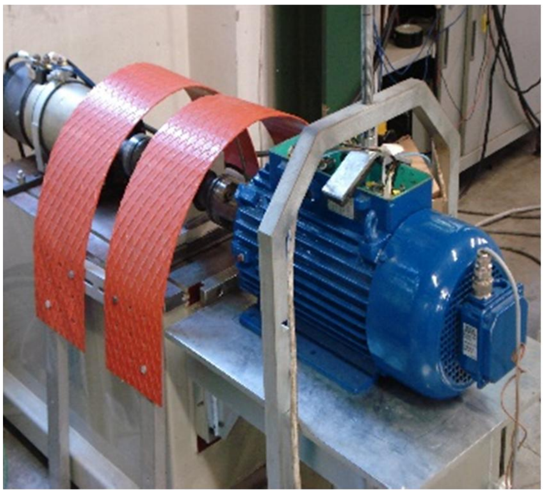

(b)

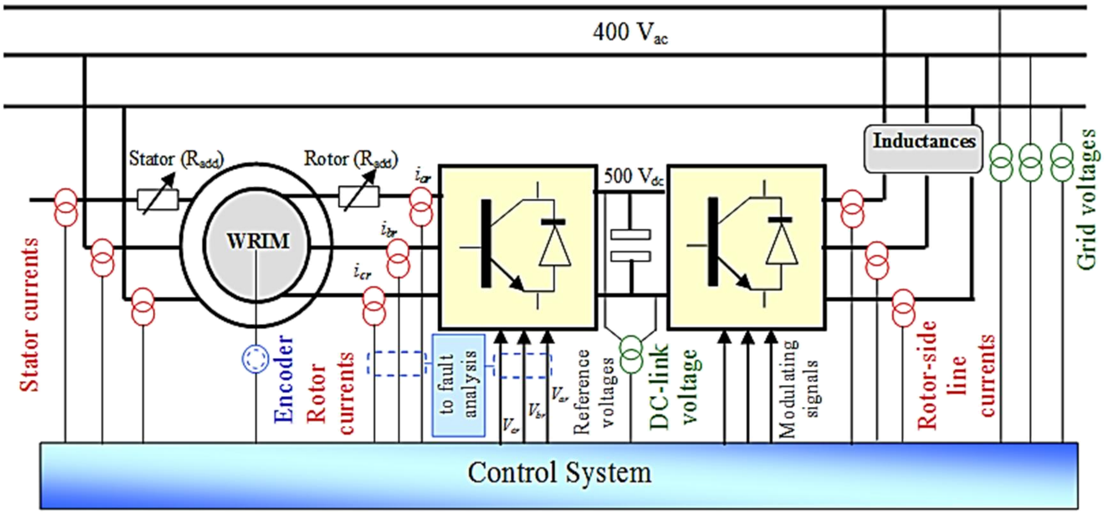

c)

Fig. 3. 2 Experimental set-up. a) Power converter cabinet. b) WRIM and prime mover. c) Schematic diagram of the test bench and position of the current and voltage sensors.

Table. 3. 1 WRIM parameters

Parameter	*Value*	
Rated power	kW	5.5
Rated stator/ rotor voltage	V	380/186
Rated frequency	Hz	50
Rated speed	rpm	1400
Stator phase resistance	Ω	0.531
Rotor phase resistance	Ω	0.310
Stator inductance	H	0.083
Rotor inductance	H	0.019
Mutual inductance	H	0.038
Pole pairs		2

Table. 3. 2 Back-to-Back Converter Parameters

Parameter	*Value*	
Grid side converter switching frequency	kHz	10
Rotor side converter switching frequency	kHz	12
Grid phase-to-phase voltage	V	400
Grid coupling inductance	mH	1.2
DC-link voltage	V	500

Table. 3. 3 Sensors

Parameter	*Value*	
Current sensor type		LA100
Current sensor accuracy (@25°C)	%	0.45
Current sensor bandwidth (-1 dB)	kHz	200
Voltage sensor type		DV1200
Voltage sensor accuracy (@25°C)	%	0.3
Voltage sensor bandwidth (-1 dB)	kHz	6.5
Encoder type	Imp/turn	1024

3.3 Results

3.3.1 Fault detection under speed-varying condition

It is important to notice that the propagation mechanisms propagation of stator and rotor faults analyzed in frequency domain (sections 1.2.2 and 2.2.2), and extended to time frequency domain in Section 2.4 are valid under the assumption of open-loop systems. The behavior of the machine may be different if it is controlled under closed loop. In this case, the control system is normally able to ensure the correct operation even under small unbalances in both stator and rotor windings. In fact, the presence of the current harmonics is usually detected and the current regulators tend to track the sinusoidal references and to drive to zero the residual errors. The capability of the control system to compensate the current harmonics depends mainly on the frequency of the fault harmonics. If this frequency is outside the bandwidth of the control system, the current regulators cannot affect the amplitude of current harmonics. On the contrary, if the frequency of the unbalance harmonics is within the bandwidth of the control system, the control system can sensibly reduce the amplitude of the fault harmonics according to the gain of the control loop at those frequencies. This behavior is due to the current regulators that naturally applies suitable voltage harmonics to cancel the corresponding current harmonics. At the same time, torque and speed oscillations are accordingly damped.

Since the bandwidth of the current loops is usually quite wide, the reduction effect on the main fault frequencies may be remarkable, and the fault frequencies are expected to appear in the voltage set-points at the output of the current regulators [5].

In the case of the WRIM-based system of Fig. 3.1, the rotor-current fault frequency components may become less notable due to the compensating action of the control system. However, these fault-related frequencies become clearly visible in the modulating signals of the rotor voltages, which can be considered as a new effective diagnostic index. In other words, a stator fault is expected to generate a relevant harmonic at $(s\text{-}2)f$ in the spectrum of the rotor voltages, whereas a rotor fault is expected to generate a negative sequence harmonic at $-sf$. The detection of the inverse sequence frequency components at $(s\text{-}2)f$ and $-sf$ is possible only by analyzing the rotor voltage space vector. Initially, the performance of the WRIM has been verified in healthy condition during a speed transient from 1395 to 1305 r/min. With a sampling frequency f_{sam} of 3.2 kHz, an eighth-level decomposition ($J = 8$) has been chosen to track the components $f_{rs} = (s - 2)f$ and $f_{rr} = -sf$ in the time domain. The computed values of frequency sliding are 98.125 and 8.125 Hz, respectively.

3.3.1.1 Stator dissymmetry detection

This fault configuration has been simulated by means of an additional resistance R_{add} connected in series with one stator phase winding and equal to the phase resistance R_s. Rotor currents and voltages, used for space vectors $(i_r,V_r)^{rs}$ computation under healthy and faulty conditions, have been recorded. Simulation results are shown in Figs. 3.3 and 3.4, which compare the WRIM operation in both healthy and fault conditions. Figs. 3.5 and 3.6 show the behavior of the WRIM during the experimental tests under the same operating conditions.

The contribution of the stator fault component at frequency $(s\text{–}2)f$ must be extracted from both rotor current and voltage space vectors. The 8th-level approximations coming from the discrete WT of $I_{sl}^{rs}(t)$ and $V_{sl}^{rs}(t)$ in healthy and fault conditions have been computed under the assumption of a sliding frequency f_{sli}^{krs} equal to 98.125 Hz. In healthy condition, the approximation a_8 does not show any variation. This fact indicates the absence of any fault component at frequency $(s\text{-}2)f$, in both rotor currents and voltages, thus leading to diagnose the healthy condition of the WRIM even under speed-varying operation.

In the case of stator unbalance ($R_{add}=R_s$), the approximation a_8 issued from rotor currents analysis does not show any significant change. This is mainly due to the compensating action of the control system under fault condition [5]. However, for the same stator unbalance, large oscillations appear in the approximation a_8 issued from the rotor voltages. These oscillations have a constant magnitude depending on the unbalance degree (R_{add}=R_s). The frequency variations of the oscillations during the transient is due to the slip-dependency of the fault component at *(s-2)f*.

As can be seen, this behavior is confirmed not only by the simulation results, but also by the experimental tests (Figs. 3.5 and 3.6), although in some cases the magnitude variations have been even greater in the experimental tests compared to what has been observed in the simulations.

In particular, Fig. 3.6 shows that the ratio between the amplitude of the approximation signal a_8 (≅ 0.5A) and the amplitude of the current (≅ 29A) is less than 0.017, whereas the ratio between the amplitude of the approximation signal a_8 (1.2V) and the amplitude of the voltage (27V before the speed step and 40 V after the speed step) varies from 0.044 to 0.030. In other words, the effect of the unbalance is from two to three times more visible in the voltage signals than in the current signals.

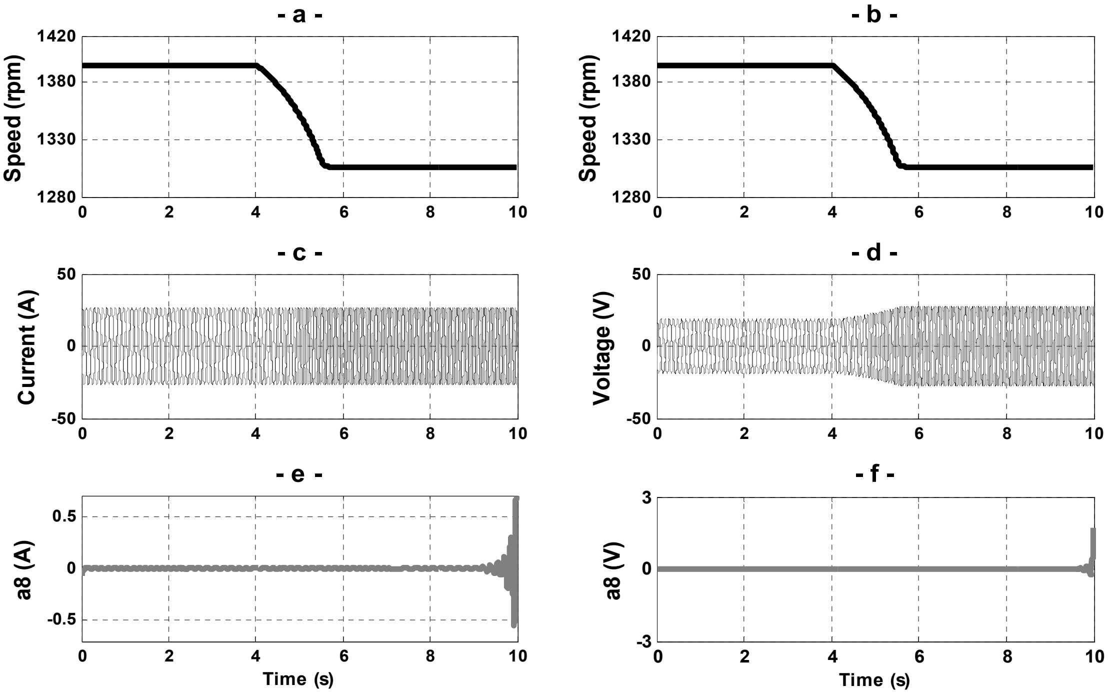

Fig. 3. 3 Discrete WT of I_{sl}^{krs} and V_{sl}^{krs} in healthy condition (R_{add}=0) under speed transient (simulation results)

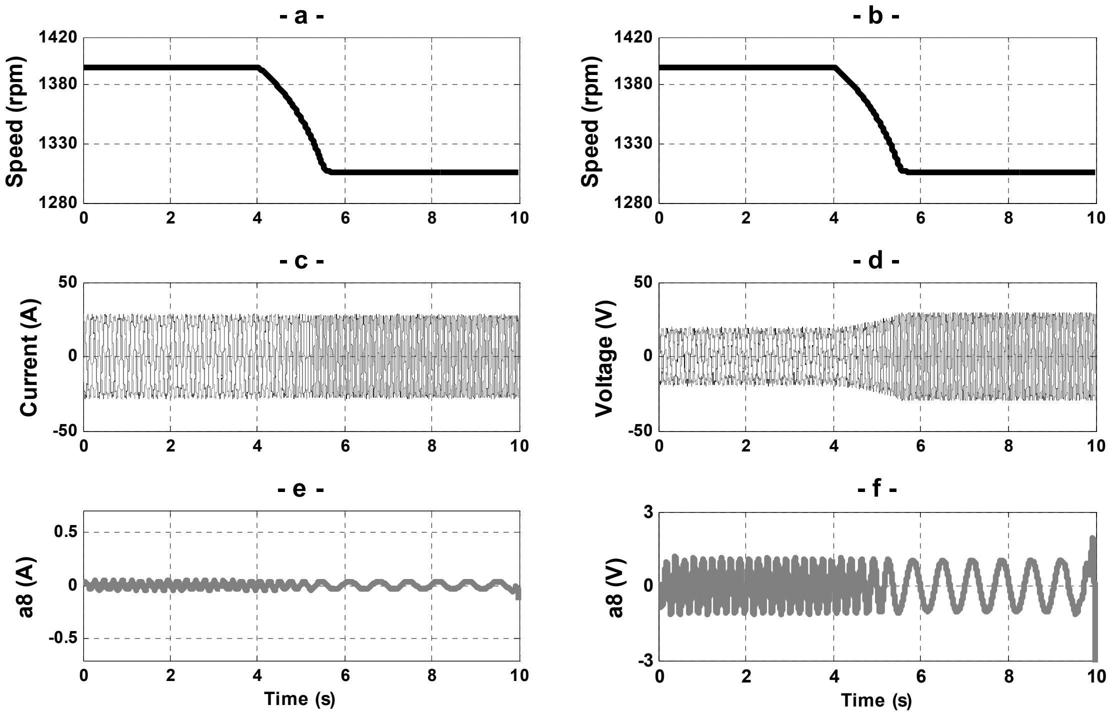

Fig. 3. 4 Discrete WT of I_{sl}^{krs} and V_{sl}^{krs} in faulty condition (R_{add}=R_s) under speed transient (simulation results)

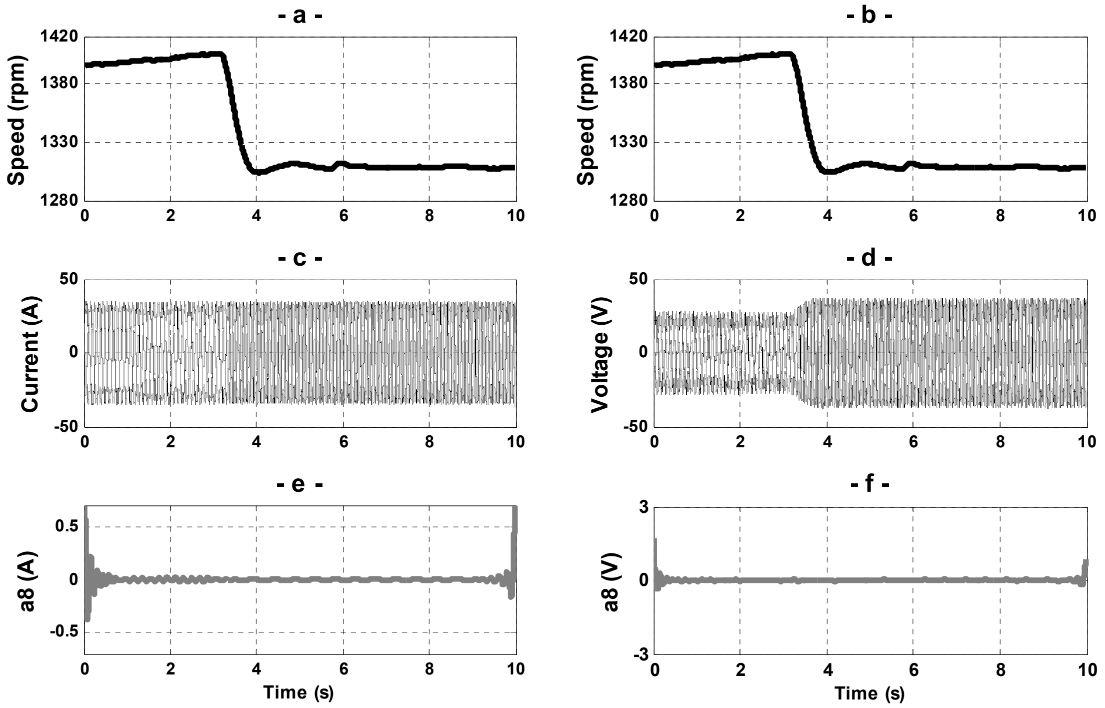

Fig. 3. 5 Discrete WT of I_{sl}^{krs} and V_{sl}^{krs} in healthy condition (R_{add}=0) under speed transient (experimental results)

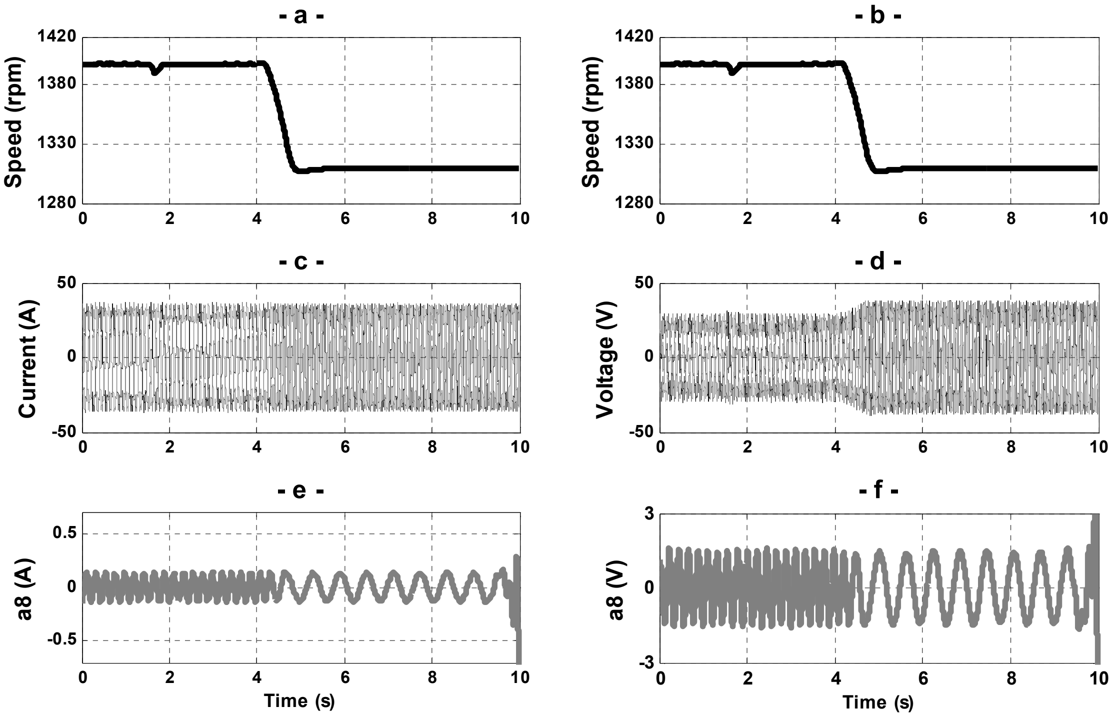

Fig. 3. 6 Discrete WT of I_{sl}^{krs} and V_{sl}^{krs} in faulty condition (R_{add}=R_s) under speed transient (experimental results)

3.3.1.2 Rotor dissymmetry detection

The same process has been repeated for the analysis of a rotor unbalance simulated by an additive resistance connected in series with a rotor phase and equal to its own resistance. In order to detect such a fault, the contribution of the rotor fault component at frequency $-sf$ has to be extracted from the rotor current and voltage space vectors. Rotor currents and voltages have been recorded for the computation of the space vectors $(i_r,V_r)^{rr}$ in healthy and faulty conditions. The simulation results, shown in Figs. 3.7 and 3.8, show a good agreement with the corresponding experimental tests, shown in Figs. 3.9 and 3.10. With similar considerations as for the stator fault, the signals $I_{sl}^{rr}(t)$ and $V_{sl}^{rr}(t)$ have been computed by using f_{sli}^{krs}=8.125 Hz. The aim of this pre-processing operation is to identify the contribution of the negative sequence frequency $-sf$ in the frequency band of the 8th approximation signal. Approximations a_8 coming from the discrete WT of signals $I_{sl}^{rr}(t)$ and $V_{sl}^{rr}(t)$ under both healthy and faulty conditions have been computed. In healthy condition, the approximation a_8 does not show any oscillation since the fault components at frequency $-sf$ in both rotor currents and voltages are not involved. This fact indicates a reliable diagnosis of healthy condition for the WRIM under speed-varying operation.

Under rotor unbalance (R_{add}=R_r), the same conclusion as for a stator unbalance has been obtained. The approximation a_8 coming from the rotor voltages shows large amplitude variations reflecting the presence of the fault frequency component -*sf*. Despite the speed transient, the oscillations reproducing the fault frequency evolution -*sf* are still significant. On the contrary, the variation of a_8 calculated for the rotor currents is small compared to the amplitude of the currents (Fig. 3.8). Experimental results under healthy and faulty ($R_{radd}=R_r$) conditions have confirmed this behavior (Figs. 3.9 and 3.10). More accurately, the contribution of the negative sequence at the frequency -*sf* under a rotor unbalance coming from the rotor voltages is more important than the corresponding one coming from rotor currents.

In conclusion, the experimental results are in total agreement with the simulation, thus proving the effectiveness of the proposed approach for the diagnosis of electrical rotor faults in a WRIM.

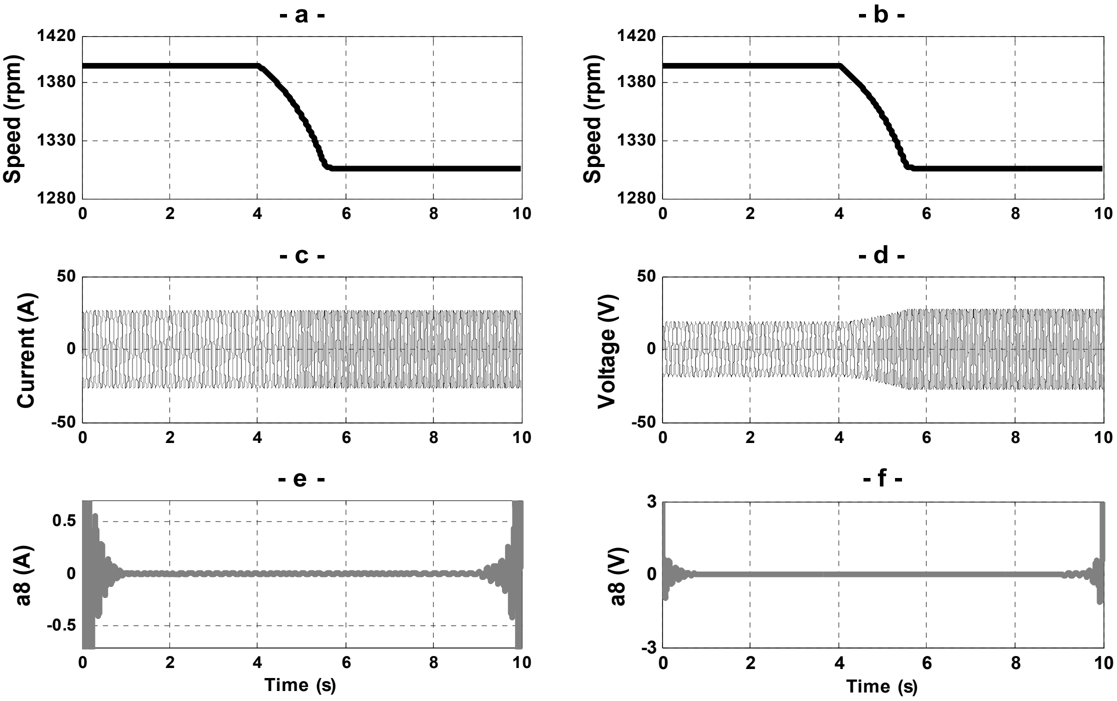

Fig. 3. 7 DWT of the signals I_{sl}^{krr} and V_{sl}^{krr} in healthy condition (R_{add}=0) under speed transient (simulation results)

3.3.2 Fault detection under fault-varying conditions

The results obtained in Section IV prove that the wavelet signal a_8 is sensitive enough to diagnose either stator or rotor winding unbalances in any WRIM operating conditions. This fact confirms the validity of the proposed technique applied to rotor voltages even in presence of slip variations.

In this section, the sensitivity of the proposed diagnostic technique is evaluated by the analysis of progressive stator and rotor winding unbalances. These fault configurations have been simulated through a ramp of resistance increment from R_{add}=0 to $R_{add}=1.3R_s$ or $R_{add}=1.3R_r$ under stator or rotor progressive unbalance respectively. The experimental set-up has been designed to emulate these situations by inserting an external variable resistance in series to a stator or a rotor phase. For the above listed tests, the WRIM operates in steady-state condition at the rated speed of 1400rpm.

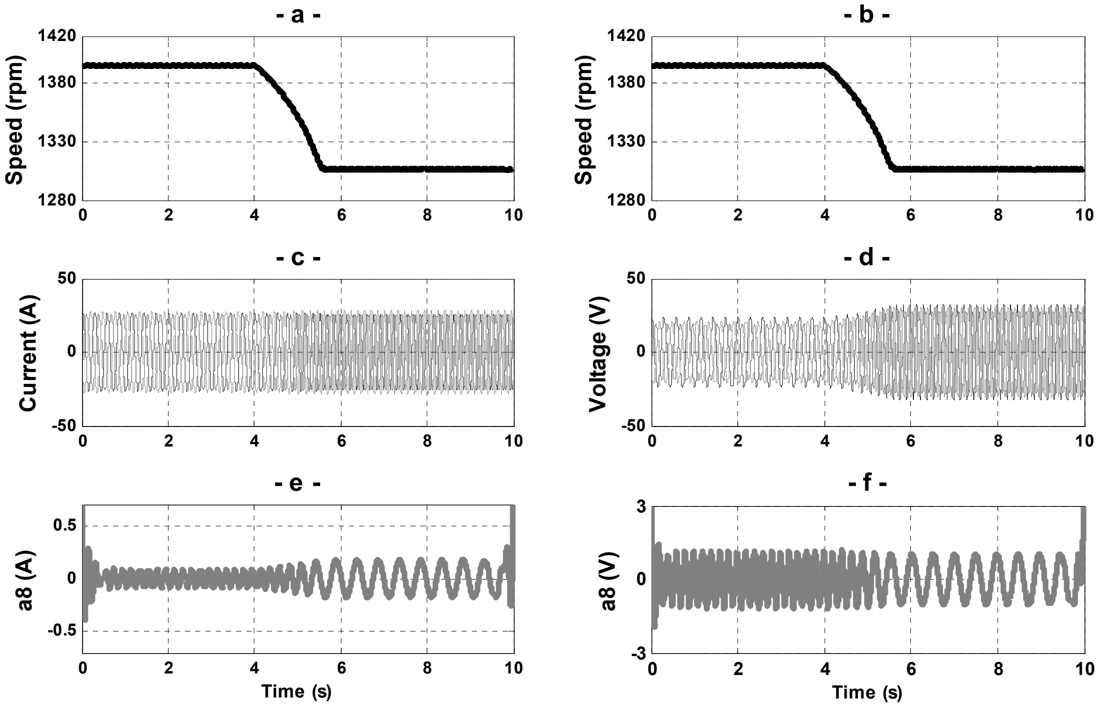

Fig. 3. 8 DWT of the signals I_{sl}^{krr} and V_{sl}^{krr} in faulty condition (R_{add}=R_r) under speed transient (simulation results)

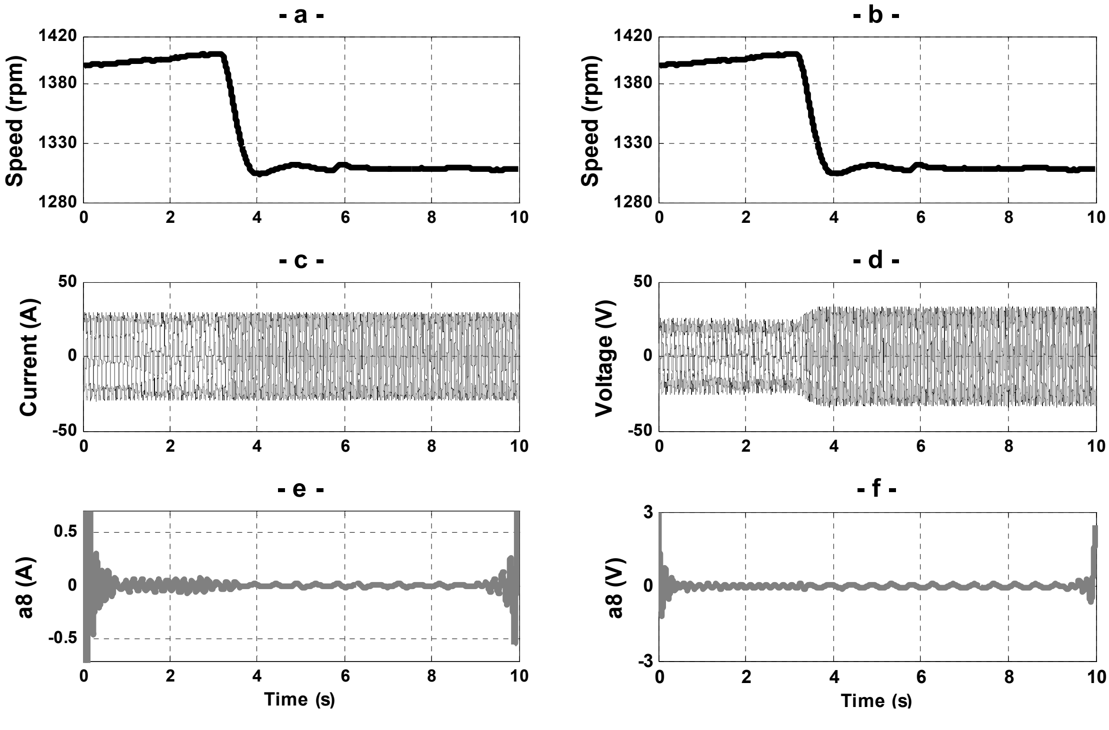

Fig. 3. 9 DWT of the signals I_{sl}^{krr} and V_{sl}^{krr} in healthy condition (R_{add}=0) under speed transient (experimental results)

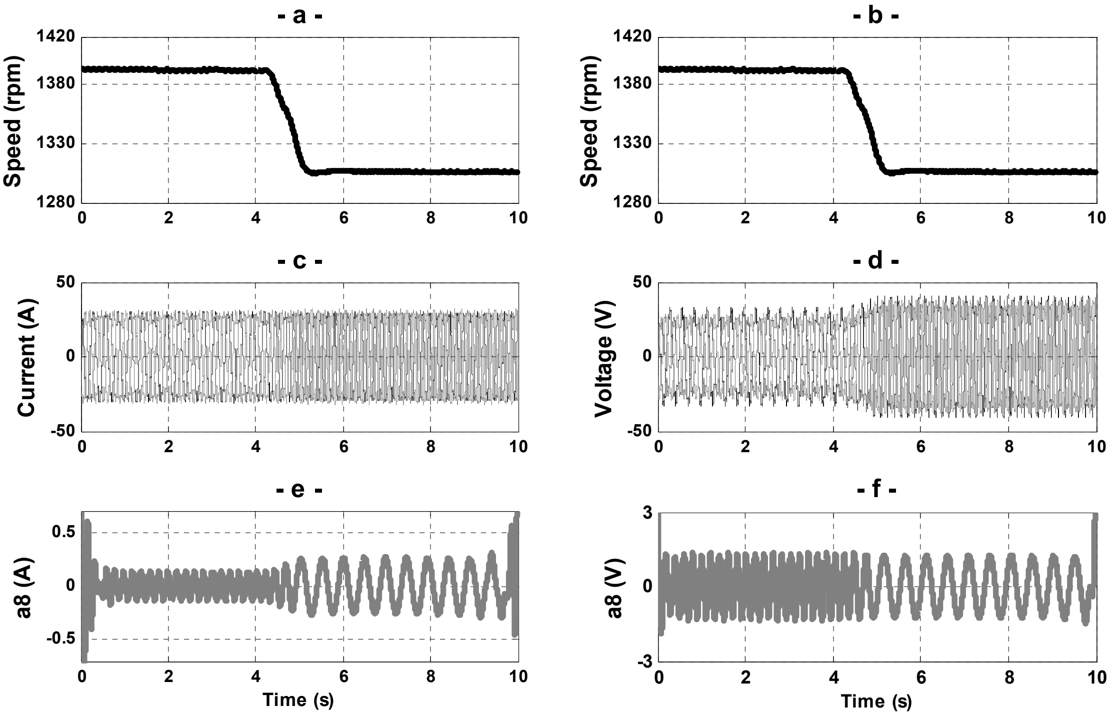

Fig. 3. 10 DWT of the signals I_{sl}^{krr} and V_{sl}^{krr} in faulty condition ($R_{add}=R_r$) under speed transient (experimental results)

3.3.2.1 Stator progressive dissymmetry detection

The stator resistance has been linearly varied in simulation from $R_{add}=0$ to $R_{add}=1.3R_s$. At rated speed, the value of f_{sli}^{krs} used for the computation of $V_{sl}^{sr}(t)$ is -99.79 Hz. The simulation result of Fig. 3.11 has been confirmed by experimental tests in the same conditions (Fig. 3.12). During the first time interval (from $t=0s$ to $t \approx 2s$) under healthy condition, the three-phase rotor voltages are balanced and sinusoidal. For this time interval, the 8th approximation signal, representative of the stator fault component at the frequency *(s-2)f*, does not show any variation. During the ramp variation of the stator resistance emulating the winding fault, the rotor phase voltages are balanced, although progressive distortions appear, which indicate the increasing contribution of the fault component at frequency *(s-2)f*. As can be seen, the progressive stator unbalance is visible in the approximation signal a_8, showing a proportional increase of its magnitude. Hence, the trend of the approximation signal is related to the fault component evolution at frequency *(s-2)f*. The experimental tests corroborate the simulation result and prove the effectiveness of the proposed technique.

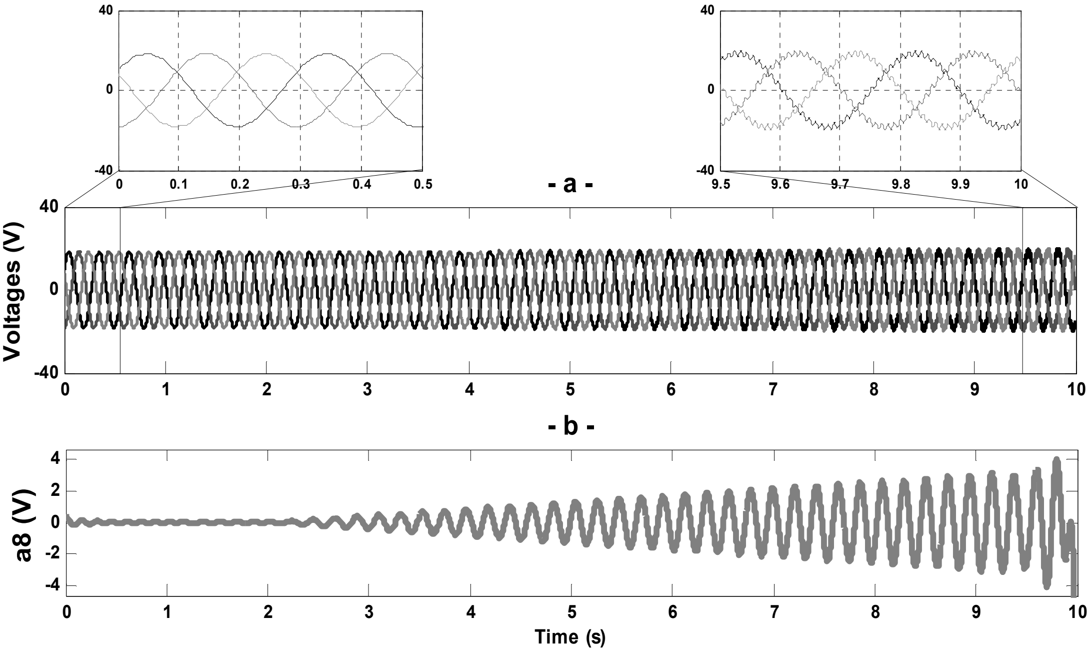

Fig. 3. 11 Discrete WT of V_{sl}^{krs} under progressive stator unbalance condition (simulation results)

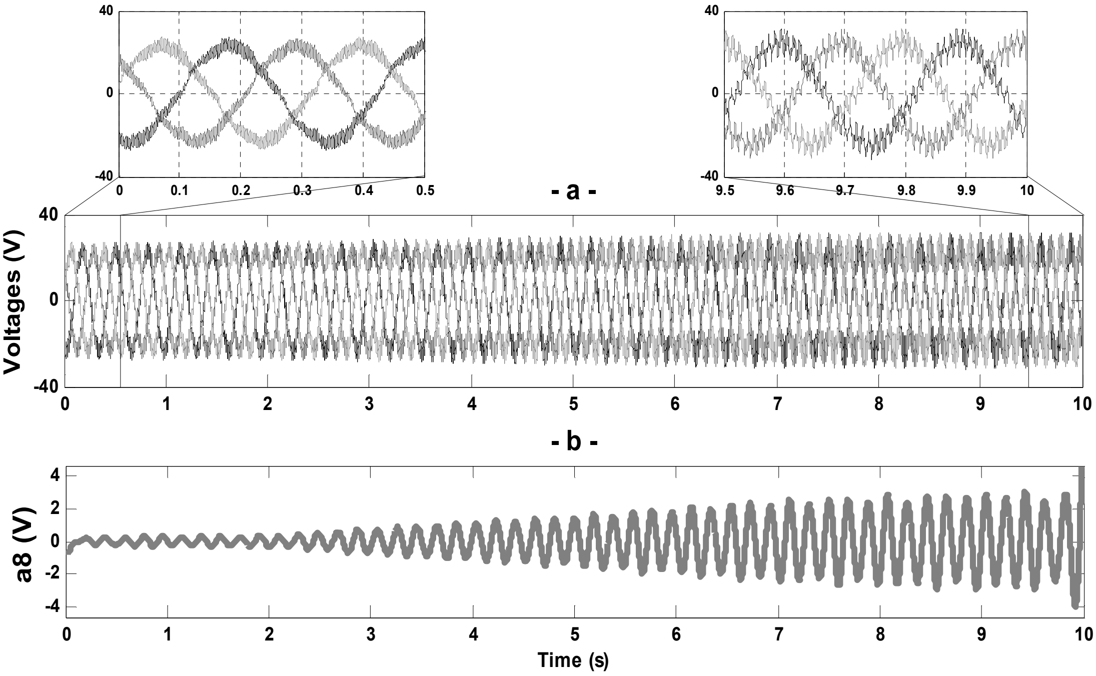

Fig. 3. 12 Discrete WT of V_{sl}^{krs} under progressive stator unbalance condition (experimental results)

3.3.2.2 Rotor progressive dissymmetry detection

The rotor resistance has been progressively varied in simulation from $R_{add}=0$ to $R_{add}=1.3R_r$. At rated speed, the value of f_{sli}^{krr} to compute $V_{sl}^{rs}(t)$ is -6.45 Hz. The simulation result (Fig. 3.13) has been confirmed by experimental tests in the same conditions (Fig. 3.14). As it can be seen, in healthy condition (from $t=0s$ to $t \approx 2s$) the three-phase rotor voltages are quite balanced and sinusoidal. The corresponding approximation signal a_8 does not show any particular oscillation during the two first seconds. When the rotor fault occurs, the three-phase rotor voltages are almost sinusoidal but become progressively unbalanced as long as the contribution of the fault frequency component $-sf$ increases. This is clearly reflected by the progressive distortion of the approximation a_8, allowing to diagnose the rotor windings degradation. In conclusion, the experimental results are in complete agreement with the simulations.

3.4 Fault quantification

Once the state of the machine has been diagnosed, a quantitative evaluation of the fault degree is necessary. The fault indicator is periodically calculated over time, every δn sampling period, and over a time interval including the latter Δn samples. This process is illustrated by Fig. 2.11.

During the experimental tests, the time interval between two consecutive calculations of the fault indicator was 125 ms, and the length of the time window for the calculation of the fault indicator was 2000 ms. Since the sample frequency was 3200 Hz, the number of samples between two consecutive calculations of the fault indicator was $\delta n = 125\ 10^{-3} \cdot 3200 = 400$, and the length of the sequence of samples was $\Delta n = 2000\ 10^{-3} \cdot 3200 = 6400$. The values of δn and Δn were chosen according to the desired time sensitivity to observe the fault evolution.

When the fault occurs, the signal energy distribution changes due to the presence of the fault frequency component. Hence, the energy excess confined in the approximation signal may be considered as a fault indicator in case of stator or rotor unbalances.

The trends of the fault indicators $mPa_8(I)$ and $mPa_8(V)$ corresponding to the simulation results depicted in Figs. 3.3 and 3.4 were computed under healthy and faulty conditions and are shown in Fig. 3.15. In healthy conditions ($R_{add}=0$), and under large range of speed variations, $mPa_8(I)$ and $mPa_8(V)$ are practically constant. Consequently, the indicator values for the healthy WRIM can be assumed as a baseline to set the threshold to discriminate healthy from stator unbalance conditions.

Under faulty condition ($R_{add}=R_s$), $mPa_8(I)$ does not show any significant variation. As previously discussed, this is due to the compensating effect of the control system. However, $mPa_8(V)$ shows a significant increase. The large energy deviation observed in faulty condition proves the effectiveness of the proposed approach, since the WRIM speed transient does not affect the indicator accuracy. The trend of the fault indicators shown in Fig. 3.16, and corresponding to the wavelet analysis shown in Figs. 3.5 and 3.6, confirms the behavior of the computer simulations.

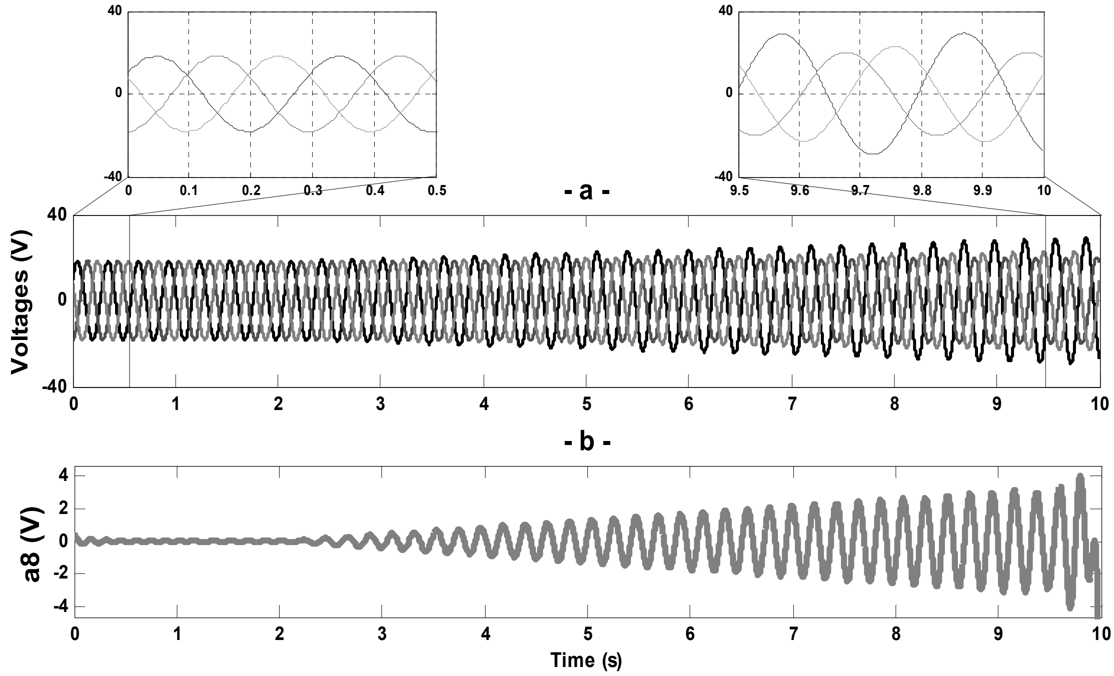

Fig. 3. 13 Discrete WT of V_{sl}^{krr} under progressive rotor unbalance condition (simulation results)

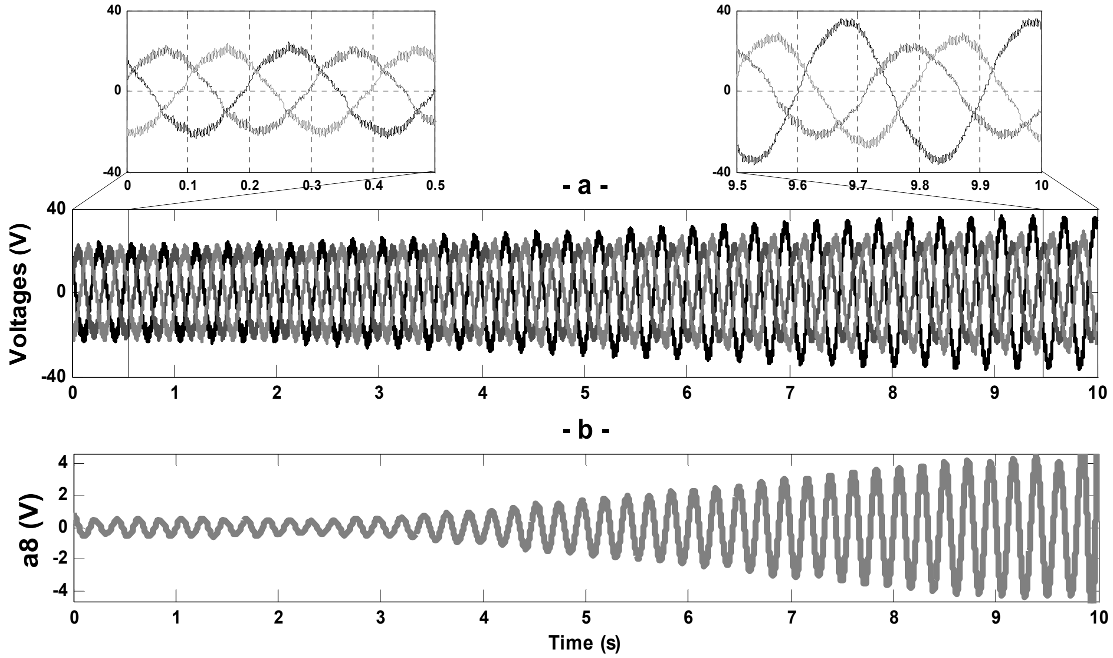

Fig. 3. 14 Discrete WT of V_{sl}^{krr} under progressive rotor unbalance condition (experimental results)

Figs. 3.17 and 3.18 show the trend of the fault indicators *$mPa_8(V)$* and *$mPa_8(I)$* during the same large speed transients analyzed in Figs. 3.7-3.10. According to the qualitative analysis in Section V-B, *$mPa_8(V)$* is expected to show variations that are more remarkable than the ones of *$mPa_8(I)$*, and the experimental results confirm this forecast. At the same time, *$mPa_8(V)$* turns out to be less sensitive to speed variations than *mPa_8* (*I*).

The trend of the fault indicator *$mPa_8(V)$* applied to $V_{sl}^{rs}(t)$ under progressive stator unbalance is shown in Fig. 3.19-a. When the stator asymmetry occurs progressively, the fault indicator clearly shows the fault evolution. In the same way, under a progressive rotor unbalance (Fig. 3.19-b), the fault indicator related to $V_{sl}^{rr}(t)$ shows a trend proportional to the fault severity.

The discrepancy observed in Fig. 3.19 between simulation and experimental results is mainly due to the inherent motor asymmetry and to measurements errors that are not considered in the analytical model. However, once the proposed technique is implemented, there is no need to know the effect of the above non idealities. In fact, a diagnosis criterion for the proposed technique typically consists in checking if the fault indicator exceeds a threshold value, which is chosen experimentally according to the accuracy of the measurements, the desired sensitivity and the behavior of the healthy machine.

In addition, the proposed fault indicator could be used also to build more complex diagnosis criteria. For example, datasets built by means of the proposed fault indicator may be used to train clustering or fuzzy techniques, neural networks or others AI methods.

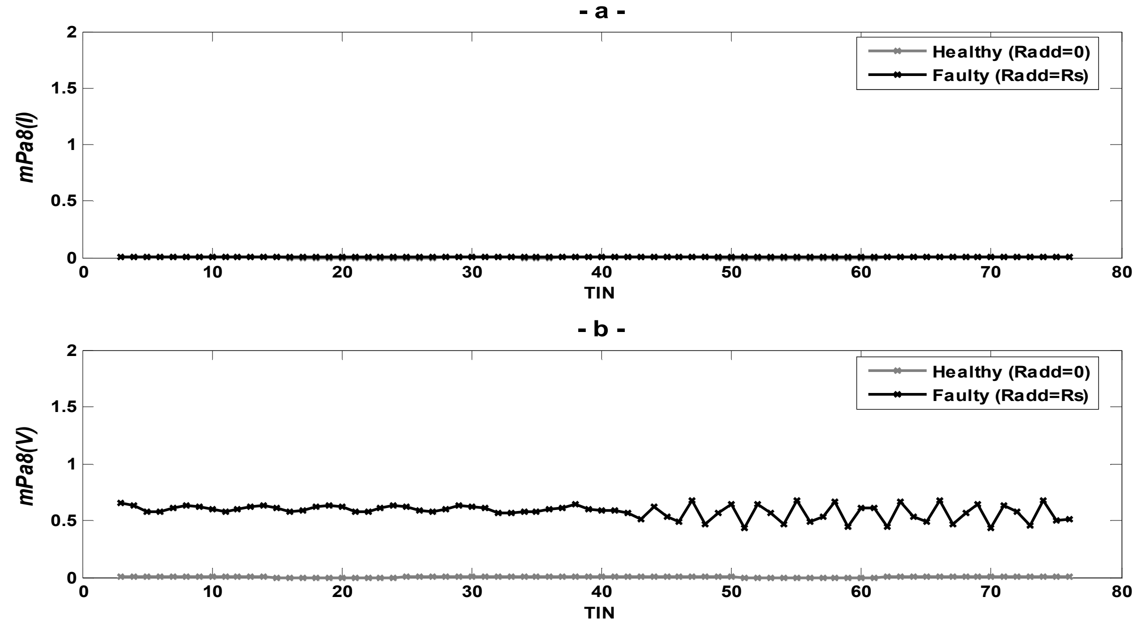

Fig. 3. 15 Values of the fault indicator *mPa_8* (as a function of the Time Interval Number) resulting from the 8th wavelet decomposition under stator unbalance for large speed variation (simulation results): a) $I_{sl}^{rs}(t)$ - b) $V_{sl}^{rs}(t)$

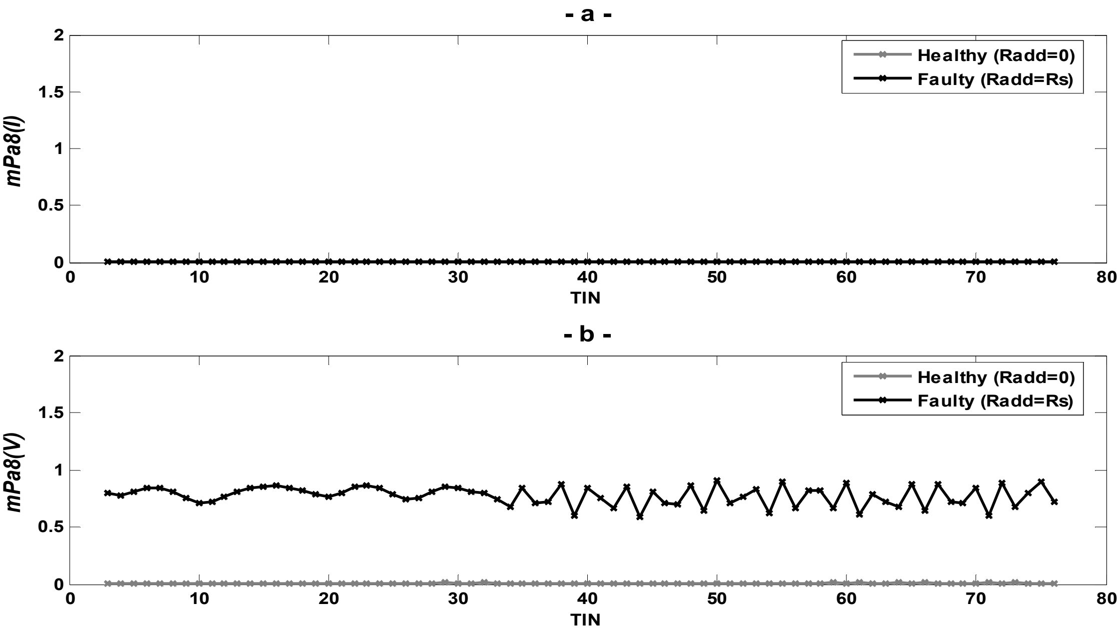

Fig. 3. 16 Values of the fault indicator mPa_8 (as a function of the Time Interval Number) resulting from the 8th wavelet decomposition under stator unbalance for large speed variation (experimental results): a) $I_{sl}^{rs}(t)$ - b) $V_{sl}^{rs}(t)$

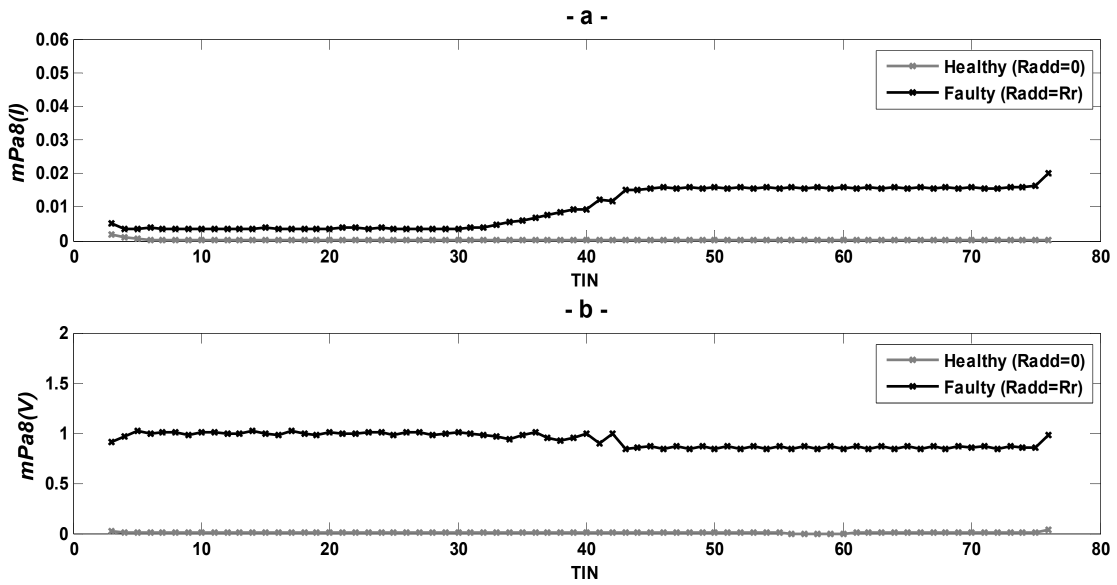

Fig. 3. 17 Values of the fault indicator mPa_8 (as a function of the Time Interval Number) resulting from the 8th wavelet decomposition under rotor unbalance for large speed variation (simulation results): a) $I_{sl}^{rr}(t)$ - b) $V_{sl}^{rr}(t)$

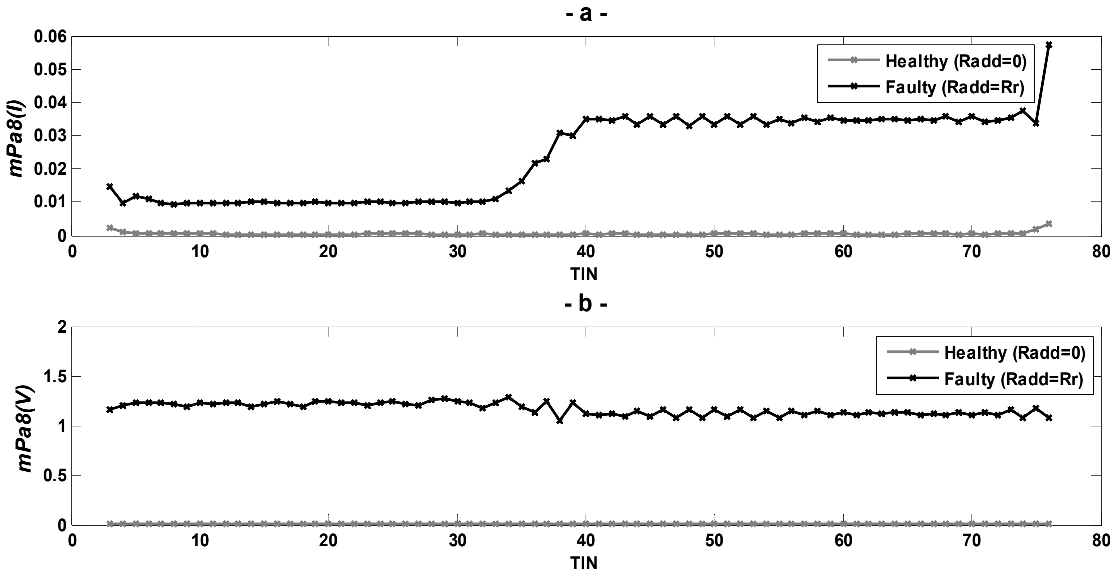

Fig. 3. 18 Values of the fault indicator *mPa_8* (as a function of the Time Interval Number) resulting from the 8th wavelet decomposition under rotor unbalance for large speed variation (experimental results): a) $I_{sl}^{rr}(t)$ - b) $V_{sl}^{rr}(t)$

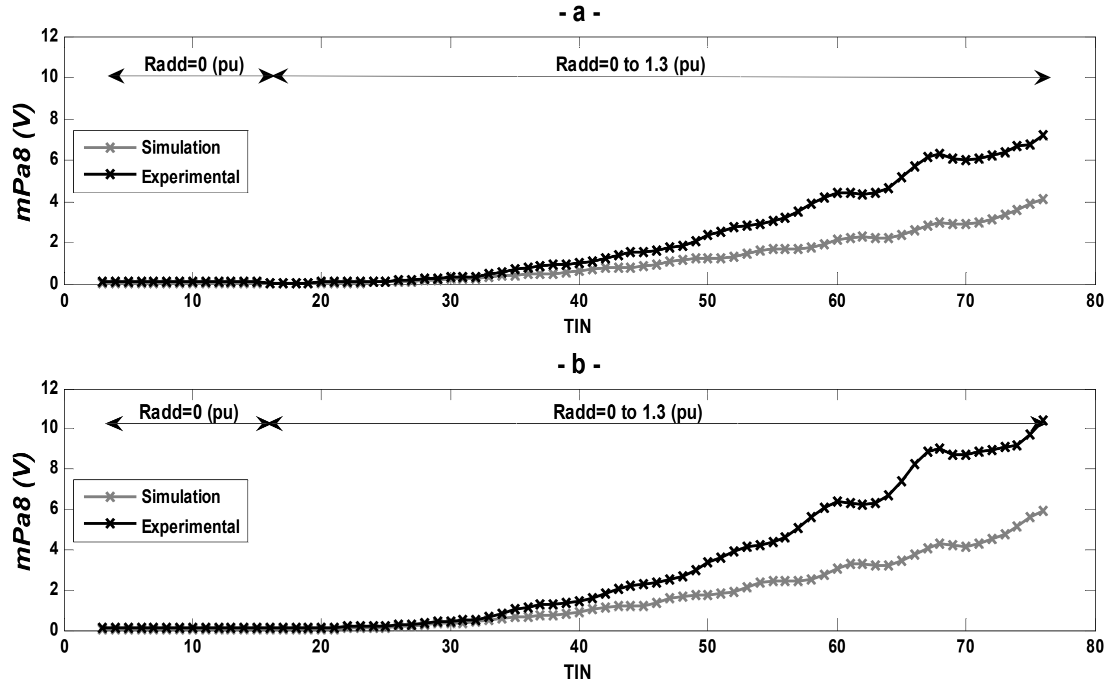

Fig. 3. 19 Values of the fault indicator *mPa_8* resulting from the 8th wavelet decomposition of $V_{sl}^{rs}(t)$ and $V_{sl}^{rr}(t)$ under progressive winding fault: a) stator -b) rotor

3.5 Conclusion

In this chapter, the proposed diagnosis technique presented in Chapter 2 was validated for the detection of electrical faults in three-phase wound-rotor induction machines (WRIMs). In this application, the proposed diagnosis approach was applied for processing the rotor-voltage commands, thus the time evolution of fault components were efficiently tracked under time-varying conditions:

- Speed-varying conditions ;
- Fault-varying conditions.

Moreover, the relevance of the fault components computed from rotor voltages in comparison to those coming from rotor currents under closed-loop operation was evidenced under time-varying conditions.

Results issued from the quantitative evaluation process of the fault extend issued from the wavelet analysis were presented showing accurate stator- or rotor-fault detection under time-varying conditions.

Simulation and experimental results show the validity of the proposed method, leading to an effective diagnosis procedure for both stator and rotor electrical faults in WRIMs.

REFERENCES

[1] A. Tapia, G. Tapia, J. X. Ostolaza, and J. R. Saenz, “Modeling and control of a wind turbine driven doubly fed induction generator”, *IEEE Trans. on Energy Conversion*, vol. 18, n° 2, June 2003, pp. 194-204.

[2] E. Bogalecka and Z. Kzreminski, “Control system of a doubly-fed induction machine supplied by current controlled voltage source inverter,” *in Proc. Inst. Elec. Eng. of Sixth Int. Conf. on Electrical Machines and Drives*, London, U.K., 1993.

[3] A. Stefani, A. Yazidi, C. Rossi, F. Filippetti, D. Casadei and G.A. Capolino, "Doubly Fed Induction Machines Diagnosis Based on Signature Analysis of Rotor Modulating Signals", *IEEE Transactions on Industry Application*, Vol. 44, N° 6, Nov/Dec 2008.

[4] A. Yazidi, H. Henao, G. A. Capolino, D. Casadei, and F. Filippetti, “Double-fed three-phase induction machine abc model for simulation and control purposes,” *in Proc. 24th Annu. IEEE IECON*, Raleigh, NC, Nov. 6–10, 2005, pp. 2560–2565.

[5] D. Casadei, F. Filippetti, C. Rossi, A. Stefani "Closed Loop Bandwidth Impact on Doubly Fed Induction Machine Asymmetries Detection Based on Rotor Voltage Signature Analysis", *43rd International Universities Power Engineering Conference*, UPEC 2008.

CHAPTER 4 : ANALYSIS OF ROTOR FAULTS SQUIRREL CAGE INDUCTION MACHINES

4.1 Introduction

In this chapter, the proposed diagnosis technique is validated for the detection of rotor broken bars in squirrel cage induction motors. The diagnosis of rotor faults in induction machine is commonly carried out by means of Motor Current Signature Analysis (MCSA), i.e., by classical spectrum analysis of the input currents. However MCSA has some drawbacks that are still under investigation. The main concern is that an efficient frequency transformation cannot be made for induction machines operating in speed–varying condition, since slip and speed vary and so does the sideband frequencies.

Another important issue related to double squirrel cage induction motors (DCIMs), subject to higher misdetection of outer cage damage in time-varying load applications, such as conveyor belts, pulverizers, etc., for which DCIMs are frequently employed. This is because the magnitude of the rotor fault frequency components (RFFCs) in the current spectrum of faulty DCIMs are small due to the low magnitude current circulation in the outer cage under steady state operation. In case of load variation, the small RFFCs are spread in a bandwidth proportional to the speed variation, which makes them even more difficult to detect.

In this chapter, the proposed diagnosis technique is firstly applied for rotor broken bars detection for single cage induction machine, by investigating MCSA. The second part of this chapter is focused on the detection of rotor outer cage bar faults for double cage motors. An experimental study on a custom-built fabricated *Cu* double cage rotor induction motor shows that the proposed diagnosis technique can provide improved detection of outer cage faults particularly used in time-varying load applications.

Experimental results show the validity of the developed approach, leading to an effective diagnosis method for broken bars in induction machines.

4.2 Analysis of rotor fault in single cage induction machine

4.2.1 System description

In order to validate the results obtained in simulations a test bed was realized. A 7.5 kW, 2 poles pair induction machine was used (Table. 4.1). Two rotors are available, one healthy and one with a drilled rotor bar. The induction machine is coupled to a 9kW separately excited DC machine controlled in speed. This allows to reproduce the simulated speed transients. Photos of the experimental test bed are shown in Fig. 4.1.

Machine currents and speed are sampled at 3.2 kHz with a time duration of 10 seconds. A smaller number of points could be used without affecting the performances of the proposed procedure.

Table. 4. 1 Single Cage Induction Motor parameters

Parameter	*Unit*	*Value*
Rated power	kW	7.5
Rated stator voltage	V	380
Nominal stator current	A	15.3
Rated frequency	Hz	50
Rated speed	rpm	1440
Stator phase resistance	Ω	0.54
Rotor phase resistance	Ω	0.58
Stator inductance	mH	88.4
Rotor inductance	mH	83.3
Magnetizing inductance	mH	81.7
Pole pairs		2
Number of rotor bars		28

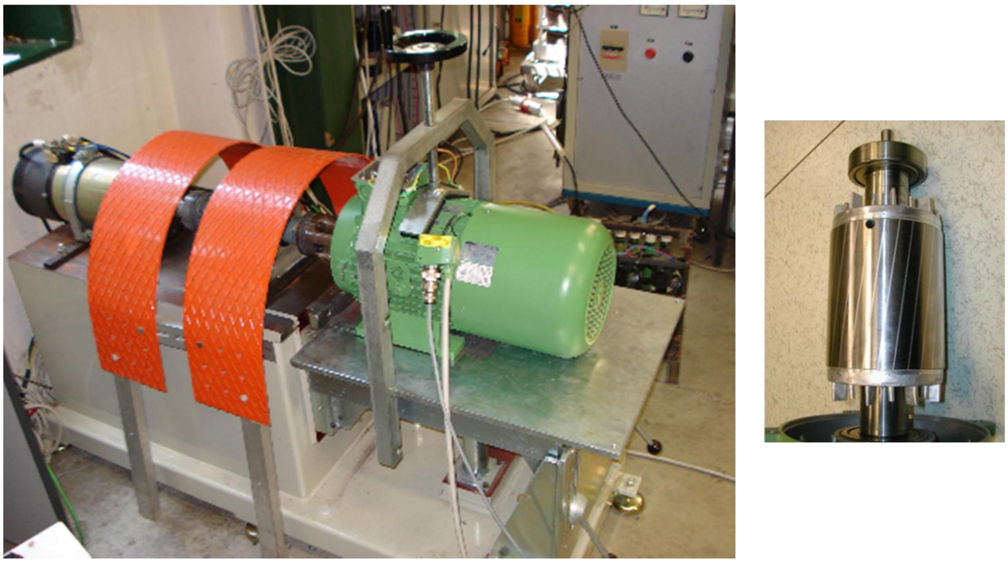

Fig. 4. 1 Test bed photo (left). The faulty rotor with one drilled rotor bar (right)

4.2.2 Results

4.2.2.1 Fault detection under speed-varying conditions

The induction motor has been initially tested in healthy conditions during a prefixed transient from 1496 rpm to 1460 rpm, corresponding to slip ranges from s=0.002 to s=0.026. Another test, for the same speed transient was made with the machine operating with one rotor broken bar. The instantaneous values of speed and phase currents, corresponding to the healthy and faulty cases, are depicted in Fig. 4.2 (a-b) and

Fig. 4.2 (c-d) respectively. For the considered speed range, approximation a_9 was chosen for extracting the contribution of the fault components $(1-2s)f$ and $(1+2s)f$.Therefore the choice of f_{sl} is made to shift these fault components inside the frequency interval [0, 3.125] Hz corresponding to approximation. For the sake of clarity only the a_9 signal will be reported. In healthy condition, the 9th approximation signal a_9, resulting from the wavelet decomposition of the stator phase current, does not show any kind of variation (Fig. 4.3). This indicates the absence of the fault component $(1-2s)f$, leading to diagnose the healthy condition of the motor under speed-varying condition.

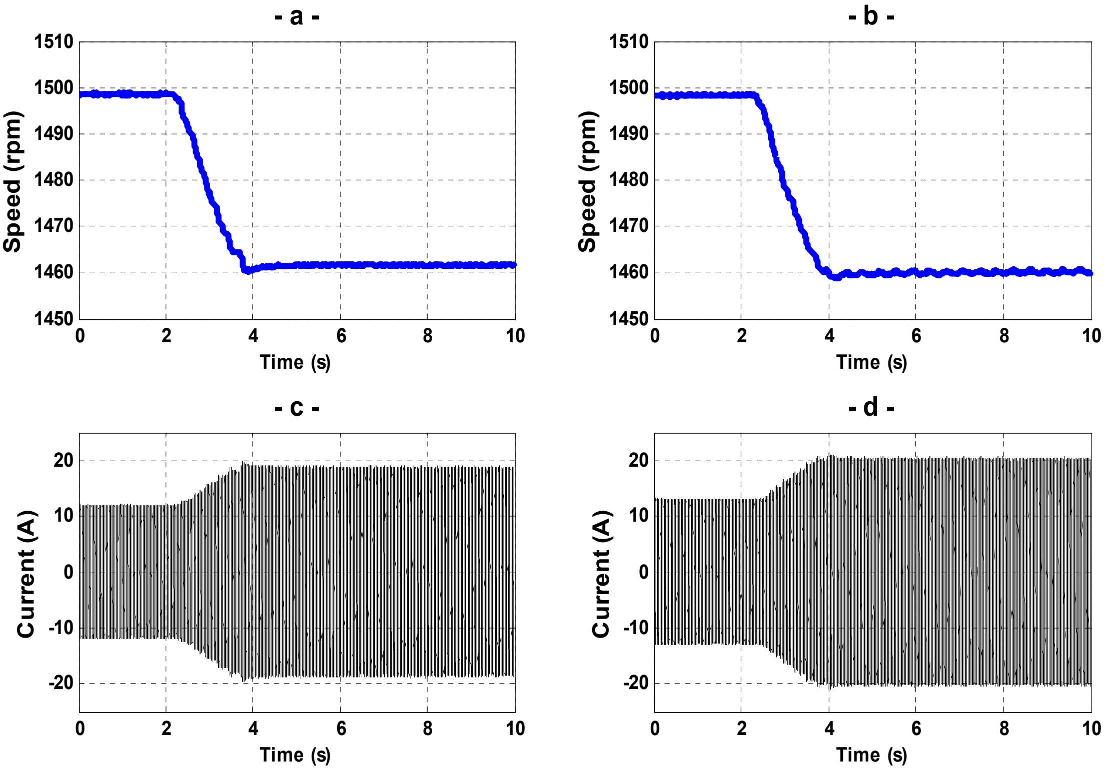

Fig. 4. 2 Instantaneous values of a-b) speed and c-d) stator phase currents under healthy and one rotor broken bar respectively

However, in faulty condition (one rotor broken bar) approximation a_9 shows significant variation in magnitude observed in Fig. 4.4. During the first time period (t=0s to t=2s), under a constant speed of 1496 rpm, the 9th approximation signal, representative of the $(1-2s)f$ frequency component, do not show any important variations. This is due to the fact that at low load level (under 4% of the nominal torque) the fault frequencies are practically superimposed to the fundamental and magnitudes are not detectable. During deceleration (around t=2s), a_9 shows particular magnitude escalation proportional to the abrupt deceleration until reaching a quasi steady-state magnitude (under 66% of the nominal torque).

More in detail, the oscillations observed in the signal a_9, with quasi-constant amplitude, follow a characteristic pattern that fits the evolution in frequency of the fault component *(1-2s)f*, during the speed transient.

The second rotor fault signature tracked is related to the fault component at frequency *(1+2s)f*. The corresponding experimental results, under healthy and rotor broken bar are presented in Fig. 4.5 and Fig. 4.6. The same observations as for the signature of the side band *(1-2s)f* under the considered rotor unbalance, are reached; the comparison of the approximation signal a_9, issued from wavelet decomposition of the stator phase current, under healthy (Fig. 4.5-b) and rotor broken bar (Fig. 4.6-b) reproduce clearly the magnitude evolution of the fault component *(1+2s)f* dynamically over time.

If we confine our attention on the approximation signal a_9 depicted in Fig. 4.4-b and Fig. 4.6-b, we can notice that the rotor fault signature issued from the fault component *(1-2s)f* is more relevant than the corresponding one related to the *(1+2s)f* component. This is mainly due to the the machine-load inertia effect on high order rotor fault harmonics. The 9th approximation signal obtained from the experimental results shows the sensitivity and the effectiveness of this particular signal a_9 to reproduce the contribution of the frequency components *(1-2s)f* and *(1+2s)f* under large speed varying conditions.

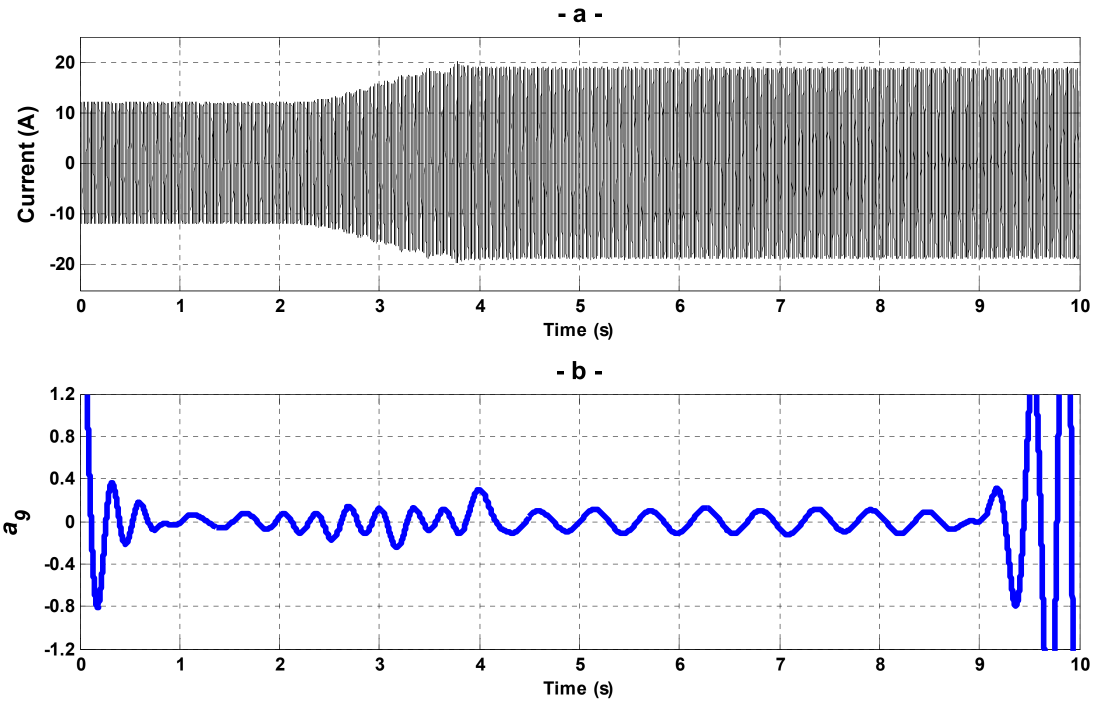

Fig. 4. 3 DWT analysis of stator phase current under speed-varying condition, for tracking the fault component *(1-2s)f* ; Healthy condition

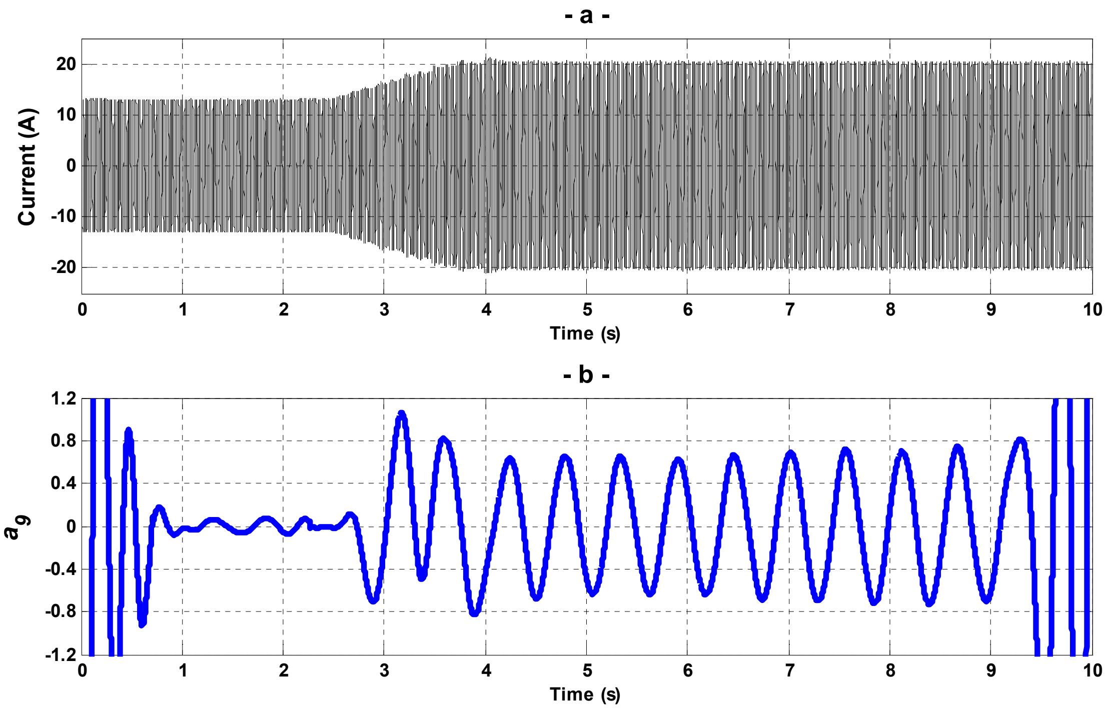

Fig. 4. 4 DWT analysis of stator phase current under speed-varying condition, for tracking the fault component *(1-2s)f* ; One Broken Bar

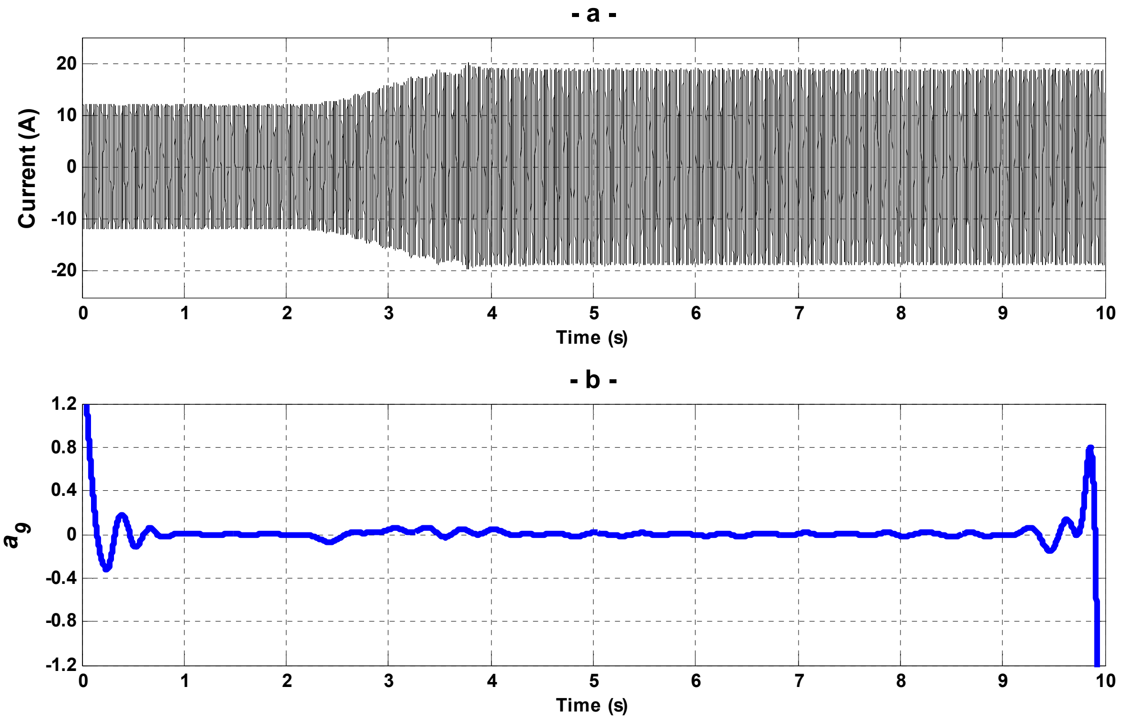

Fig. 4. 5 DWT analysis of stator phase current under speed-varying condition, for tracking the fault component *(1+2s)f* ; Healthy condition

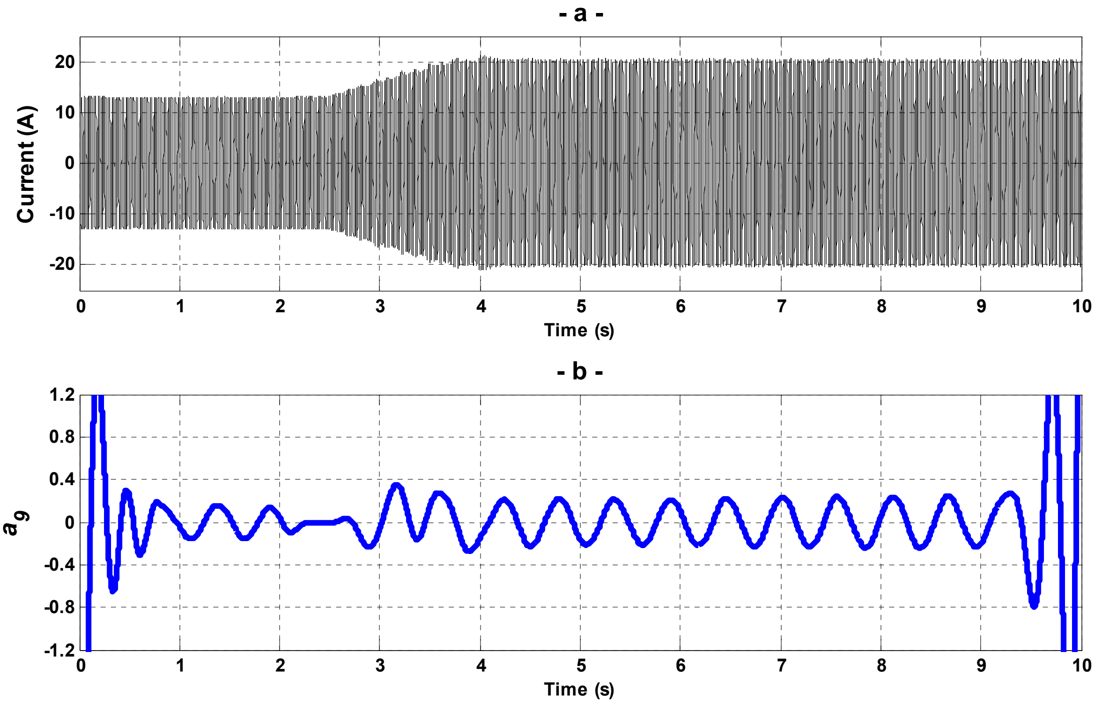

Fig. 4. 6 DWT analysis of stator phase current under speed-varying condition, for tracking the fault component *(1+2s)f* ; One Broken Bar

4.2.2.2 Fault quantification

Once the machine is qualitatively diagnosed, the fault indicator based on a cyclic mean power calculation of the approximation a_9, resulting from the wavelet decomposition applied to one stator current, has been processed to evaluate quantitatively the degree of the fault extent.

The cyclic evolution of the fault indicator mPa_9, representative of the contributions of the fault components components *(1-2s)f* and *(1+2s)f* , issued from the experimental tests (Figs. 4.3-4.6), under healthy and rotor broken bar conditions are depicted in Fig. 4.7 and Fig. 4.8 respectively. In healthy condition, and under large range of speed variations, mPa_9 does not show any significant change. Consequently, the indicator values for the healthy motor are considered as a baseline to set the threshold for discriminating healthy from faulty conditions. Under rotor broken bar condition the calculated mPa_9 indicator shows a noteworthy increase. The large energy deviation observed in faulty condition proves the effectiveness of the proposed approach, since the transient speed motor operation does not disturb the fault assessment, in comparison with the healthy case.

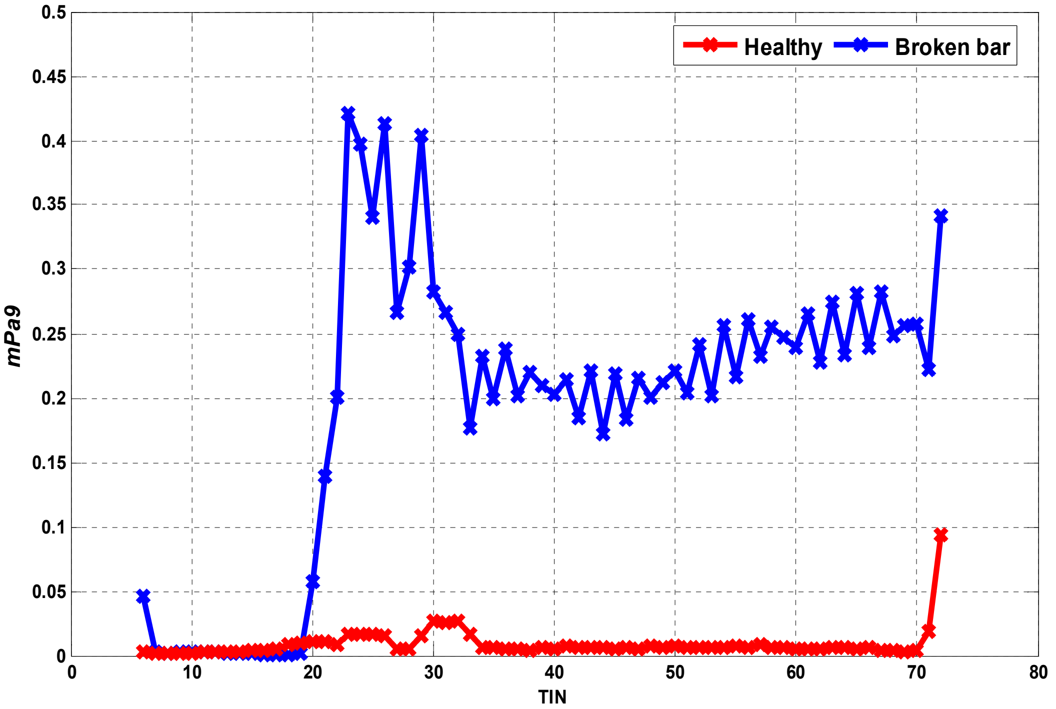

Fig. 4. 7 Cyclic values of the fault indicator *mPa*$_9$, resulting from the 9th wavelet decomposition level of the signals I_{sl} under healthy and rotor bar broken (red and blue) during the tracking of *(1-2s)f* component

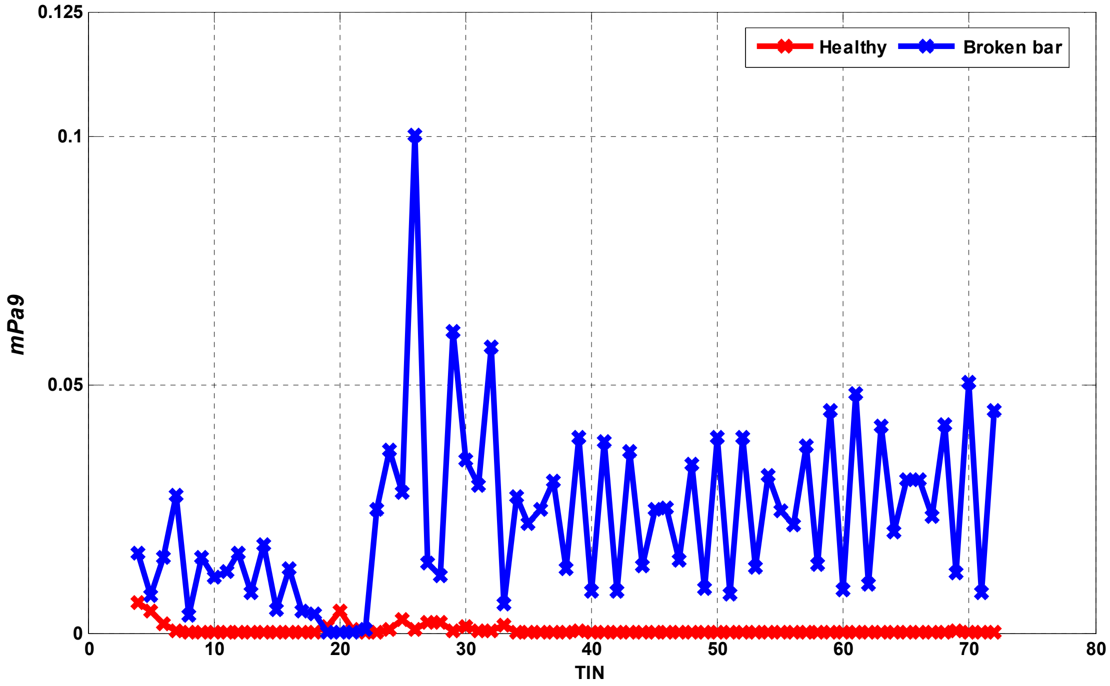

Fig. 4. 8 Cyclic values of the fault indicator *mPa*$_9$, resulting from the 9th wavelet decomposition level of the signals I_{sl} under healthy and rotor bar broken (red and blue) during the tracking of *(1+2s)f* component

4.3 Analysis of rotor fault in double cage induction machine

Successful detection of outer cage faults in DCIMs requires understanding similarities and differences with single cage broken bars phenomenon. The main similarity between these two classes of motors in case of rotor fault is the existence of interbar currents [1]-[5], and the chain of fault harmonics that appears in stator line-currents [6]-[8].

For large or double squirrel cage motors, as long as the contact impedance between the rotor bars and iron core is small or the copper bars are directly inserted into the laminated iron slots, the broken bars are no longer a physical condition ensuring an open circuit, since inter-bar or cross path currents can flow. If the resistance between the bars and the iron core is low, currents will start to flow between the bars through the lamination, which increases the stray-load losses in the machine and affect the torque during the start-up [3]-[4]. Subsequently, these currents interact with the radial component of the air-gap magnetic field, and compensate the rotor asymmetry caused by rotor bar breakage and leads to axial vibrations [1],[4] and to temperature increase [9]. In DCIMs these interactions can reduce significantly the amplitudes of rotor fault components.

Another typical behavior of induction motors with rotor broken bars is the existence of sideband components in the line currents at frequencies $(1\pm 2s)f$ whose amplitudes are usually monitored for rotor diagnostic. The main difference between DCIMs and single cage motors in case of broken bars is related to the inherent structure of the double cages [10]. Double cage motors have two squirrel cages shorted with a common end ring or with separate end rings. The schematic and the electrical equivalent circuit of the double cage rotor are shown in Fig. 4.9. The outer cage is usually composed of small high resistivity material bars, while the inner cage is made of larger, low-resistance bars [11]. The iron between the outer cage and the inner cage, together with the proximity of the outer cage with the stator windings, causes the outer cage leakage reactance to be low. Conversely, the leakage inductance of the inner cage is large since the magnetic reluctance of flux path closing through the inner bar is low (Fig. 4.9).

Therefore, the rotor current is mainly confined to the high resistance outer cage at high slip (i.e., startup) due to the dominance of the leakage inductance, thus obtaining high startup torque. When steady state operation is reached, the leakage inductance is negligible (low slip) and the outer cage resistance is dominant, which causes the current to flow mainly in the low resistance inner cage. The rotor operates as a normal low-resistance rotor, and the sensitivity of detecting the rotor fault from stator current is significantly reduced. Considering that the depth of flux penetration into the rotor is inversely proportional to the square root of the rotor frequency, the inner cage can be nearly disregarded during the startup or during any abrupt slip increase due to load transients.

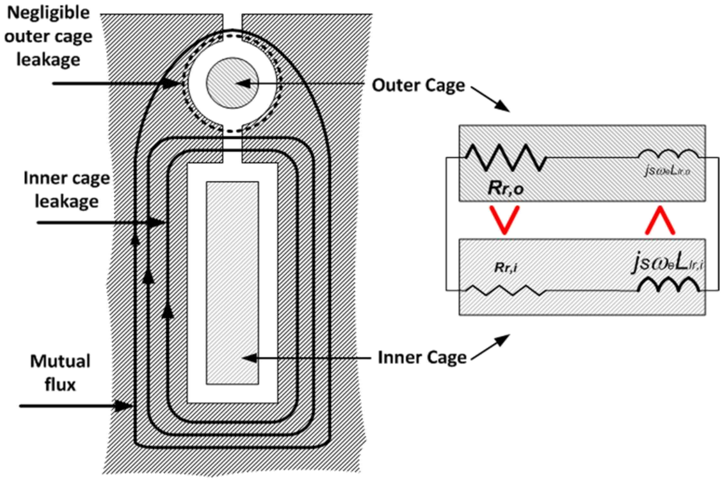

Fig. 4. 9 Electrical equivalent circuit representation of a double squirrel cage induction motor

The sensitivity of MCSA has been experimentally evaluated in [7], [12] for single cage and double cage rotor machines. It can be seen in Fig. 4.10 that the sensitivity of MCSA for outer cage damage in double cage rotors under rated load is significantly lower than that of the single cage rotor under identical conditions. The f_l component is relatively lower by 18 ~ 22dB for the double cage design, which corresponds to a decrease in sensitivity by a factor of 10. The situation is worse for time-varying loads since the fault components spread out resulting in lower peak magnitude. Considering that the default fault alarm level for broken bars is set at -45~-35dB in commercial MCSA products (to avoid false alarms) [12]-[13], outer cage faults of double cage motors are unlikely to be detected unless a method dedicated to double cage motors is used.

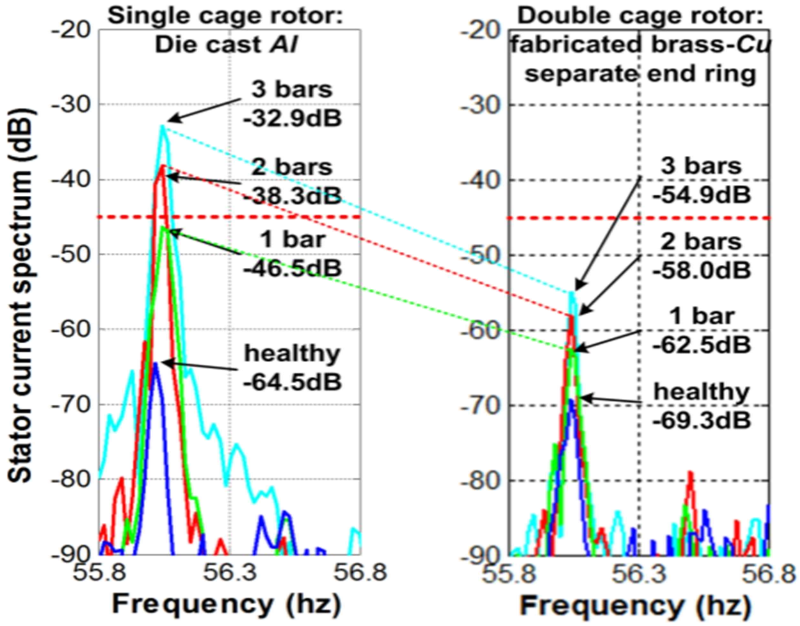

Fig. 4. 10 Experimental measurements of broken bar component, f_{rffc}, with on-line MCSA under rated load for 0-3/44 broken bars for (left) single cage deep bar *Al* die cast rotor; (right) double cage fabricated brass-*Cu* separate end ring rotor [7]

4.3.1 Motor Current Signature Analysis

4.3.1.1 System description

Experimental verification of the proposed method was performed on a 380V, 7.5 Hp, 12 A induction motor with a custom-made double cage rotor. A fabricated copper separate end ring double cage rotor, shown in Fig. 4.11, was constructed to fit the stator of an aluminum die cast induction motor, already available. The outer cage was made of brass, which is common in large motors for obtaining high starting torque. The custom-made rotor is designed and built so that it allows testing of the proposed method on a motor representative of large motors.

The tests were performed for the healthy rotor and a faulty rotor after cutting 3 of 44 rotor bars at the bar end ring joint. The MCSA results shown for the double cage rotor in Fig. 4.10 are obtained with the same test rotor. The motor load was controlled by adjusting the field voltage of a 30 Hp DC generator coupled to the motor. Commercial current sensors and a 16 bit DAQ board were used to measure the stator-line current i_{sa} (the sampling frequency f_s was 960 Hz) over a data acquisition window of 10 seconds under load transient conditions from 10% to 90% of the full load. The second series of tests was carried out during an acquisition time interval of 25 seconds under a load profile from 10% to 50% then to 90% of the full load.

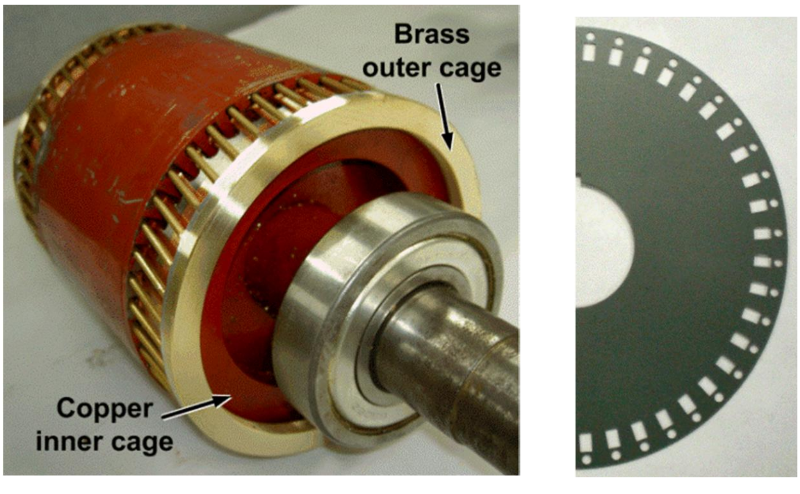

(a) (b)

Fig. 4. 11 Custom designed fabricated copper separate end ring double cage rotor sample with brass outer cage and copper inner cage(a), and the corresponding rotor lamination (b)

4.3.1.2 Results

4.3.1.2.1 Rotor Fault detection

A six level decomposition (*n=6*) was chosen to cover the frequency bands of the fault components, as shown in Table 4.2. The proposed diagnosis approach was applied to the stator current with f_{sl}^{l}=52.10 Hz and then with f_{sl}^{r}=60.39 Hz, to isolate the contribution of the fault components f_l and f_r, respectively. The first series of tests were conducted under a large speed transient during 10 seconds, as reported by the speed profiles in Figs. 4.12-a and 4.13-a, for healthy rotor and for three rotor outer cage broken bars, respectively. The corresponding stator currents are shown in Figs. 4.12-b and 4.13-b. The sixth-level approximation signals resulting from the DWT of $i_{sl}^{l}(t)$ in healthy and faulty conditions, computed under the assumption of a sliding frequency f_{sl}^{l}=52.10Hz, are depicted in Figs. 4.12-c and 4.13-c respectively.

Table. 4. 2 Frequency bands of approximation and detail signals

Approximation signal, a_j	*Frequency bands (Hz)*	*Detail Signal, d_j*	*Frequency bands (Hz)*
a_6	[0 – 7.5]	d_6	[7.5 – 15]
a_5	[0 – 15]	d_5	[15 – 30]
a_4	[0 – 30]	d_4	[30 – 60]

In healthy condition, it can be observed that the approximation signal a_6 (Fig. 4.12-c) does not show any variation. This fact indicates that the fault component f_l is absent in the stator current (Fig. 4.12-b), which leads to the diagnosis of “healthy” condition of the DCIM.

On the contrary, a significant variation in the amplitude of the approximation signal a_6 can be observed under a fault condition with three broken outer cage bars, as shown in Fig. 4.13-c. In steady state, under light load conditions (10% rated load), important variations in a_6^l cannot be observed between 0~4 *s*. This is due to the fact that fault components with small magnitude, superimposed on the fundamental, are not detectable under light load conditions. However, during the deceleration transient due to the load variation around *t*≈4s, an escalation in the magnitude of a_6^l proportional to the rate of deceleration can be observed, as shown in Fig. 4.13-c.

The increase in the 6th approximation signal can be observed until reaching a quasi steady-state magnitude at 90% rated load. The oscillations observed in the signal a_6^l with quasi-constant amplitude are the consequence of the time evolution of the component f_l issued from the stator current (Fig. 4.13-b) during the speed transient.

The second rotor fault signature tracked is related to the right sideband component at frequency f_r.

The corresponding experimental results, under healthy and three broken outer cage bars are presented in Figs. 4.12-d and 4.13-d, respectively.

The observations for a_6^r are similar to those of a_6^l. The variation of the 6th approximation signal is negligible under healthy (Fig.4.12-d) condition, whereas a remarkable evolution over time can be observed for the faulty case (Fig. 4.13-d). Analyzing the approximation signals a_6^l and a_6^r depicted in Figs. 4.13-c,d, one can note that the rotor fault signature issued from the fault component related to f_l shows larger variation than that related to f_r. This is due mainly to the damping effect of the machine-load inertia. In any case, for reliable diagnosis, the diagnostic index is based on the sum of both amplitudes.

In order to determine the threshold for the fault indicator F_{ind}, a second series of experimental tests were conducted under healthy and faulty cases, with the time varying load (speed) profile shown in Figs. 4.14 and 4.15. The load was increased from 10% to 50% and then to 90% within a 25*s* interval. The results are similar to those Figs. 4.12 and 4.13.

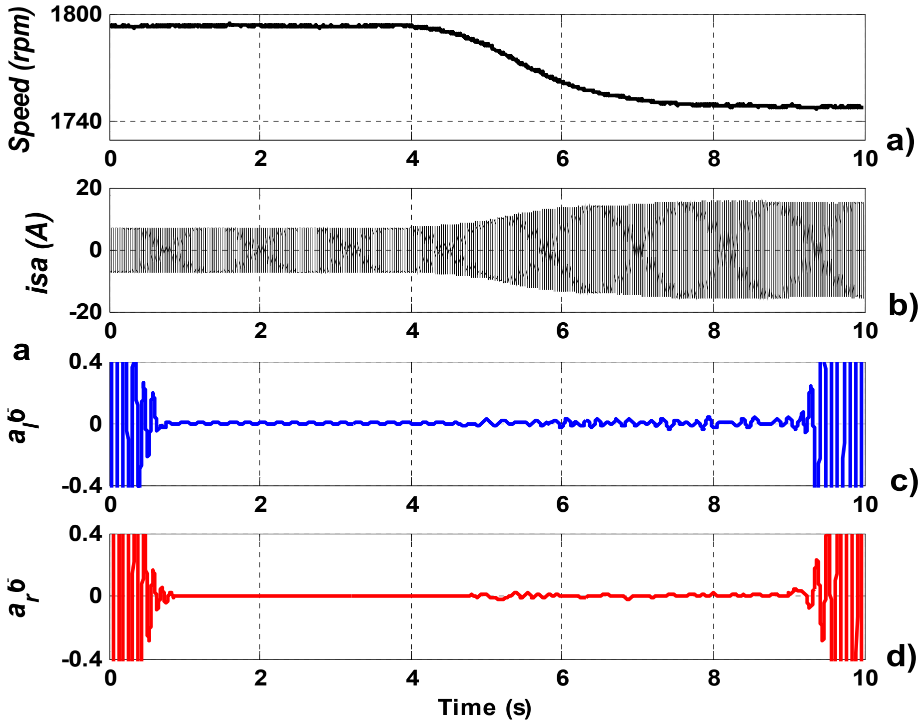

Fig. 4. 12 DWT analysis of stator current under transient operating condition (10%-90% rated load):a) speed profile, b) phase current, c) f_l component, and d) f_r component under healthy conditions

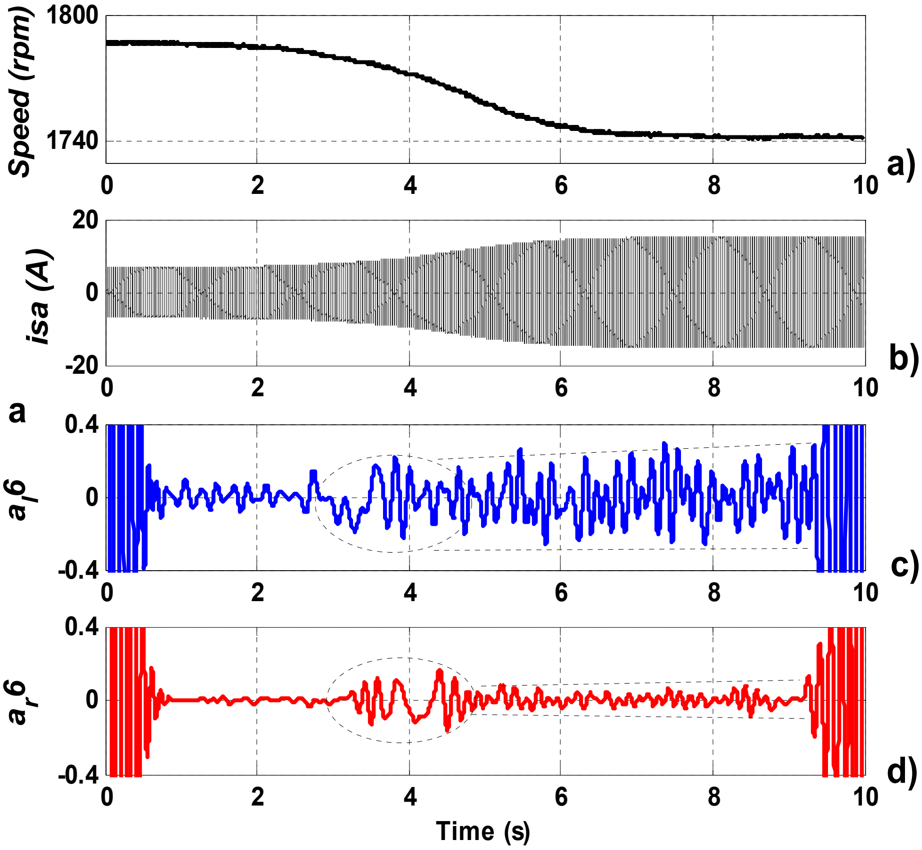

Fig. 4. 13 DWT analysis of stator current under transient operating condition (10%-90% rated load):a) speed profile, b) phase current, c) f_l component, and d) f_r componentwith3 broken outer cage bars

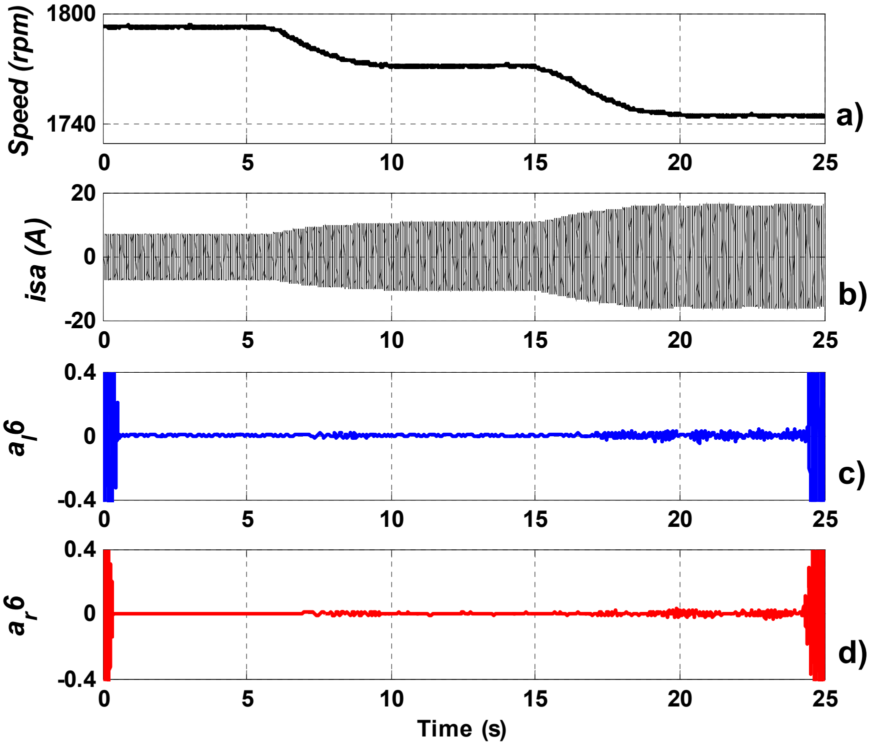

Fig. 4. 14 DWT analysis of stator current under transient operating condition (10%-50%-90% rated load): a) speed profile, b) phase current, c) fl component, and d) fr component under healthy conditions

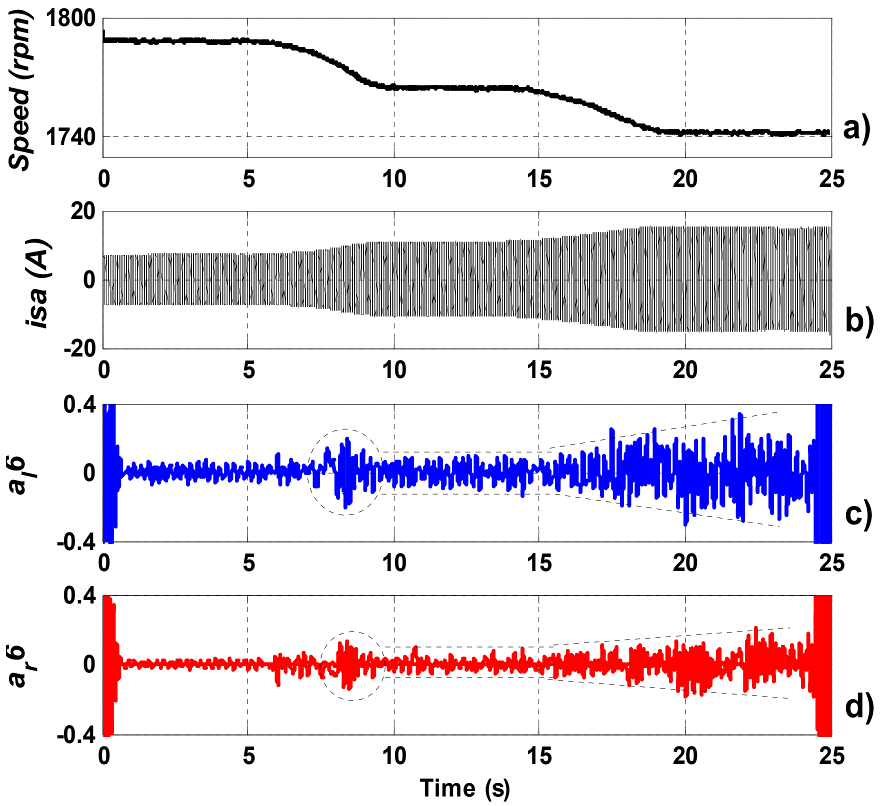

Fig. 4. 15 DWT analysis of stator current under transient operating condition (10%-50%-90% rated load):a) speed profile, b) phase current, c) f_l component, and d) f_r component with3 broken outer cage bars

4.3.1.2.2 Fault quantification

Once the state of the machine has been qualitatively diagnosed, a quantitative evaluation of the fault severity is necessary. The fault indicator is periodically calculated, every 400 samples, by using a window of 6400 samples (δx=400 samples, Δx=6400 samples). The values of δx and Δx were chosen according to the desired time sensitivity to observe the fault evolution.

The periodic calculation of the normalized fault indicator corresponding to the behavior of the healthy and faulty motors reported in Figs. 4.14 and 4.15, is depicted in Fig. 4.16. After repeating a number of tests, the fault indicator for the faulty case can be considered as a baseline for setting the threshold to discriminate healthy from faulty rotors with broken outer cage bar condition, as shown in Fig. 4.16.

The indicator F_{ind} which is proportional to the sum of a_6^l and a_6^r, shows significant increase under faulty conditions. The large energy deviation observed in faulty conditions under the load transient verifies the effectiveness of the proposed approach. The fault indictor under healthy conditions is always lower than that of the faulty case even under load transients, as can be seen in Fig. 4.16. The experimental results of Figs. 4.12-4.15 clearly show the main advantage of the proposed method: the outer cage faults in double cage motors can be reliably observed with high sensitivity even under time-varying load transients as the assessment is not disturbed for a healthy machine under load transients.

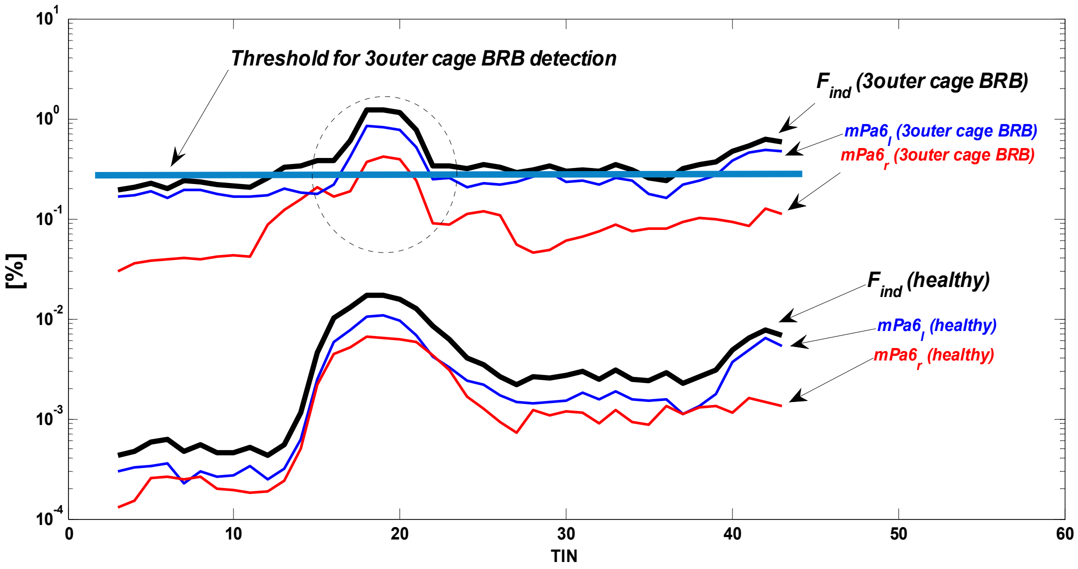

Fig. 4. 16 Values of the fault indicators: normalized Find (Black line)resulting from the 6th wavelet decomposition level of the stator current under healthy and faulty (3 broken outer cage bars) conditions with speed-varying conditions. Left side component (Blue line), and right side component (Red line)

4.3.2 Motor Vibration Signature Analysis

In healthy conditions only the fundamental frequency f exists in stator currents of a double cage induction machine. If the rotor part is damaged, the rotor symmetry of the machine is lost producing a reverse rotating magnetic field related to an inverse sequence component at frequency $-sf$. This inverse sequence is reflected on the stator side, producing the frequency $(1-2s)f$. These frequency components generate electromagnetic and mechanical interactions between stator and rotor parts. Consequently torque and speed ripple effects are generated at frequency $2sf$, which modulate the rotating magnetic flux [6].

This modulation produces two current components, i.e., an additional left-side component at $(1-2s)f$ and a right side component at $(1+2s)f$. Following this interaction process, the frequency content of the stator currents show series of fault components at the following frequencies $((1\pm 2ks)f)_{k=1,2,3,\ldots}$. More specifically, for large or double squirrel-cage motors, as long as the contact impedance between the rotor bars and iron core is small or the copper bars are directly inserted into the laminated iron slots, the broken bar is no longer a physical condition ensuring an open circuit and inter bar or cross-path currents can flow. As a consequence, these inter bar transverse currents interact with the radial stator flux density, generating axial forces. These facts lead mainly to the presence of a first chain of fault frequency components at $(f_{mec}\pm 2ksf)_{k=1,2,3,\ldots}$, and a second one at $((6-2ks)f)_{k=1,2,3,\ldots}$, in radial and axial vibration directions (f_{mec} denotes the mechanical speed of the motor) [15]- [18]. In the following, the focus will be exclusively on tracking the most relevant fault components of the harmonic chains$((6-2ks)f)_{k=1,2,3,\ldots}$ and $(f_{mec}\pm 2ksf)_{k=1,2,3,\ldots}$, issued from axial vibrations.

4.3.2.1 System description

In order to evaluate the performances of the proposed approach, two double cage induction motors are available; one healthy, and the second with a drilled broken bar (the bar was completely disconnected from the common end-ring). The characteristics of the double cage induction motors used for experiments are presented in Table 4.3. A three-phase autotransformer of 30 kVA, 0-380 V is used as motor regulated supply. A four quadrants 7,83 kW dc electrical drive is adopted to reach the different planned load conditions. One piezoelectric accelerometers Brüel & Kjær model 4507 B 005, was mounted for measuring axial vibrations of the core motors. Fig. 4.17 shows detailed photos of the healthy and drilled rotor (left), and details of the test-bed (right). In Fig. 4.18 and Fig. 4.19 instantaneous values of rotor speed and axial vibration signals are depicted for healthy and faulty conditions respectively. All signals reported have been recorded during 20 seconds. The tests were carried out considering a speed transient from 0% to 70% of full load.

Table. 4. 3 Data of the double rotor cage motor

Data	Value	
Rated Power	kW	5.5
Rated stator voltage	V	400
Rated current	A	13
Rated frequency	Hz	50
Rated speed	rpm	2870
Rotor diameter	mm	110
Axial length of the rotor	mm	90
Air gap length	mm	0.5
Number of stator slots		36
Number of rotor slots		30

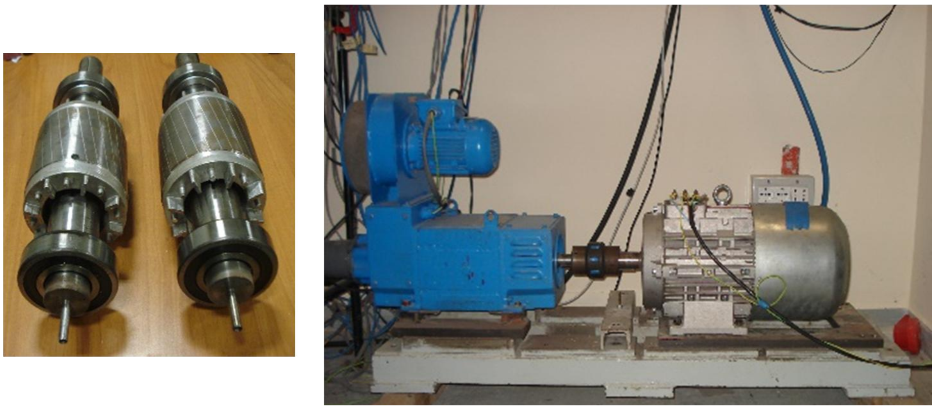

Fig. 4. 17 Photos of the healthy and drilled broken bar (left), and details of the test-bed (right)

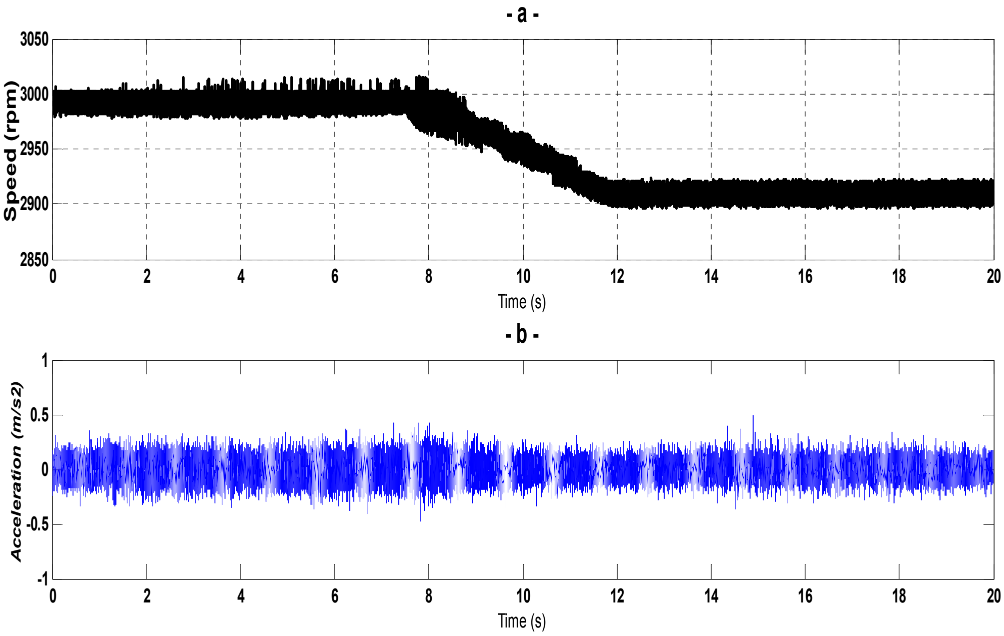

Fig. 4. 18 Instantaneous values of speed (a), and axial vibration signal (b) under healthy conditions

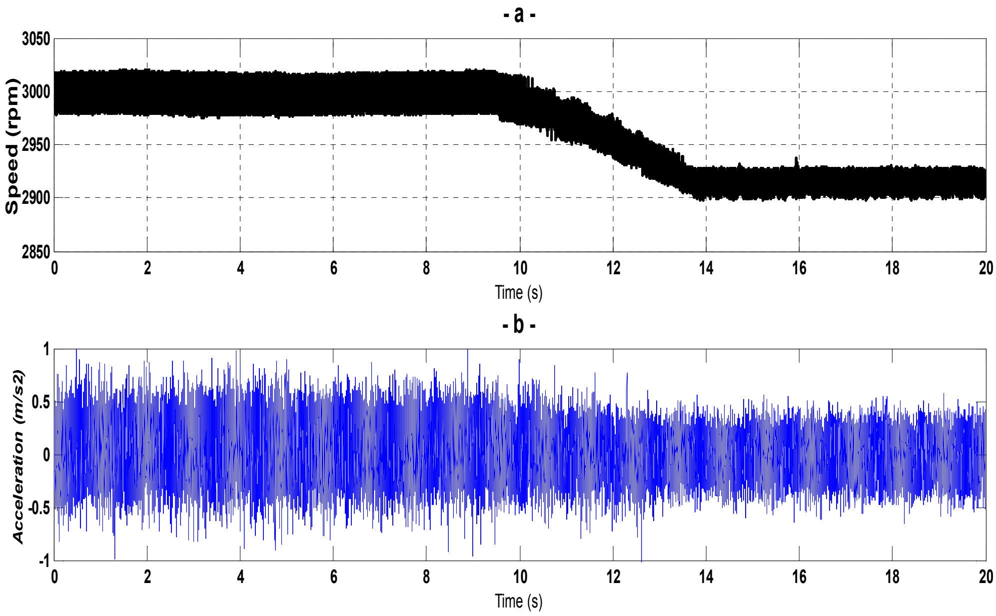

Fig. 4. 19 Instantaneous values of speed (a), and axial vibration signal (b) under broken bar

4.3.2.2 Results

4.3.2.2.1 Rotor Fault detection

With a sampling frequency f_s=2.0kHz, a six level decomposition (J=6) was chosen in order to cover the frequency bands in which we can track the contribution of the first chain of harmonic $((6\text{-}2ks)f)_{k=1,2,3,\ldots}$. The second chain of fault component

$(f_{mec}\pm 2ksf)_{k=1,2,3,\ldots}$, will be tracked in a frequency band corresponding to seven level decomposition (J=6). The frequency band repartition corresponding to the above decompositions are detailed in Table. 4.4. The chains of fault components $((6-2ks)f)_{k=1,2,3,\ldots}$ and $(f_{mec}\pm 2ksf)_{k=1,2,3,\ldots}$, will be tracked in the frequency bands [0: 15.625] and [0: 7.812] respectively, after appropriate frequency sliding applied to axial vibration signals. All signals reported have been recorded during 10 seconds.

Table. 4. 4 Frequency bands at each level of decomposition

Approximations «a_j»	*Frequency bands (Hz)*	*Details « d_j »*	*Frequency bands (Hz)*
a_7	: [0 – 7.812]	d_7	: [7.812 – 15.625]
a_6	: [0 – 15.625]	d_6	: [15.625 – 31.25]
a_5	: [0 – 31.25]	d_5	: [31.25 – 62.5]
a_4	: [0 – 62.5]	d_4	: [62.5 – 125]
a_3	: [0 – 125]	d_3	: [125 – 250]
a_2	: [0 – 250]	d_2	: [250 – 500]
a_1	: [0 – 500]	d_1	: [500 – 1000]

The wavelet decompositions of the axial vibration signals (v_{ax}) in healthy condition, for each chain or rotor fault components, are used as references in comparison to the faulty cases.

During the considered transient conditions, the investigated axial vibration signals under healthy and one drilled broken bar are depicted in Figs. (4.20-a, 4.22-a) and Figs. (4.21-a, 4.24-a) respectively. After a frequency sliding of 286.16 Hz applied to the axial vibration signals v_{ax} under healthy and one rotor broken bar condition, the resulting signals V_{sl} were analysed by DWT thereby. The corresponding Wavelet Analysis results (a_6), under healthy and faulty conditions are reported in Fig. 4.20-b and Fig.4.21-b respectively.

In healthy condition, the approximation signal of interest (a_6), depicted in Figure 4.20-b, shows very low variations. This indicates the absence of the chain of rotor fault component $((6-2ks)f)_{k=1,2,3,\ldots}$, leading to diagnose the healthy condition of the motor under speed-varying conditions. Under faulty condition, the contribution of the chain of fault components $((6-2ks)f)_{k=1,2,3,\ldots}$, observed on the 6th approximation signal, is very relevant in comparison to the healthy case (Fig. 4.21-b). More in detail, the oscillations observed in the signal a_6, with quasi-constant amplitude, follow a characteristic pattern that fits the evolution in frequency of the considered chain of fault components. The same observations are valuable for the contribution of the chain of rotor fault component $(f_{mec}\pm 2ksf)_{k=1,2,3,\ldots}$, observed under healthy and faulty conditions, in Fig. 4.22-b and Fig. 4.24-b respectively. The variations observed in the approximation signal a_7 are evident in faulty case (Fig. 4.22-b) in comparison to the healthy one (Fig. 4.24-b), leading to a clear discrimination between healthy and faulty conditions, through the evolution of the wavelet signal a_7.

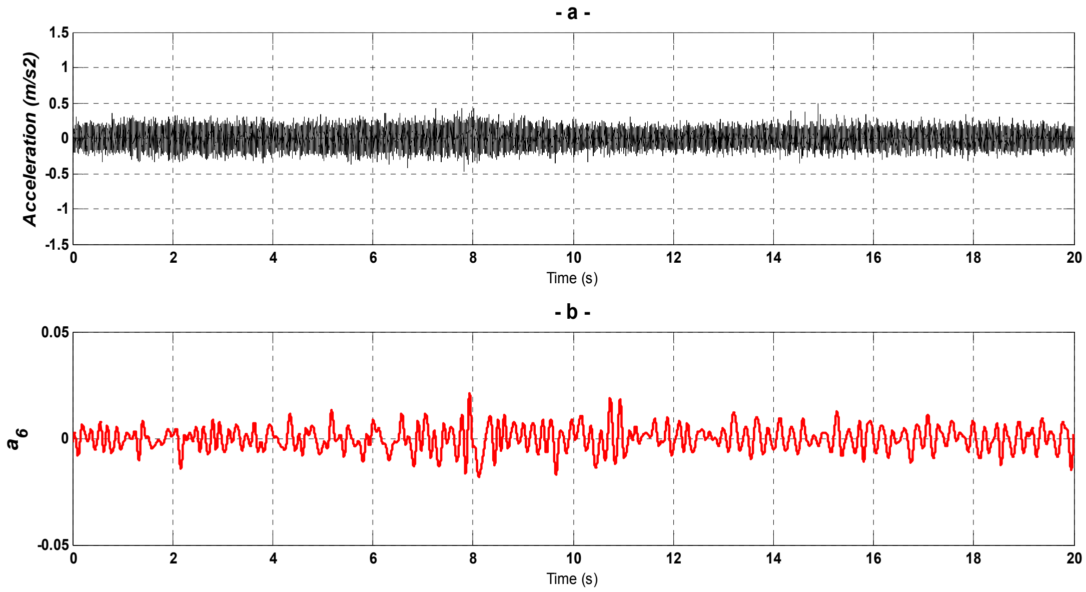

Fig. 4. 20 Instantaneous values of axial vibration signal (a), and its corresponding Wavelet analysis (b) under healthy condition

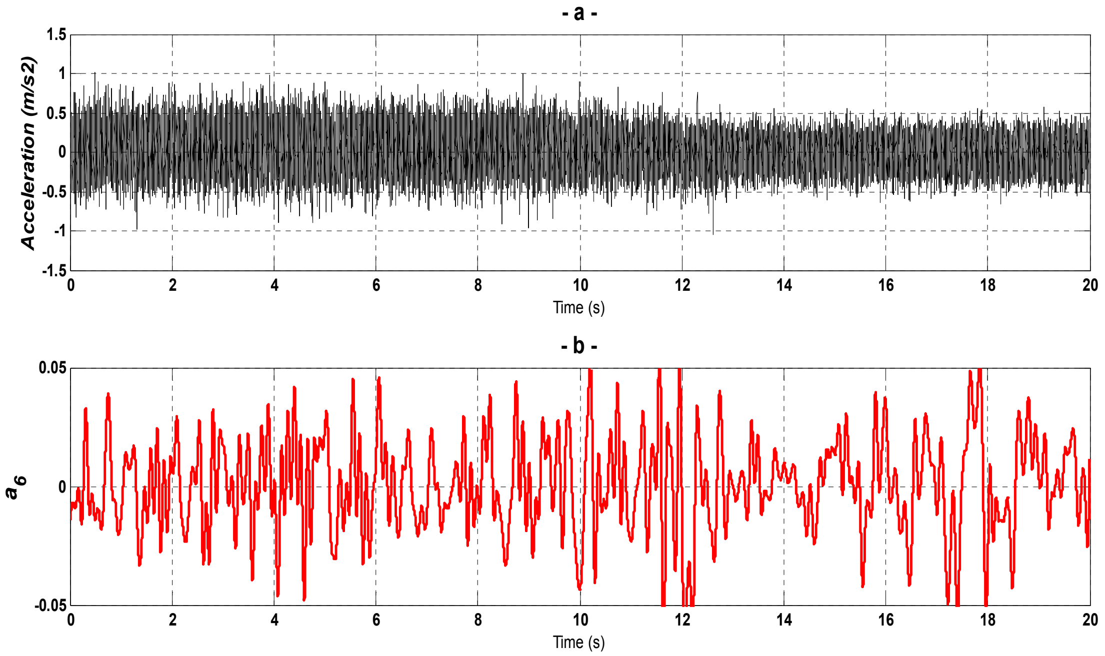

Fig. 4. 21 Instantaneous values of axial vibration signal (a), and its corresponding Wavelet analysis (b) under rotor broken bar.

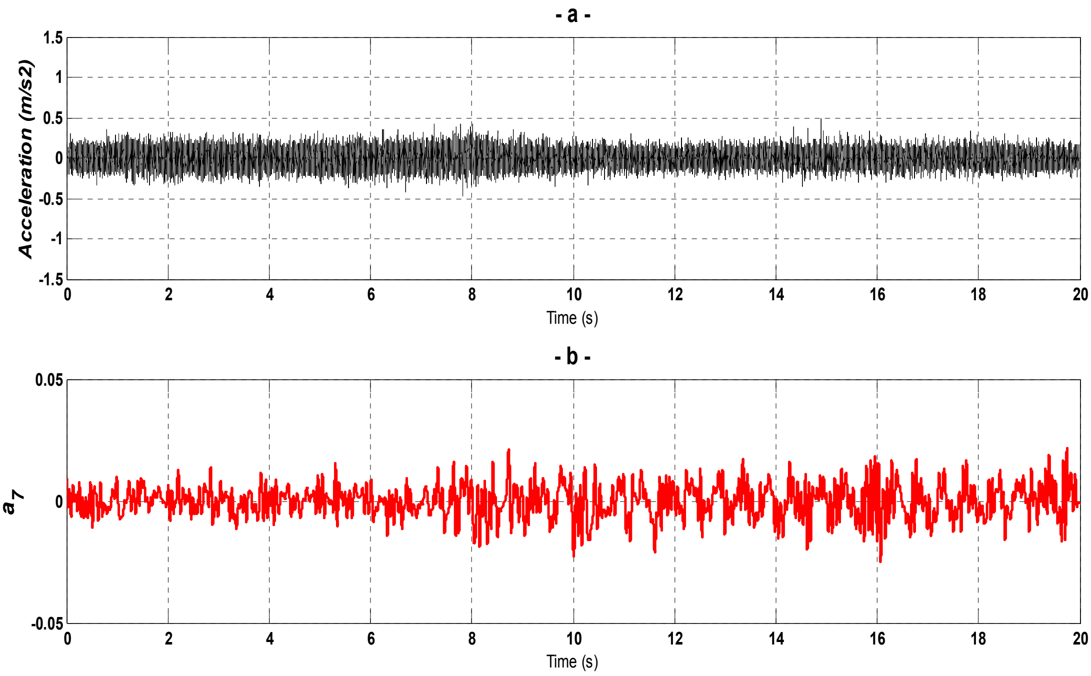

Fig. 4. 22 Instantaneous values of axial vibration signal (a), and its corresponding Wavelet analysis (b) under healthy condition

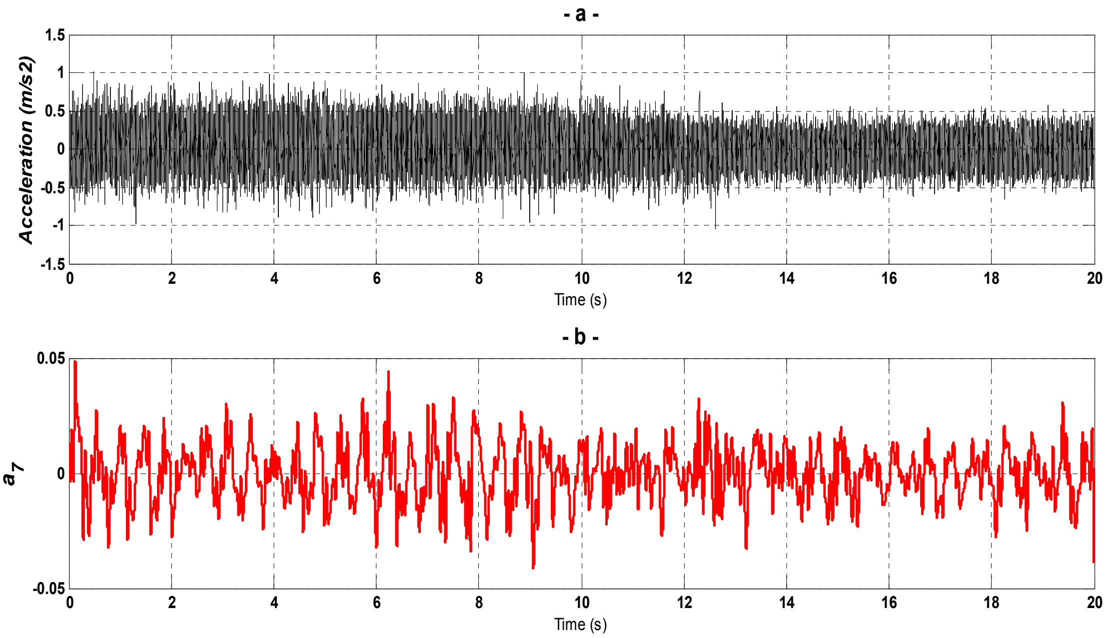

Fig. 4. 23 Instantaneous values of axial vibration signal (a), and its corresponding Wavelet analysis (b) under rotor broken bar.

4.3.2.2.2 Fault quantification

After the above qualitative analysis of the fault, a quantitative evaluation of the fault extend was conducted. The fault indicator is periodically calculated (every 400 samples) using a window of 6400 samples, where δn=150 samples and Δn=6400 samples.

The mean power calculation results, issued from the approximation signal a_6, which have been obtained in Figs. 4.20-b and 4.21-b, are depicted in Fig. 4.24. In healthy condition, the calculated mPa_6 indicator don't show any significant changes. Consequently, the indicator values for the healthy motor response are considered as a baseline to set the threshold for discriminating healthy from rotor broken bar conditions. In faulty conditions the calculated mPa_6 indicator shows significant increase. The large energy deviation observed in faulty conditions reflect the presence of the chain of rotor fault components $((6\text{-}2ks)f)_{k=1,2,3,\ldots}$, leading to an effective diagnosis procedure for broken bars in double squirrel cage induction machine.

The above conclusions are valid also for the quantification process related to the contribution of the chain of rotor fault components $(f_{mec}\pm 2ksf)_{k=1,2,3,\ldots}$, and depicted in Fig. 4.25 for the healthy and faulty cases. Other fault components could be treated in the same way for improving the quantification process.

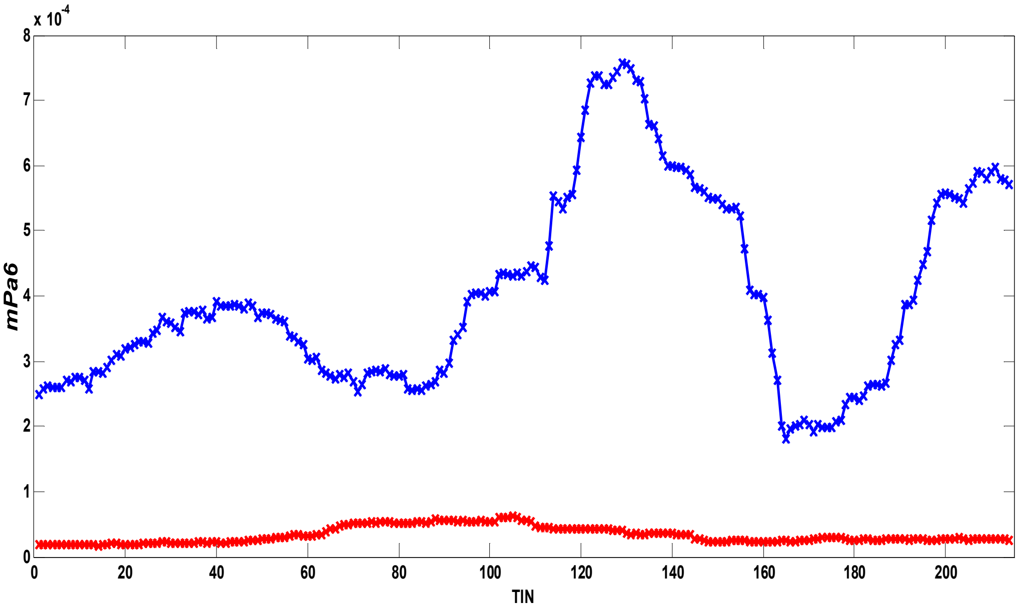

Fig. 4. 24 Cyclic values of the mPa6 fault indicator calculation issued from the approximation signal a6, under healthy (Red) and rotor broken bar (Blue) conditions.

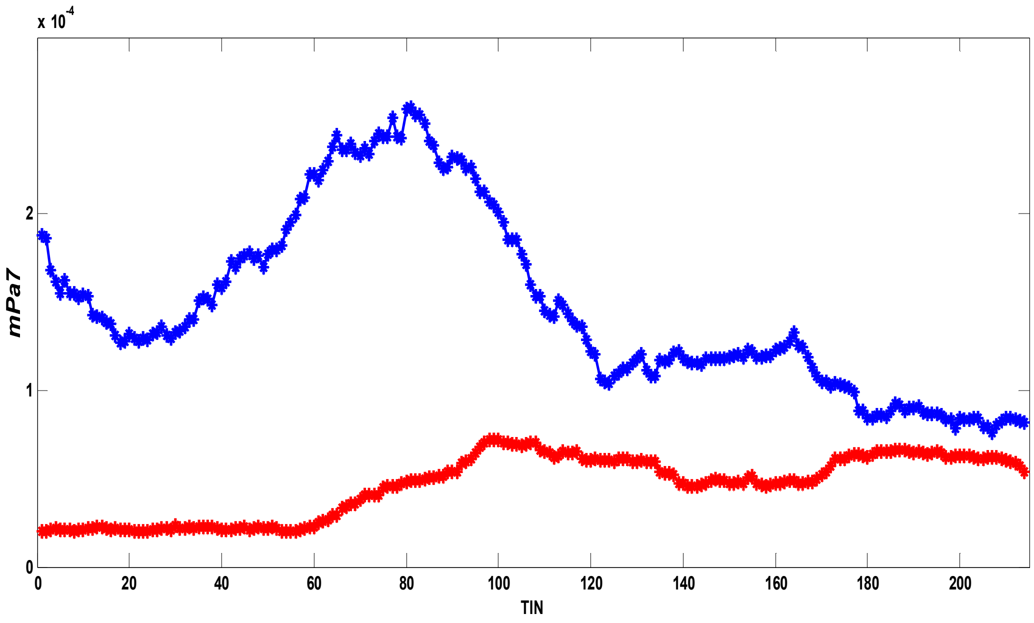

Fig. 4. 25 Cyclic values of the *mPa_7* fault indicator calculation issued from the approximation signal *a_7*, under healthy (Red) and rotor broken bar (Blue) conditions.

4.4 Conclusion

In this chapter, the proposed diagnosis technique was validated for the detection of rotor broken bars in squirrel cage induction motors. As first application, the proposed diagnosis technique was successfully applied for rotor broken bars detection for single cage induction machine, by investigating MCSA. The second part of this chapter is focused on the detection of rotor outer cage bar faults for double cage motors. Using the proposed diagnosis technique, motor current signature analysis and motor vibration signature analysis were successfully applied to the detection of outer cage faults, and for motors operating under time-varying conditions.

REFERENCES

[1] R.F. Walliser and C. F. Landy, "Assessment of interbar currents in double cage induction motors with broken bars," *IEEE Trans. Energy Convers.*, vol. 9, no. 1, pp. 159–164, Mar. 1994.

[2] R. Carlson, C.A. da Silva, N. Sadowski, Y. Lefevre, and M. Lajoie-Mazenc, "Analysis of the Effect of Inter-Bar Currents on the Performance of Polyphase Cage-Induction Motors, " *IEEE Trans. Ind. Appl.*, vol. 39, no. 6, pp. 1674–1680, Nov./Dec. 2003.

[3] D.G. Dorrell , P.J. Hollik, C.B. Rasmussen, "Analysis and Effects of Inter-Bar Current and Skew on a Long Skewed-Rotor Induction Motor for Pump Applications", *IEEE Trans. on Magn.,*vol. 43, no. 6, pp. 2534-2536, 2007.

[4] D.G. Dorrell, T.J.E. Miller, C.B. Rasmussen, "Inter-bar currents in induction machines", *IEEE Trans. Ind. Appl.*, vol. 39, no. 3, pp. 676–684, May/Jun. 2003.

[5] I. Kerszenbaum, C.F. Landy, "The existence of inter-bar currents in three phase squirrel cage motors with rotor-bar and end-ring faults," *IEEE Trans. Pow. Appar. and Syst.*, vol. PAS-103, no. 7, pp. 1854-1862, July 1984.

[6] A. Bellini, F. Filippetti, C. Tassoni, and G. A. Capolino, "Advances in diagnostic techniques for induction machines", *IEEE Trans. Ind. Electron.*, Vol.55, N° 12, Dec. 2008.

[7] J. Park, B. Kim, J. Yang, K. Lee, S.B. Lee, E.J. Wiedenbrug, M. Teska, and S. Han, " Evaluation of the detectability of broken rotor bars for double squirrel cage rotor induction motors," *Proc. of IEEE ECCE*, pp. 2493-2500, Sept. 2010.

[8] J. A. Daviu, M. R. Guasp, J. P. Linares, J. Park, S.B. Lee, J. Yoo, C. Kral, "Detecion of broken outer cage bars for double cage induction motors under the startup transient", *IEEE Trans. Ind. Appl.*, vol. 48, no. 5, pp. 1539–1548, Sep./Oct. 2012.

[9] J. Mroz, "Temperature field distribution of a double squirrel-cage rotor during startup," *IEE Proceedings – Electric Power Applications*, vol. 152, no. 6, pp. 1531-1538, Nov. 2005.

[10] Motors and generators, NEMA standards pub. MG 1-2006, 2006.

[11] P.L. Alger, and J.H. Wray, "Double and triple squirrel cages for polyphase induction motors," AIEE Transactions Part III – Power *Apparatus and Systems*, vol. 78, no.2, pp. 637-645, Jan. 1953.

[12] G.C. Stone, and I. Culbert, "The testing tools," *IEEE Industry Applications Magazine*, no. 14, vol. 6, pp. 48-53, Nov./Dec. 2008.

[13] *EXP 4000 Users Manual*, Baker Instrument Company – An SKF Group Company, Fort Collins, CO, Feb. 2010.

[14] A. Bouzida, O. Touhami, R. Ibtiouen, A. Belouchrani, M. Fadel, and A. Rezzoug, “Fault diagnosis in industrial induction machines through discrete wavelet transform,” *IEEE Trans. Ind. Electron.*, vol. 58, no. 9, pp. 4385–4395, Sep. 2011.

[15] G. H. Muller and C. F. Landy, "A novel method to detect broken rotor bars in squirrel cage induction motors when interbar currents are present, " IEEE Trans. on Energy Conversion, Vol. 18, N° 1, pp. 71-79, Mar. 2003.

[16] C. Concari, G. Franceschini, and C. Tassoni, " Differential Diagnosis Based on Multivariable Monitoring to Assess Induction Machine Rotor Conditions", *IEEE Trans. on Ind. Electronics*, Vol. 55, N° 12, Dec. 2008.

[17] J. J. Rangel-Magdaleno, R. J. Romero-Troncoso, R. A. Osornio-Rios, E. Cabal-Yepez, and L. M. Contreras-Medina, "Novel Methodology for Online Half-Broken-Bar Detection on Induction Motors", *IEEE Trans. on Inst. and Meas.*, Vol. 58, N° 5, May. 2009.

[18] A. Sadoughi, M. Ebrahimi, M. Moalem, and S. Sadri, "Intelligent Diagnosis of Broken Bars in Induction Motors Based on New Features in Vibration Spectrum", *The IEEE-SDEMPED'07*, pp. 106-111. Sep. 2007.

CHAPTER 5 : FAULT DIAGNOSIS EXTENSION FOR MULTIPHASE ELECTRICAL MACHINES

5.1 Introduction

In this chapter, the proposed diagnosis technique is extended to faults detection in Multiphase electrical machines. Multiphase Permanent-Magnet Generators are an attractive alternative to induction machines for a variety of applications owing to their reliability and dynamic performance, suited for emerging applications such as automotive or traction systems. In this context, diagnosing the status of the rotor magnets is crucial for improving the reliability of the generators. This Chapter is firstly focused on the demagnetization of the rotor magnet trailing edges, due to large stator currents, in five-phase surface-mounted permanent magnet synchronous generators under Time-varying conditions. Consequently, the classical application of Fourier analysis for processing the back-emf induced in the α-β planes fails as the fault components intended to be monitored to assess the magnets status are spread in a bandwidth proportional to the speed variation. In this context, the back-emf induced in the α-β planes is analyzed by the proposed diagnosis technique for the detection of rotor demagnetization in multiphase surface-mounted permanent magnet generator under speed-varying conditions. The proposed methodology is validated by means of two dimensional (2-D) Finite Element Analysis (FEA) and numerical simulations. Moreover, a cyclic quantification of the fault extent over time was introduced for accurate rotor fault detection.

The second subpart of this section investigates the behavior of multiphase induction machines with an odd number of phases in investigated under the assumption that the stator winding is unbalanced owing to a fault or an incipient damage. The analysis leads to a method to assess the unbalance condition of the machine, based on the calculation of the space vectors of the stator currents in the available α-β planes. Experimental results for the analysis established in time and frequency domains show interesting results to be extended to time-frequency domain.

5.2 Characterization of Rotor Demagnetization in Five-Phase Surface–Mounted Permanent Magnet Generator

5.2.1 System description

The numerical modeling of the used five-phase surface-mounted PMSG is developed for healthy and local magnet demagnetization conditions. Multiple space vector theory is considered to represent the five-phase system by two space vectors and a zero-sequence component as detailed in Appendix.2. Under the assumptions usually adopted for the analysis of ac machines, the magnetic field produced by the stator windings in the air gap can be expressed in a stator reference frame in terms of stator current space vectors in the following compact form:

$$h_S\left(\theta_S,t\right)=\frac{5\,N_S}{2\pi\,\delta\,p}\Re_e\left[K_{wS1}\,\bar{i}_{S1}\,e^{-j\theta_S}-\frac{K_{wS3}}{3}\bar{i}_{S3}\,e^{-j3\theta_S}-\frac{K_{wS7}}{7}\bar{i}^{*}_{S3}\,e^{-j7\theta_S}+\frac{K_{wS9}}{9}\bar{i}^{*}_{S1}\,e^{-j9\theta_S}\right] \tag{5. 1}$$

where, N_S is the number of series-connected conductors per phase, δ is the air gap length, p the number of pairs of poles, $\Re_e$ the real part operator, $K_{wS\rho}$ the ρ-th winding coefficient, θ_S a stationary angular coordinate in electrical radians whose origin is aligned with the magnetic axis of phase 1, whereas $\bar{i}_{S1}$ and $\bar{i}_{S3}$ are the stator current space vectors.

The symbol "*" identifies the complex conjugate quantities. Besides the fundamental component, (5.1) takes into account the third, the seventh and the ninth spatial harmonics, and is expressed in terms of the instantaneous values of the stator current vectors. It is worth noting that the fifth spatial harmonic is null, since it can be generated only by the zero-sequence component of the stator currents, which is zero owing to the star connection of the windings.

With the usually adopted control strategy for PMSGs, the air gap distribution of the stator MMF is maximum along the quadrature axis. In this way, one half of each magnet is reverse magnetized. This can lead to a local demagnetization of the rotor magnets, which is reproduced by simply removing part of the magnetic material from the trailing edge.

The magnetic field produced by the rotor magnets in the air gap, in a rotor reference frame, can be written as:

$$\begin{aligned}h_R\left(\theta_R,t\right)=\frac{2\,H_M}{\pi}\Re_e\Big[&\left(e^{j(\gamma+\Delta\gamma)}+e^{-j\gamma}\right)e^{-j\theta_R}\\&-\frac{1}{3}\left(e^{j3(\gamma+\Delta\gamma)}+e^{-j3\gamma}\right)e^{-j3\theta_R}+\frac{1}{5}\left(e^{j5(\gamma+\Delta\gamma)}+e^{-j5\gamma}\right)e^{-j5\theta_R}\\&-\frac{1}{7}\left(e^{j7(\gamma+\Delta\gamma)}+e^{-j7\gamma}\right)e^{-j7\theta_R}+\frac{1}{9}\left(e^{j9(\gamma+\Delta\gamma)}+e^{-j9\gamma}\right)e^{-j9\theta_R}\Big]\end{aligned} \tag{5. 2}$$

where, θ_R is an angular coordinate in electrical radians in the rotor reference frame, π-2γ is the pole arc of the surface-mounted permanent magnets, and $\Delta\gamma$ identifies the demagnetized portion of the magnets (Fig. 5.1).

By neglecting the slot opening effect, and assuming a unitary relative recoil permeability of the magnets, the value of H_M can be expressed as:

$$H_M=\frac{\delta_M\,B_R}{\delta\,\mu_0}, \tag{5. 3}$$

where, δ_M is the magnet thickness, and B_R is the residual flux density of the magnet material.

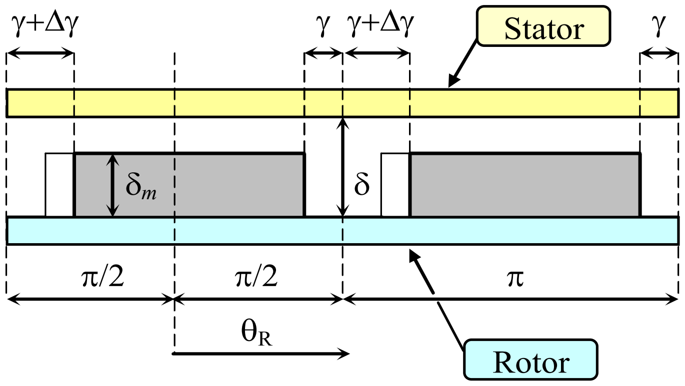

Fig. 5. 1 Schematic draw of a pair of surface-mounted permanent magnets in healthy and fault conditions

Besides the fundamental component, (5.2) takes into account the third, the fifth, the seventh and the ninth spatial harmonics. Fig. 5.2 shows the amplitude variation of every single spatial harmonic in the flux density distribution as a function of the pole arc reduction Δγ in electrical radians for the considered machine (Table.5.1).

Table. 5. 1 Five-Phase PMSG Parameters (FEA)

Rated torque	12 Nm
Torque over current ratio	2.4 Nm/A
Rated speed	3000 rpm
Phase resistance	0.55 Ohm
Phase reactance (100 Hz)	4.5 Ohm
Pole number	4
Stator inner radius	40 mm
Stator outer radius	68 mm
Stack length	100 mm
Slot number	40
Slot opening width	1.8 mm
Slot opening depth	0.5 mm
Stator winding pitch	9/10
Radius of the rotor surface	36 mm
Magnet-arc to pole-pitch ratio	77.14 / 90
Magnet radial thickness	3 mm
Magnet remanence	1.3 T
Relative recoil permeability	1.13
Magnetization type	Radial

The amplitudes are normalized by the amplitude of the fundamental. It is a matter of fact that a reduction of the pole arc leads to a variation of the harmonic content in the flux linkage, and thus in the back-emf. In the present work, and as it is detailed below, the focus is exclusively on tracking the contribution of the ninth and seventh inverse harmonics issued from the back-emf.

To evaluate the stator linkage fluxes, it is necessary to consider the contributions of the air gap magnetic field and of the leakage fluxes. The air gap magnetic field contribution can be derived by means of (5.1) and (5.2).

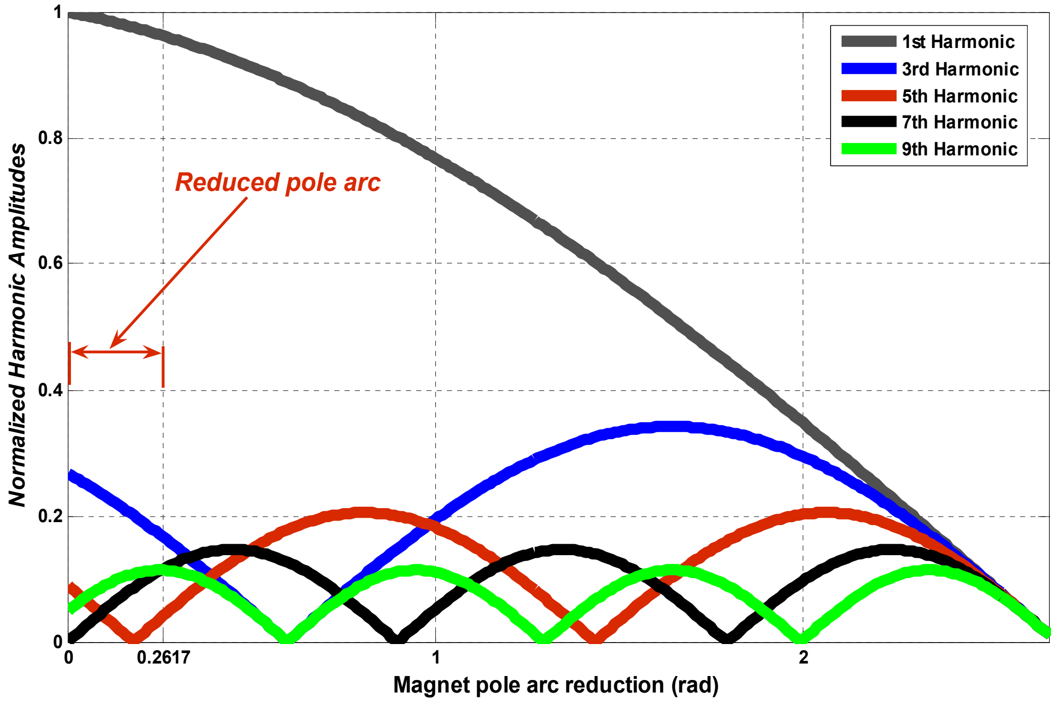

Fig. 5. 2 Harmonic amplitude variation in the flux density distribution as a function of the magnet pole arc reduction Δγ in electrical radians

The contribution of the leakage fluxes can be easily described by introducing two leakage inductances (the leakage inductances L_{Sd1} and L_{Sd3} for the α_1-β_1 and α_3-β_3 planes, respectively).

In conclusion, the mathematical model of the surface-mounted PMSG, written in terms of multiple space vectors, can be written as follows:

$$v_{S0} = \frac{d\phi_{S0}}{dt}, \tag{5. 4}$$

$$\overline{v}_{S1} = R_S\,\overline{i}_{S1} + \frac{d\overline{\phi}_{S1}}{dt}, \tag{5. 5}$$

$$\overline{v}_{S3} = R_S\,\overline{i}_{S3} + \frac{d\overline{\phi}_{S3}}{dt}, \tag{5. 6}$$

where the zero-sequence and the α1-β1 and α3-β3 space vectors of the linkage fluxes are given by

$$\phi_{S0} = \Re_e\left[\bar{\phi}_{M5}\, e^{j5\theta}\right] , \tag{5. 7}$$

$$\bar{\phi}_{S1} = L_{S1}\,\bar{i}_{S1} + \bar{\phi}_{M1}\, e^{j\theta} + \bar{\phi}_{M9}\, e^{-j9\theta} , \tag{5. 8}$$

$$\bar{\phi}_{S3} = L_{S3}\,\bar{i}_{S3} + \bar{\phi}_{M3}\, e^{j3\theta} + \bar{\phi}_{M7}\, e^{-j7\theta} . \tag{5. 9}$$

In (5.7)-(5.9), θ is the rotor position in electrical radians, whereas L_{S1} and L_{S3} are the α1-β1 and α3-β3 synchronous inductances, which can be expressed as

$$L_{S1} = L_{Sd1} + L_{SS}\left(K_{wS1}^2 + \frac{K_{wS9}^2}{81}\right), \tag{5. 10}$$

$$L_{S3} = L_{Sd3} + L_{SS}\left(\frac{K_{wS3}^2}{9} + \frac{K_{wS7}^2}{49}\right), \tag{5. 11}$$

where

$$L_{SS} = \frac{5\,\mu_0\, L\,\tau\, N_S^2}{2\,\pi^2\,\delta\, p}, \tag{5. 12}$$

and τ is the pole pitch.

The space vectors of the fluxes linked with the stator windings due to the permanent magnet field harmonics, can be expressed as follows:

$$\bar{\phi}_{m1} = \phi_M\, K_{wS1}\left[e^{j(\gamma+\Delta\gamma)} + e^{-j\gamma}\right] \tag{5. 13}$$

$$\bar{\phi}_{m3} = \phi_M\, \frac{K_{wS3}}{9}\left[e^{j3(\gamma+\Delta\gamma)} + e^{-j3\gamma}\right] \tag{5. 14}$$

$$\bar{\phi}_{m7} = \phi_M\, \frac{K_{wS7}}{49}\left[e^{-j7(\gamma+\Delta\gamma)} + e^{j7\gamma}\right] \tag{5. 15}$$

$$\bar{\phi}_{m9} = \phi_M\, \frac{K_{wS9}}{81}\left[e^{-j9(\gamma+\Delta\gamma)} + e^{j9\gamma}\right] \tag{5. 16}$$

where

$$\phi_M = \frac{2\,\mu_0\, L\,\tau\, N_S\, H_M}{\pi^2} \tag{5. 17}$$

The electromagnetic torque T_{em} assumes the following form:

$$T_{em} = T_{em,1} + T_{em,3} + T_{em,7} + T_{em,9} \tag{5. 18}$$

where

$$T_{em,1} = \frac{5}{2} p\, K_{wS1}\, \phi_M \left[\bar{i}_{S1} \cdot j\left(e^{j(\gamma+\Delta\gamma)} + e^{-j\gamma}\right) e^{j\theta} \right] \tag{5. 19}$$

$$T_{em,3} = \frac{5}{2} p \frac{K_{wS3}}{3} \phi_M \left[\bar{i}_{S3} \cdot j\left(e^{j3(\gamma+\Delta\gamma)} + e^{-j3\gamma}\right) e^{j3\theta} \right] \tag{5. 20}$$

$$T_{em,7} = \frac{5}{2} p \frac{K_{wS7}}{7} \phi_M \left[\bar{i}^{*}_{S3} \cdot j\left(e^{j7(\gamma+\Delta\gamma)} + e^{-j7\gamma}\right) e^{j7\theta} \right] \tag{5. 21}$$

$$T_{em,9} = \frac{5}{2} p \frac{K_{wS9}}{9} \phi_M \left[\bar{i}^{*}_{S1} \cdot j\left(e^{j9(\gamma+\Delta\gamma)} + e^{-j9\gamma}\right) e^{j9\theta} \right] \tag{5. 22}$$

As can be seen, four torque contributions are present, each one identified by the order of the related spatial harmonic in the air gap.

Contributions $T_{em,1}$ and $T_{em,3}$ can be ripple free owing to the synchronization of $\bar{i}_{S1}$ with $e^{j\theta}$, and $\bar{i}_{S3}$ with $e^{j3\theta}$. On the contrary, contributions $T_{em,7}$ and $T_{em,9}$ are oscillating, because $\bar{i}^{*}_{S3}$ is not synchronized with $e^{j7\theta}$, as well as $\bar{i}^{*}_{S1}$ is not synchronized with $e^{j9\theta}$.

Note that the stator current space vector $\bar{i}_{S3}$ is usually kept equal to zero by the control system in a standard five-phase drive. A non-zero value of $\bar{i}_{S3}$ is used only in high torque density motor drives, as discussed in [1]-[4]. In the present investigation, a null value of $\bar{i}_{S3}$ is assumed. Consequently, only the contribution $T_{em,9}$ has to be minimized in order to reduce the torque ripple. This goal can be obtained either by an opportune choice of the permanent magnet pole arc or by suitable short-pitch stator windings. Taking into account (5.5), (5.6), (5.8), (5.9), (5.13), (5.14), (5.16) and (5.17), the space vectors $\bar{e}_{S1}$ and $\bar{e}_{S3}$ of the back-emf, can be expressed as shown in (5.23) and (5.24), which emphasize the low order harmonic content of the back-emf space vectors.

$$\begin{aligned}\bar{e}_{S1} = {} & j\,2\,\omega\phi_M\, K_{wS1} \cos\left(\gamma + \frac{\Delta\gamma}{2}\right) e^{j\frac{\Delta\gamma}{2}}\, e^{j\theta} \\ & - \frac{j\,2\,\omega\phi_M\, K_{wS9}}{9} \cos\left(9\gamma + \frac{9\Delta\gamma}{2}\right) e^{-j\frac{9\Delta\gamma}{2}}\, e^{-j9\theta}\end{aligned} \tag{5. 23}$$

$$\begin{aligned}\bar{e}_{S3} = {} & \frac{j\,2\,\omega\phi_M\, K_{wS3}}{3} \cos\left(3\gamma + \frac{3\Delta\gamma}{2}\right) e^{j\frac{3\Delta\gamma}{2}}\, e^{j3\theta} \\ & - \frac{j\,2\,\omega\phi_M\, K_{wS7}}{7} \cos\left(7\gamma + \frac{7\Delta\gamma}{2}\right) e^{-j\frac{7\Delta\gamma}{2}}\, e^{-j7\theta}\end{aligned} \tag{5. 24}$$

In order to validate the theoretical analysis of the emf harmonic content under speed varying-conditions, the simulation of a five-phase surface-mounted PMSG has been carried out using FEA. The parameters of the generator are summarized in Table 5.1. A double-layer stator winding, having two slots per pole and per phase, with 9/10 coil pitch, is considered (K_{wS9} = 0.024). The pole arc for the surface-mounted permanent magnet has been reduced of one seventh in respect to the polar pitch in order to eliminate the seventh harmonic in the resulting emf. The cross-section of the five-phase PMSG, with a superimposed flux plot obtained by FEA, in healthy no-load conditions, is shown in Fig. 5.3.

The simulations have been performed in no-load conditions under speed varying conditions (from 1500rpm to 3000rpm), firstly with healthy magnets ($\Delta\gamma = 0°$) and, then, with magnets having a reduced pole arc ($\Delta\gamma = 15°$) in order to reproduce a demagnetization on the trailing edges. By means of the FEA simulations, the linkage fluxes with the five stator phases have been determined as function of the rotor position. For the analysis of the sensitivity to the fault, the emfs have been divided by the rotor speed (expressed in electrical radians) obtaining the so called 'normalized emf'.

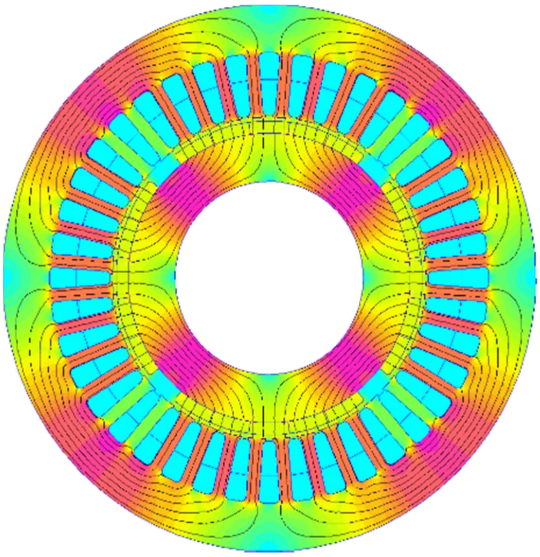

Fig. 5. 3 Cross-section of the five-phase PMSG, with a superimposed flux plot obtained by FEA, in healthy no-load conditions.

The large speed transient profile adopted during the simulations under healthy and faulty conditions is depicted in Fig. 5.4-a. The corresponding back-emfs under faulty conditions are depicted in Fig. 5.4-b. All signals reported have been recorded during 15 seconds, with a sampling frequency of 3.2 kHz.

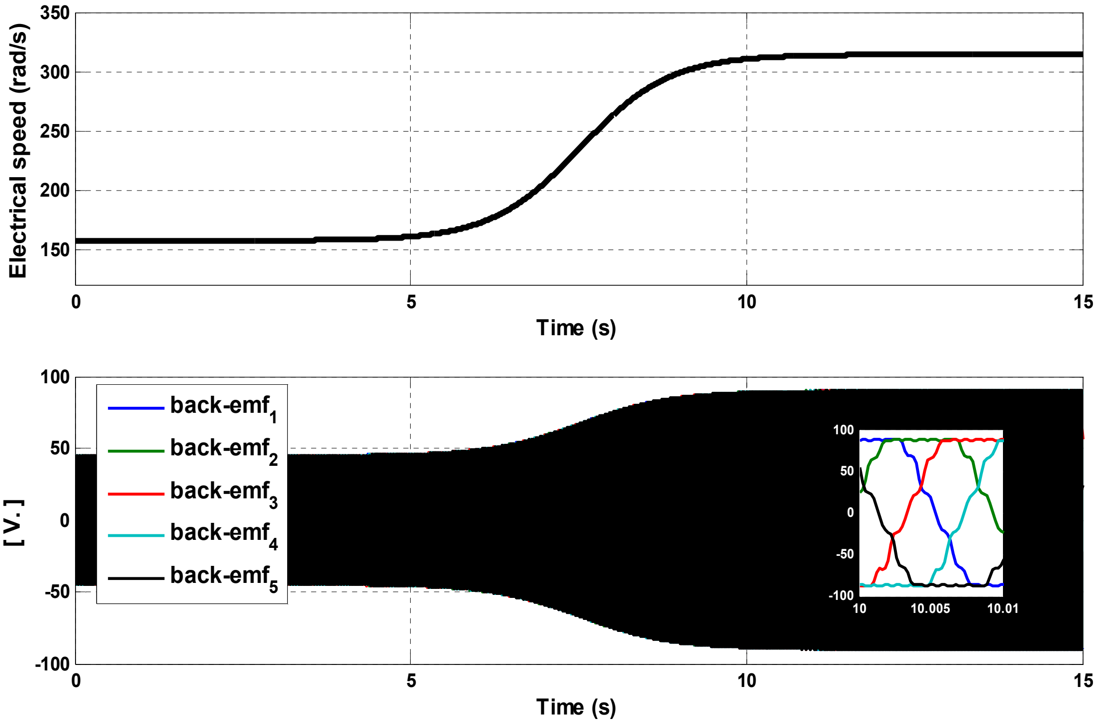

Fig. 5. 4 Instantaneous values of the electrical speed (a), and the corresponding back-emfs under faulty conditions

5.2.2 Results

With reference to the machine whose parameters are reported in Table 5.1, the sampling frequency f_s is chosen equal to 3.2kHz and a three-level decomposition (J=3) is adopted to cover the frequency bands in which the frequency component characteristics of the fault can be tracked (see Table 5.2).

As explained in Section III, the contribution of 7th inverse harmonic component of the normalized back-emf space vector $\bar{e}_{s3}/\omega$ can be observed in the approximation signal a_3 after appropriate sliding frequency. In order to isolate the contribution of the 7th inverse harmonic fault component in the frequency band of the approximation signal a_3, a sliding frequency $f_{sl} = -(7f_S+12.5\text{ Hz})$ was chosen to shift the α_3-β_3 components of the normalized back-emfs under healthy and faulty conditions. As already explained, the sliding frequency is chosen in such a way that the expected fault harmonic is shifted in the middle of the frequency band of the approximation signal a_3. The results of this analysis are shown in Figs. 5.5-5.6. The wavelet decomposition obtained when the machine is healthy should be compared with the one obtained in the case of faulty rotor. The absence of amplitude variations in a_3 (Fig. 5.5-b) is due to the low contribution of the 7th harmonic in healthy conditions, which allows one to diagnose the healthy state of the machine. By contrast, under a local demagnetization (Fig. 5.6-b) , it is possible to notice an amplitude increase in the approximation signal a_3, in comparison to the healthy case (Fig. 5.5-b). This result means a clear detection of rotor demagnetization.

Table. 5. 2 Frequency band of each level

Approximations «a_j»	*Frequency bands (Hz)*	*Details « d_j»*	*Frequency bands (Hz)*
a_3	: [0 – 200]	d_3	: [200 – 400]
a_2	: [0 – 400]	d_2	: [400 – 800]
a_1	: [0 – 800]	d_1	: [800– 1600]

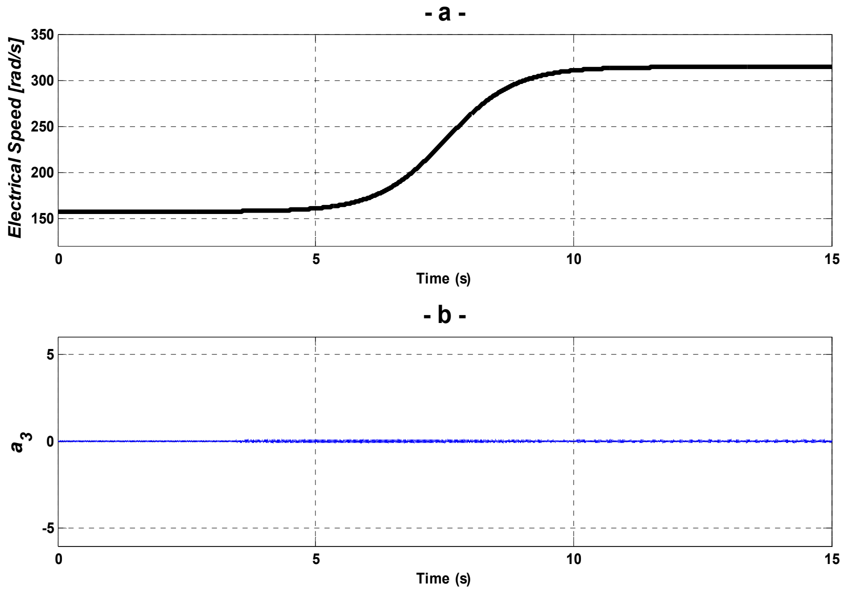

Fig. 5. 5 Instantaneous values of the electrical speed (a), and the third approximation signal (a_3) issued from Wavelet analysis of the α_3-β_3 components of the back-emf space vector under healthy conditions.

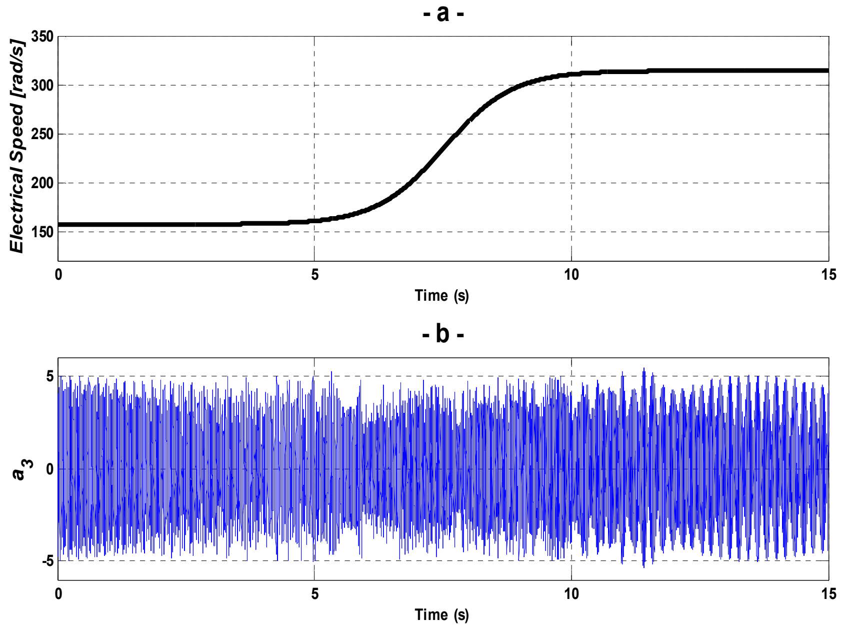

Fig. 5. 6 Instantaneous values of the electrical speed (a), and the third approximation signal (a_3) issued from Wavelet analysis of the α_3-β_3 components of the back-emf space vector under local rotor magnet demagnetization conditions.

Once the state of the machine has been qualitatively diagnosed, a quantitative evaluation of the fault severity is necessary. The fault indicator is periodically calculated, every 400 samples, by using a window of 6400 samples (δx=400 samples, Δx=6400 samples). The values of δx and Δx were chosen according to the desired time sensitivity to observe the fault evolution. Fig. 5.7 shows the shapes of the corresponding fault indicators in faulty and healthy conditions respectively. These results mean that the proposed methodology leads to a clear detection of rotor demagnetization.

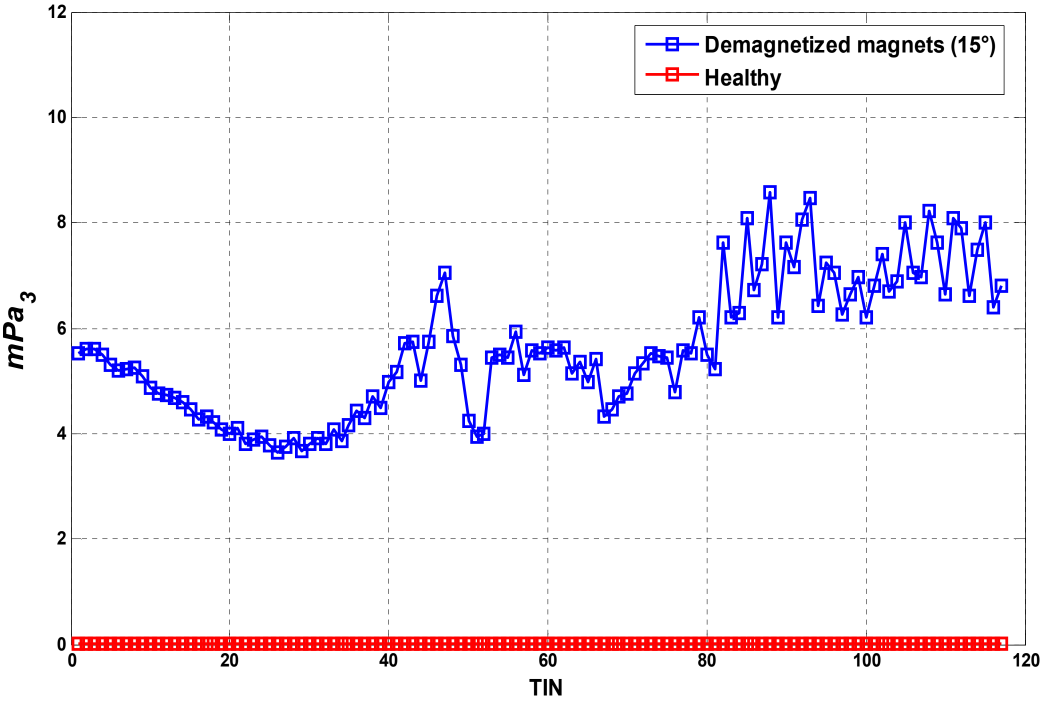

Fig. 5. 7 Values of the fault indicator mPa_3 (e_{S3}), corresponding to the 7th inverse harmonic component, resulting from the approximation signal a_3 under large speed transient, for healthy and local rotor demagnetization (15°) conditions.

5.3 Characterization of stator fault in seven-phase induction machine

Multiphase drives are receiving an increasing attention by the research community in high power applications. In this section, the behavior of seven-phase induction machine is investigated under incipient stator unbalance. The analysis leads to a method to assess the unbalance condition of the machine, based on the calculation of the space vectors of the stator currents in the available α-β planes. The analytical model of a multiphase induction motor with unbalanced stator winding is completely developed in [5] . The investigation of the current stator space vectors in the available α-β planes has shown interesting results for stator fault detection and localization. Results are confirmed by experimental tests.

5.3.1 System description

Multiphase machines are usually fed by a multiphase inverter, whose command signals are calculated by a control system within a closed-loop scheme. Nevertheless it is of some interest to analyze the behavior of machine under the assumption that the control scheme is an open loop, such as the constant V/Hz control scheme. The main reason is that the understanding of such control schemes is the starting point for more complex cases.

A complete drive system has been built and some experimental tests have been realized. The experimental set-up consists of a 7-phase IGBT inverter and a 4 kW, 7-phase, 4-pole squirrel cage induction motor. The parameters of the motors are shown in Table 5.3. A schematic diagram and some pictures of the experimental set-up are shown in Fig. 5.8. The control algorithm is very simple, without any form of compensation of the voltage drop on the stator impedance.

All the tests have been carried out by feeding the motor with 80 V at 25 Hz. The resulting motor speed in healthy conditions is around 700 rpm, and the load has been adjusted so that the torque produced by the motor is 15 Nm, i.e., about two third of the rated torque.

During the experimental tests, an extern resistor has been added in series with the machine phases to reproduce a fault condition in a non-destructive way.

Table. 5. 3 Parameters of the Seven-Phase Machine

T_{rated} = 24 Nm	L_{S1} = 180 mH
$I_{s,max}$ = 7.5 A$_{\text{(peak)}}$	L_{R1} = 180 mH
$I_{S1d,rated}$ = 3.6 A$_{\text{(peak)}}$	M_1 = 175 mH
f_{rated} = 50 Hz	L_{S3} = 24 mH
R_S = 1.3Ω	L_{R3} = 24 mH
R_{R1} = 1.0Ω	M_3 = 19 mH
R_{R3} = 0.8Ω	L_{S5} = 10 mH
R_{R5} = 0.6Ω	L_{R5} = 10 mH
$p = 2$	M_5 = 7mH

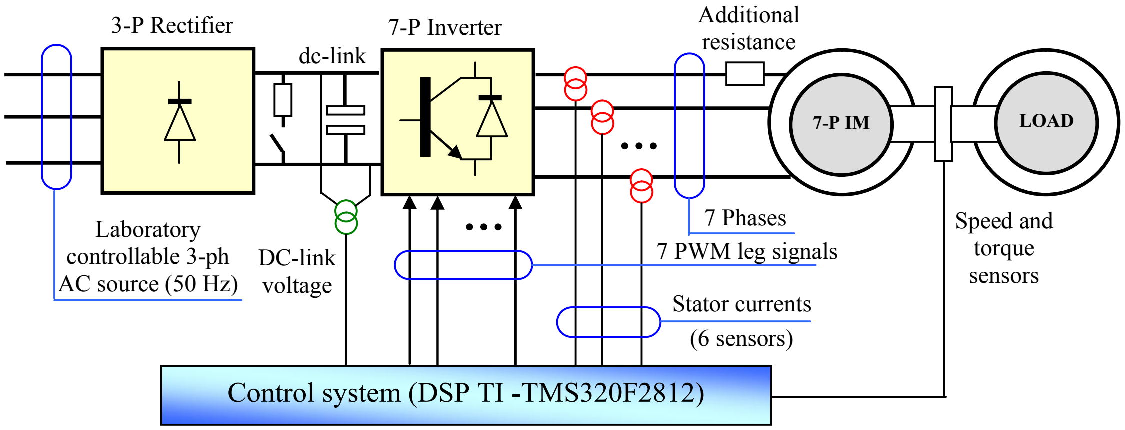

a)

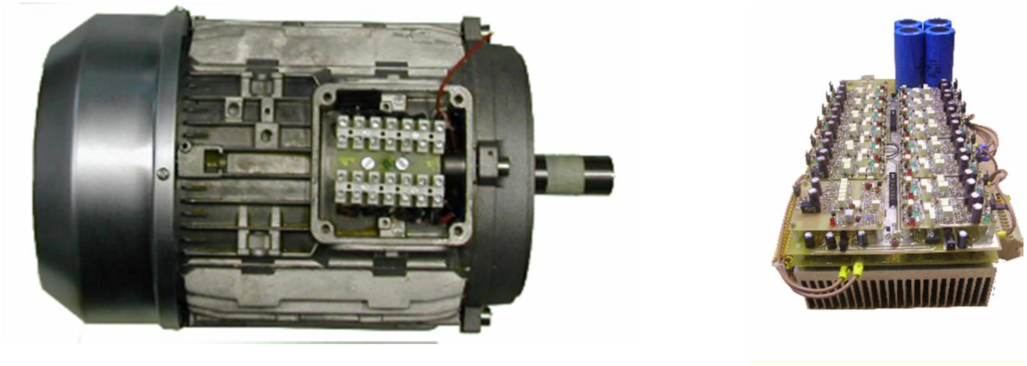

b) c)

Fig. 5. 8 Experimental set-up. a) Schematic diagram of the test bench and position of the current and voltage sensors. b) Seven phase induction machine. c) Seven phase inverter

5.3.2 Results

Without additional resistance, the behavior of the machine is regular and the stator currents are practically sinusoidal.

Figs. 5.9-5.10 show the behavior of $\bar{i}_{S3}$ and $\bar{i}_{S5}$ in these operating conditions. As can be seen in Figs. 5.9-a and 5.10-a, $\bar{i}_{S3}$ and $\bar{i}_{S5}$ are noisy quantities even in healthy operating conditions. The reason is the current ripple due to the pulse width modulation.

In addition, the control scheme adopted for the experimental tests is of open-loop type. Consequently, the currents are affected by the inverter nonlinearity (dead times, voltage drop of the conducting switches).

Finally, some manufacturing inaccuracies may lead to small asymmetries of the motor windings. As a result, $\bar{i}_{S3}$ and $\bar{i}_{S5}$ cannot be exactly null.

Fig. 5.9-b and 5.10-b show that spectra of $\bar{i}_{S3}$ and $\bar{i}_{S5}$. It can be noted that the most important harmonic component of $\bar{i}_{S3}$ is at 75 Hz, i.e., three times the fundamental frequency. This fact suggests that the currents in the planes α_3-β_3 and α_5-β_5 are mainly due to the perturbations resulting from the manufacturing machine asymmetry and the inverter nonlinearity.

It is straightforward to extract the harmonic components of $\bar{i}_{S3}$ and $\bar{i}_{S5}$ at 25 Hz. The behavior of these components is shown in Fig. 5.9-c and 5.10-c. As predicted by the theoretical analysis [5], the current space vectors move on elliptical trajectories, and the amplitudes of the major axes are lower than 50mA.

The behavior of the drive has been assessed under a phase imbalance. Figs. 5.11 and 5.12 show the behavior of the drive when an additional resistance, equal to twice the stator resistance, is added to phase 1, whereas Fig. 5.13 and 5.14 show the behavior of the drive when the additional resistance is added to phase 3.

As can be seen, the behavior of the drive is now very different from that in healthy condition.

The magnitudes of $\bar{i}_{S3}$ and $\bar{i}_{S5}$ are now sensibly greater and can be easily detected. Their spectra confirm that the most important harmonic components are at ±25 Hz, in perfect agreement with the theoretical analysis.

When the fault is in phase 1, the directions of the major axes of the ellipses in Fig. 5.11-c and 5.12-c coincide with that of the α-axis, as expected.

When the fault is in phase 3, the major axis of the ellipse of Fig. 5.11-c forms an angle of -50 degrees with the α-axis (an angle of -51.42 degrees was expected), whereas the major axis of the ellipse of Fig. 5.14-c forms an angle of 158 degrees (an angle of 154 degrees was expected). As can be seen from these results, there is a good agreement between theoretical predictions and experimental tests. Actual investigations are in progress for extending the developed technique based on time and frequency domain informations to time-frequency domain using the diagnosis technique validated in this thesis.

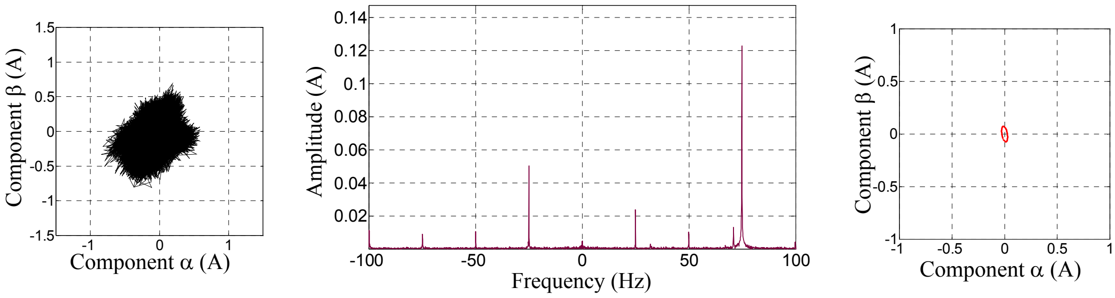

a) **b)** **c)**

Fig. 5. 9 - Experimental result. Behavior of the drive in healthy condition. a) Behavior of $\bar{i}_{S3}$. b) Spectrum of $\bar{i}_{S3}$. c) Trajectory of the components of $\bar{i}_{S3}$ at ±25 Hz

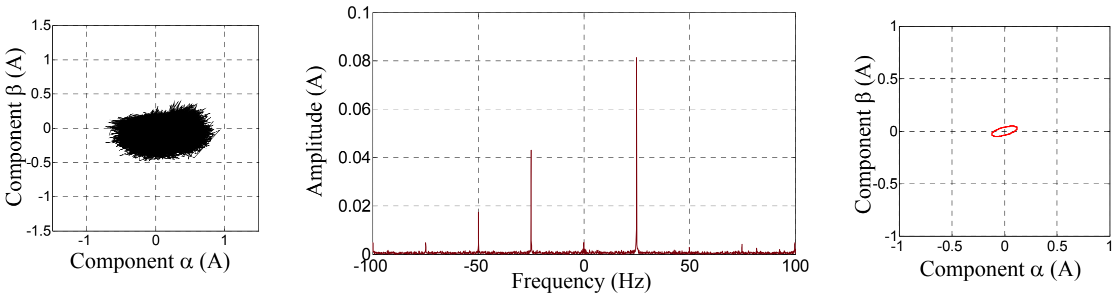

a) **b)** **c)**

Fig. 5. 10 Experimental result. Behavior of the drive in healthy condition. a) Behavior of $\bar{i}_{S5}$. b) Spectrum of $\bar{i}_{S5}$. c) Trajectory of the components of $\bar{i}_{S5}$ at ±25 Hz

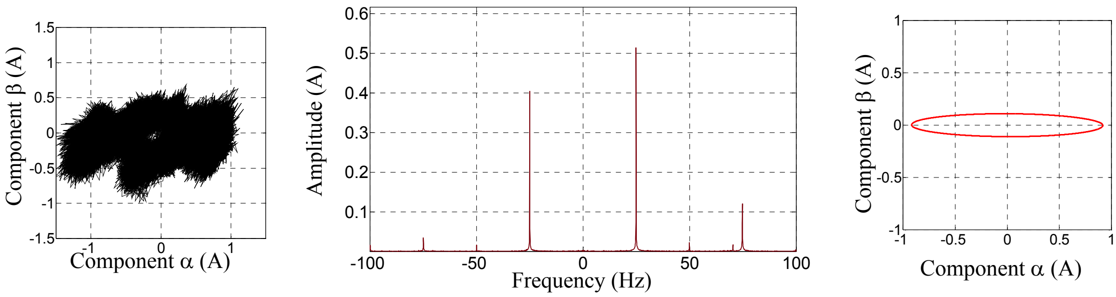

a) **b)** **c)**

Fig. 5. 11 Experimental result. Behavior of the drive when an additional resistance is in series with phase 1. a) Behavior of $\bar{i}_{S3}$. b) Spectrum of $\bar{i}_{S3}$. c) Trajectory of the components of $\bar{i}_{S3}$ at ±25 Hz.

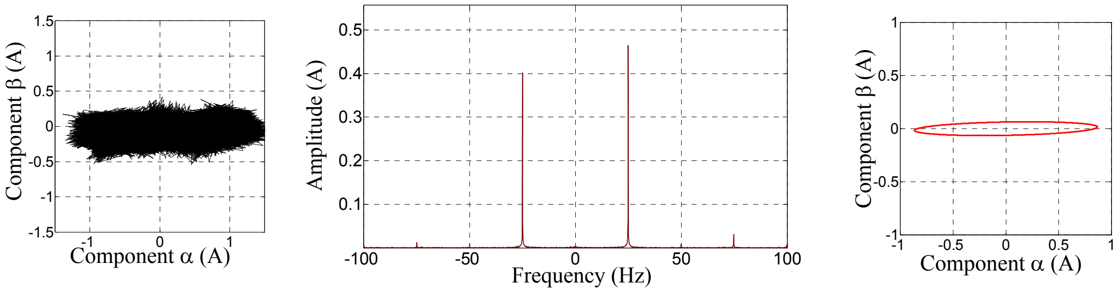

a) **b)** **c)**

Fig. 5. 12 Experimental result. Behavior of the drive when an additional resistance is in series with phase 1. a) Behavior of $\bar{i}_{S5}$. b) Spectrum of $\bar{i}_{S5}$. c) Trajectory of the components of $\bar{i}_{S5}$ at ±25 Hz.

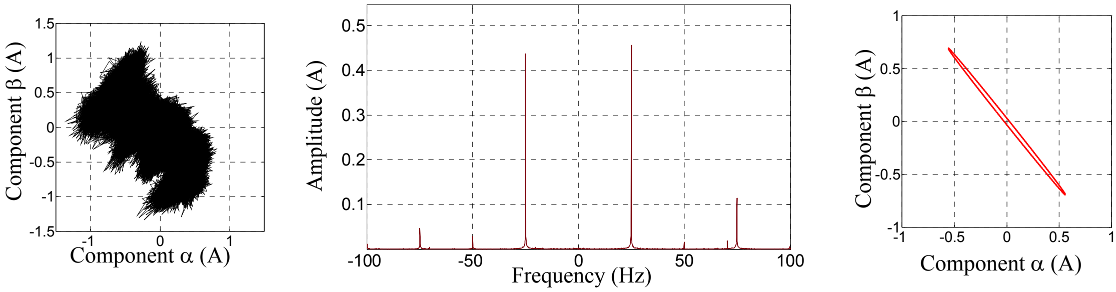

a) **b)** **c)**

Fig. 5. 13 Experimental result. Behavior of the drive when an additional resistance is in series with phase 1. a) Behavior of $\bar{i}_{S3}$. b) Spectrum of $\bar{i}_{S3}$. c) Trajectory of the components of $\bar{i}_{S3}$ at ±25 Hz

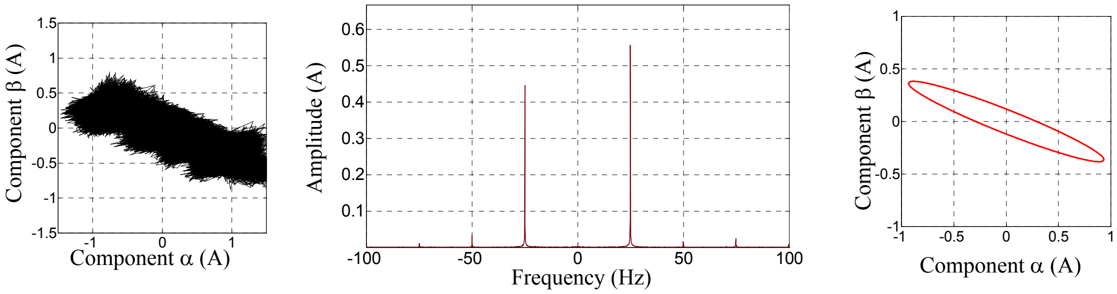

a) **b)** **c)**

Fig. 5. 14 Experimental result. Behavior of the drive when an additional resistance is in series with phase 1. a) Behavior of $\bar{i}_{S5}$. b) Spectrum of $\bar{i}_{S5}$. c) Trajectory of the components of $\bar{i}_{S5}$ at ±25 Hz

5.4 Conclusion

The proposed diagnosis technique was extended to the detection of rotor demagnetization, in five-phase surface-mounted permanent magnet synchronous generators under time-varying conditions. The proposed methodology was validated by means of two dimensional (2-D) Finite Element Analysis (FEA) and numerical simulations. Moreover, a cyclic quantification of the fault extent over time was introduced for accurate rotor fault detection.

Another important issue of stator fault detection and localization in multiphase induction machines with an odd number of phases was experimentally investigated. The analysis leads to a method to assess the unbalance condition of the machine, based on the calculation of the space vectors of the stator currents in the available α-β planes. The issued results in time and frequency domains are under investigation to be extended to time-frequency domain.

REFERENCES

[1] L. Parsa, H. A. Toliyat, “Five-phase permanent-magnet motor drives,” *IEEE Trans. on Ind. Appl.*, Vol. 41, No. 1, Jan./Feb. 2005, pp. 30-37.

[2] L. Parsa, N. Kim, H. Toliyat, “Field weakening operation of a high torque density five phase permanent magnet motor drive,” *in Proc. of the IEEE-IEMDC’05*, 15-18 May 2005, pp. 1507 - 1512.

[3] L. Parsa, H. A. Toliyat, "Sensorless direct torque control of five-phase interior permanent-magnet motor drives, " *IEEE Trans. on Ind. Appl.*, Vol. 43, No. 4, July/Aug. 2007.

[4] C. Olivieri, G. Fabri, M. Tursini, "Sensorless control of five-phase brushless dc motors", *SLED’10*, 9-10 July 2010, Padova, Italy, pp. 24-31.

[5] L. Zarri, M. Mengoni, Y. Gritli, A. Tani, F. Filippetti, G. Serra, D. Casadei, “Behavior of multiphase induction machines with unbalanced stator windings,” *Proc. of SDEMPED11*, Bologna, Italy, Sept. 5-8, pp. 84-91.

CONCLUSIONS

In the current thesis, a new diagnosis technique for electrical machines operating in time-varying conditions has been presented, where the validity under speed-varying condition or fault-varying condition was experimentally validated.

After an exhaustive analysis of the potential failure modes in electrical machines, such as stator and rotor electrical/mechanical faults, investigated in this thesis, a literature review of the corresponding diagnosis techniques was firstly established leading to the following possible improvements achieved by the proposed diagnosis technique in this thesis:also presented leading .

1) Capability of monitoring the fault evolution continuously over time under any transient operating condition;
2) No requirement for speed/slip measurement or estimation;
3) Higher accuracy in filtering frequency components around the fundamental;
4) Reduction in the likelihood of false indications by avoiding confusion with other fault harmonics (the contribution of the most relevant fault frequency components under speed-varying conditions are clamped in a single frequency band);
5) Low memory requirement due to low sampling frequency;
6) Reduction in the latency of time processing (no requirement of repeated sampling operation).

The effectiveness of the proposed diagnosis technique was then experimentally evaluated for the detection of rotor broken bars in single and then in double squirrel cage induction motors under speed-varying conditions. Results issued from motor current signature analysis and vibration signature analysis using the proposed technique have shown high reliability fault indexes.

Finally, the detection of rotor demagnetization, in five-phase surface-mounted permanent magnet synchronous generators under time-varying conditions was investigated in the fifth chapter showing the high accuracy of detection for this category of fault. An important issue of stator fault detection and localization in multiphase induction machines with an odd number of phases was experimentally investigated. The issued results in time and frequency domains are under investigation to be extended to time-frequency domain using the developed technique.

Possible improvements of the presented technique can be by combining electrical and mechanical signature analysis for improving the relevance of the fault index. This issue can be also achieved by the use of AI techniques planned for future works.

APPENDIX. 1: WRIM MODEL

Representing motor variables in two different reference frames will make the impedance matrix dependent on the rotor electrical angle. Anyway on the hypothesis of null homopolar current component the equations number is reduced to six, i.e. four voltage equations and two mechanicals. For the derivation of the mathematical model the following assumptions are considered: infinite iron permeability, smooth air gap, and three-phase symmetry of stator and rotor windings with sinusoidal distribution of the air gap flux density.

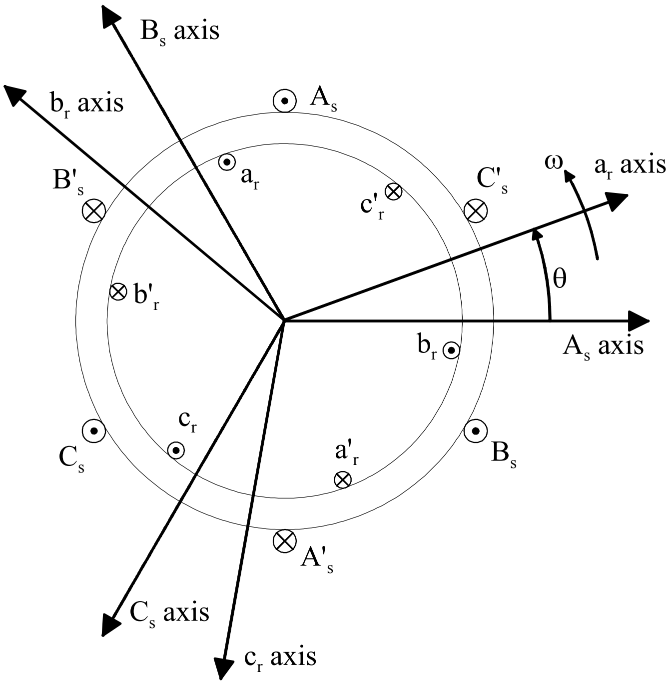

Fig. A.1 Wound rotor induction machine simplified scheme

Starting from the equation in the time domain for every single stator and rotor winding we can write, with reference to Fig. A.1, the following equations using concise matrix notation:

$$[v_{ABCS}] = [r_{ABCS}][i_{ABCS}] + \frac{d}{dt}[\lambda_{ABCS}] \qquad \text{(A.1. 1)}$$

$$[v_{abcr}] = [r_{abcr}][i_{abcr}] + \frac{d}{dt}[\lambda_{abcr}] \qquad \text{(A.1. 2)}$$

Where uppercase letters and the subscript *S* stand for stator quantities, lowercase letters and subscript *r* stand for rotor quantities, [*v*] represents the three phase voltages vector, [*i*] represents the three phase currents vector, [*r*] is a *3x3* diagonal matrix containing the three phase winding resistances and [*λ*] is the flux linkages vector of the three phase winding.

More in detail stator and rotor fluxes can be related to stator and rotor currents as follows:

$$\begin{bmatrix} \lambda_{ABCS} \\ \lambda_{abcr} \end{bmatrix} = \begin{bmatrix} [L_S] & [L_{Sr}(\theta)] \\ [L_{Sr}(\theta)]^T & [L_r] \end{bmatrix} \begin{bmatrix} i_{ABCS} \\ i_{abcr} \end{bmatrix} \tag{A.1. 3}$$

Where $[L_s]$, $[L_r]$ and $[L_{sr}(\theta)]$ represents the following matrixes of self and mutual inductance coefficients:

$$[L_S] = \begin{bmatrix} L_{AS} & M_{ABS} & M_{ACS} \\ M_{ABS} & L_{BS} & M_{BCS} \\ M_{ACS} & M_{BCS} & L_{CS} \end{bmatrix} \tag{A.1. 4}$$

$$[L_r] = \begin{bmatrix} L_{ar} & M_{abr} & M_{bcr} \\ M_{abr} & L_{br} & M_{bcr} \\ M_{acr} & M_{bcr} & L_{cr} \end{bmatrix} \tag{A.1. 5}$$

$$[L_{Sr}(\theta)] = \begin{bmatrix} L_{SrAa}\cos\theta & L_{SrAb}\cos\left(\theta + \frac{2\pi}{3}\right) & L_{SrAc}\cos\left(\theta - \frac{2\pi}{3}\right) \\ L_{SrBa}\cos\left(\theta - \frac{2\pi}{3}\right) & L_{SrBb}\cos\theta & L_{SrBc}\cos\left(\theta + \frac{2\pi}{3}\right) \\ L_{SrCa}\cos\left(\theta + \frac{2\pi}{3}\right) & L_{SrCb}\cos\left(\theta - \frac{2\pi}{3}\right) & L_{SrCc}\cos\theta \end{bmatrix} \tag{A.1. 6}$$

Where L_{JS} represents the total self inductance for the Jth stator phase winding given by the sum of the leakage inductance l_{JdS} and the stator self inductance taking into account the magnetic field lines that cross the air gap L_{JSS}. M_{IJS} is the mutual stator inductance coefficient, considering the flux linkage of the Ith stator winding due to the current flowing in the Jth stator winding. L_{SrIj} is the maximum value of the mutual inductance coefficient between stator and rotor, considering the flux linkage of the Ith stator winding due to the current flowing in the jth rotor winding. The meaning of L_{jr} and M_{ijr} coefficients is the same as for L_{JS} and M_{IJS} but referred to rotor windings.

By substituting (A.1.3), (A.1.4), (A.1.5) , (A.1.6) in (A.1.1) and (A.1.2), the complete set of voltage differential equations can be retrieved:

$$[v_{ABCS}] = [r_{ABCS}][i_{ABCS}] + [L_s]\frac{d}{dt}[i_{ABCS}] + [i_{abcr}]\frac{d}{dt}[L_{Sr}(\theta)] + [L_{Sr}(\theta)]\frac{d}{dt}[i_{abcr}] \tag{A.1. 7}$$

$$[v_{abcr}] = [r_{abcr}][i_{abcr}] + [L_r]\frac{d}{dt}[i_{abcr}] + [i_{ABCS}]\frac{d}{dt}[L_{Sr}(\theta)]^T + [L_{Sr}(\theta)]^T\frac{d}{dt}[i_{ABCS}] \tag{A.1. 8}$$

On the hypothesis of null homopolar stator and rotor currents and considering line to line voltages instead of phase voltages, the six equations (A.1.7) and (A.1.8) can be reduced to four equations:

$$\begin{bmatrix} v_{ACS} \\ v_{BCS} \\ v_{acr} \\ v_{bcr} \end{bmatrix} = \left[A(\theta,\omega)\right]\bullet\begin{bmatrix} i_{AS} \\ i_{BS} \\ i_{ar} \\ i_{br} \end{bmatrix} + \left[B(\theta)\right]\bullet\frac{d}{dt}\begin{bmatrix} i_{AS} \\ i_{BS} \\ i_{ar} \\ i_{br} \end{bmatrix} \tag{A.1. 9}$$

Where matrix $[A(\theta,\omega)]$ contains all the e.m.f. motional terms, whereas all the transformer terms are confined in $[B(\theta)]$. For the sake of brevity these two matrixes are not presented here since they do not add a lot to the discussion, anyway they can be easily derived from equations (A.1.7) and (A.1.8).

For the simulation of the transient electromechanical state also the two mechanical equations:

$$\frac{J}{P}\frac{d\omega}{dt} = T_{em} - T_l - K_a\left(\frac{\omega}{P}\right)^2 \tag{A.1. 10}$$

$$\frac{d\theta}{dt} = \omega \tag{A.1. 11}$$

where J is the moment of inertia T_l is the load torque and the T_{em} the electromagnetic torque, has to be added to the system where the T_{em} can be computed as follows:

$$T_{em} = [i_{ABCS}]^T \frac{d[L_{Sr}(\theta)]}{d\theta}[i_{abcr}] \tag{A.1. 12}$$

Once the set of differential equations (A.1.9) has been expressed in the explicit form (i.e. in the input state output form), and the two mechanical equations (A.1.10) and (A.1.11). are taken into account, the entire model presents:

- Five inputs, i.e. two stator line to line voltages, two rotor line to line voltages and the load torque.
- six state variables, i.e. two stator currents, two rotor currents, and two mechanical variables, the electrical rotor speed and angle.
- six outputs, i.e. the two stator currents in the stator reference frame, two rotor currents in the rotor reference frame, the electrical rotor speed and the electromagnetic torque.

It’s worth noting that, since the voltage equations are written in two different reference frames, the impedance matrixes in (A.1.9) are dependent on the rotor electrical position angle. Thus to obtain the explicit form of the voltage differential equations set the matrix [B(θ)] has to be inversed at each simulation step.

APPENDIX. 2: MULTIPLE SPACE VECTOR REPRESENTATION

For a given set of 5 real variables $x_1,...,x_k,...,x_5$ a new set of complex variables $y_0, \overline{y}_1, \overline{y}_3$ can be obtained by means of the following symmetrical linear transformations:

$$y_0 = \frac{1}{5} \sum_{k=1}^{5} x_k \tag{A.2. 1}$$

$$\overline{y}_\rho = \frac{2}{5} \sum_{k=1}^{5} x_k \, \overline{\alpha}^{\rho(k-1)}, \quad (\rho = 1, 3) \tag{A.2. 2}$$

where $\overline{\alpha} = \exp(j 2\pi / 5)$.

Relationships (A.2.1) and (A.2.2) lead to a real variable y_0 (zero-sequence component) and two complex variables $\overline{y}_1, \overline{y}_3$ (multiple space vectors).

The inverse transformations are

$$x_k = y_0 + \sum_{\rho=1,3} \overline{y}_\rho \cdot \overline{\alpha}^{\rho(k-1)}, \quad (k = 1, 2, ..., 5) \tag{A.2. 3}$$

where the symbol "·" represents the scalar product.

According to (A.2.1)-(A.2.3), a general five-phase system can be represented by two space vectors and the zero-sequence component. The two space vectors are mutually independent and move arbitrarily in the corresponding α-β planes.